Karlsruher Institut für Technologie

Schriftenreihe
Kontinuumsmechanik im Maschinenbau

31

Alexander Dyck

Chemo-Mechanically Coupled Models in Continuum Thermodynamics

KIT Scientific Publishing

Alexander Dyck

Chemo-Mechanically Coupled Models in Continuum Thermodynamics

Schriftenreihe
Kontinuumsmechanik im Maschinenbau
Band 31

Karlsruher Institut für Technologie (KIT)
Institut für Technische Mechanik
Bereich Kontinuumsmechanik

Hrsg. Prof. Dr.-Ing. habil. Thomas Böhlke

Eine Übersicht aller bisher in dieser Schriftenreihe erschienenen Bände finden Sie am Ende des Buchs.

Chemo-Mechanically Coupled Models in Continuum Thermodynamics

by
Alexander Dyck

KIT Scientific Publishing

Karlsruher Institut für Technologie
Institut für Technische Mechanik
Bereich Kontinuumsmechanik

Chemo-Mechanically Coupled Models in Continuum Thermodynamics

Zur Erlangung des akademischen Grades eines Doktor-Ingenieurs
von der KIT-Fakultät für Maschinenbau des
Karlsruher Instituts für Technologie (KIT) genehmigte Dissertation

von Alexander Dyck, M.Sc.

Tag der mündlichen Prüfung: 9. Januar 2025
Hauptreferent: Prof. Dr. Ing. habil. Thomas Böhlke
Korreferenten: Prof. Dr. Ing. habil. Michael Johlitz
Prof. Dr. rer. nat. habil. Astrid Pundt

Impressum

KIT Scientific Publishing

Karlsruher Institut für Technologie (KIT)
KIT Scientific Publishing
Straße am Forum 2
D-76131 Karlsruhe

www.bibliothek.kit.edu/ksp.php | E-Mail: info@ksp.kit.edu | Shop: www.ksp.kit.edu

Print on Demand 2025 – Gedruckt auf FSC-zertifiziertem Papier

ISSN 2192-693X
ISBN 978-3-7315-1425-1
DOI 10.5445/KSP/1000179945

Publications and citations

This publication based thesis is partially based the following publications, which are available under the CC BY 4.0 license[1]:

- **Dyck, A., Groß, L., Keursten J., Kehrer, L., Böhlke, T. (2024).** Modeling and FE simulation of coupled water diffusion and viscoelasticity in relaxation tests of polyamide 6. *Continuum Mechanics and Thermodynamics*.
  DOI: 10.1007/s00161-024-01305-4
- **Dyck, A., Böhlke, T., Pundt, A., Wagner, S. (2024).** Phase transformation in the palladium hydrogen system: Effects of boundary conditions on phase stabilities. *Scripta Materialia*, 247,
  DOI: 10.1016/j.scriptamat.2024.116117
- **Dyck, A., Böhlke, T., Pundt, A., Wagner, S. (2024).** Phase transformation in the Niobium Hydrogen system: Effects of elasto-plastic deformations on phase stability predicted by a thermodynamic model. *Scripta Materialia*, 251,
  DOI: 10.1016/j.scriptamat.2024.116209
- **Dyck, A., Gisy, J., Hille, F., Wagner, S., Pundt, A., Böhlke, T. (2025).** Hydride formation in open thin film metal hydrogen systems: Cahn-Hilliard-type phase-field simulations coupled to elasto-plastic deformation.
  Mechanics of Materials

Whenever parts from one of these publications is used, this is indicated by a footnote in the corresponding chapter, section or subsection

---

[1] `https://creativecommons.org/licenses/by/4.0/`

heading. The original section number from the paper is specified in the footnote. The term ’based on’ refers to the following types of adaption:

- Minor linguistic changes.
- Addition or omission of some parts of the original text.
- Homogenization of notation, and citation style of the publication content throughout the thesis.
- Introduction of references to other chapters in this thesis.
- Omission of repeating content and replacement with references to other chapters or sections of this thesis.
- Adaption of equation, figure and table numbering.

Captions of all figures and tables based on one of the publications specify the original publication and figure or table number using the term ’based on’. The formatting of figures and tables from publications has been homogenized. Further modifications are stated in the caption of the figure.

In one instance, major changes with respect to the content of the original publication were introduced, c.f. Sec. 3.4 and the table and figure contained therein. In this case the term ’adapted from’ is used and the respective footnotes and captions outline all major changes.

The author contributions to each work are given in the supplemental material at submission of this thesis and are listed in each publication.

Zusammenfassung

Die Betrachtung von Mehrfeldproblemen mithilfe von Kontinuumsmodellen erfährt eine zunehmende Bedeutung. Dies lässt sich beispielsweise an der gekoppelten Betrachtung von chemischen und mechanischen Feldern bei der Auslegung von Energiespeichersystemen aus der Ingenieurpraxis verdeutlichen. Um der Komplexität realer Prozesse gerecht zu werden sind validierte Modelle und effiziente Implementierungen in kommerziellen Finite-Elemente Solvern notwendig.

Im Rahmen dieser Arbeit werden chemo-mechanisch gekoppelte Kontinuumsmodelle im Rahmen der Coleman-Noll Prozedur thermodynamisch konsistent abgeleitet. Dabei werden Probleme der Wasserstoffversprödung, der Phasenseparation in Metall-Wasserstoffsystemen und der Diffusion von Wasser in Polymeren adressiert.

Im Kontext der Wasserstoffversprödung wird ein Schema vorgestellt, das es erlaubt, chemo-mechanisch gekoppelte Modelle mithilfe des kommerziellen Finite-Elemente Solvers ABAQUS zu lösen. Die Neuheit liegt dabei in der Nutzung des chemischen Potentials der diffundierenden Spezies als Freiheitsgrad, was Vorteile gegenüber in der Literatur etablierter Schemata mit sich bringt.

Im Kontext der Phasenseparation von Metall-Wasserstoffsystemen wird ein Modell vorgestellt, das die Phasenseparation von Niob und Palladium Dünnschicht-Systemen unter Wasserstoffbeladung beschreibt. Das Modell wird sowohl analytisch als auch mithilfe von Finite-Elemente Simulationen untersucht und die Resultate mit experimentellen Befunden verglichen. Dabei zeigt sich, dass zahlreiche im Experiment beobachtete Effekte durch das Modell präzise beschrieben werden.

Abschließend wird ein chemo-mechanisch gekoppeltes Modell für die Diffusion von Wasser in Polyamid 6 vorgestellt. Dieses wird unter Zuhilfenahme des zuvor vorgestellten Schemas implementiert. Im Vergleich mit Experimenten zeigt sich, dass das Modell das Trocknungsverhalten von Polyamid 6 in Abhängigkeit von Luftfeuchtigkeit und Umgebungstemperatur vorhersagen kann. Zudem kann durch das Modell ein Wiederanstieg des Relaxationsmoduls bei großer Versuchsdauer und erhöhter Temperatur abgebildet und mit der Kontraktion des Polyamids aufgrund der Trocknung erklärt werden.

Summary

The investigation of multi-physics problems using continuum models is becoming increasingly important. For instance, the coupled analysis of chemical and mechanical fields in the design of energy storage systems is now a standard practice in engineering. To address the complexity of real processes, validated models and efficient implementations in commercial Finite-Element solvers are essential.

In this thesis, we derive chemo-mechanically coupled continuum models in a thermodynamically consistent manner, following the Coleman-Noll procedure. Issues addressed by the models are related to hydrogen embrittlement, phase-separation in thin-film metal-hydrogen systems and the diffusion of water in polymers.

In the context of hydrogen embrittlement, a scheme is presented that allows for the solution of chemo-mechanically coupled models using the commercial Finite-Element solver ABAQUS. The novelty of this approach lies in its use of chemical potential of the diffusing species as the degree of freedom, which offers advantages over established schemes in the literature.

In the context of phase-separation in thin-film metal-hydrogen systems, a model is presented that describes phase-separation in Niobium and Palladium thin-film systems under hydrogen loading. The model is investigated both analytically and using Finite-Element simulations and the results are compared with experimental findings. It is demonstrated that numerous experimentally observed effects are accurately described by the model.

Finally, a chemo-mechanically coupled model for the diffusion of water in Polyamide 6 is presented. The model is implemented using the scheme previously introduced. The model is capable of predicting the drying behavior of Polyamide 6 in dependence on humidity levels and environmental temperature, confirmed by comparison to experimental results. In addition, the model predicts an increase in the relaxation modulus during prolongued tests at elevated temperatures, which is linked to the contraction of Polyamide due to drying.

Acknowledgments

First and foremost I want to express my gratitude to my supervisor Prof. Dr.-Ing. habil. Thomas Böhlke. During his amazing lectures I was introduced to the field of continuum mechanics. In addition, I am greatful for having the freedom (and the task) of choosing my own research topic and path. While this freedom was oftentimes challenging, it tremendously helped to shape my scientific work. Secondly I want to thank Prof. Dr.-Ing. habil. Michael Johlitz and Prof. Dr. rer. nat. habil. Astrid Pundt for not only reviewing my thesis, but also for being partners during fruitful discussions regarding my research work. Results of these discussions not only improved the contents of this thesis, but also broadened my scientific horizon. In addition I want to thank Prof. Dr.-Ing. habil. Bronislava Gorr for taking over the chair during the defense of my thesis.

I am very grateful to have worked alongside so many great people (both from scientific and administrative parts) at the Institute of Engineering Mechanics. Not only for being accessible for work related problems, but most importantly for being there as friends. This definitely extends to all the people I had the privilege of collaborating with, both from KIT and from other academic institutions.

Finally it is time to thank the people who are most dear to me. I think everyone knows how important caregivers are and I am glad to have all of you by my side.

Karlsruhe, April 2025 Alexander Dyck

Contents

Chapter 1

Introduction

1.1 Motivation and objectives

In many engineering applications multiple coupled fields are of interest. Examples include thermo-mechanically coupled problems, c.f. Wicht et al. (2021) and Gajek et al. (2022), in which the coupling of deformations to temperature is investigated, or chemo-mechanically coupled problems, where both diffusion processes and chemical reactions can occur, which can both be influenced by deformations or induce deformations, c.f. Johlitz and Lion (2013) and Dyck et al. (2024c). These examples involve the coupling of two fields. In the case of a thermo-mechanical coupling these are a mechanical and a thermal field, while chemo-mechanically coupled problems are concerned with a chemical field, typically a concentration field, and a mechanical field. Even more complicated problems involve more than two coupled fields, such as chemo-electro-mechanical problems in Lithium (Li)-Ion batteries (Bistri and Di Leo, 2023) or corrosion in metals (Makuch et al., 2024). Within the framework of this thesis, we restrict our considerations to two-field problems with a chemical and a mechanical field, i.e. chemo-mechanically coupled problems.

From an experimental perspective, investigating chemo-mechanically coupled problems is a challenging endeavor. Depending on the considered material system, this can be, e.g., due to:

- a large duration of experiments, as diffusive processes are slow and stationary conditions are only obtained after prolonged periods (Dyck et al., 2024c),
- difficulties in preparing appropriate samples and applying desired boundary conditions, which is especially true for miniaturized systems such as thin-film metal hydrogen systems (Dyck et al., 2024b;a; 2025) or Li-Ion batteries (Schoof et al., 2024) and
- the difficulty of separating different influencing factors and their effect on the observed experimental behavior.

Thus, it is often difficult to interpret experimental results. In these situations, model-driven simulations can assist with interpreting experiments. As they are less time-consuming, different geometries and boundary conditions can be easily investigated. Various effects that influence the experimentally observed behavior can be superimposed using models and their influence can be quantitatively determined. Finite-Element simulations have been used predominantly in this context, see, e.g., Miehe et al. (2010) and Hageman and Martínez-Pañeda (2023).

The present thesis is aimed at improving the understanding of chemo-mechanically coupled problems using Finite-Element simulations. Our primary objective is addressing the following issues:

- The simulation of chemo-mechanically coupled two-field problems using commercial Finite-Element solvers is challenging, as the partial differential equation governing the evolution of the chemical field is often not included in the solver library. We aim at bridging this gap by introducing a scheme that allows us to solve chemo-mechanically coupled problems using the commercial Finite-Element solver ABAQUS (Smith, 2009). As an application for the proposed scheme we investigate hydrogen embrittlement in metals, see, e.g., Barrera et al. (2016) and Fernández-Sousa et al. (2020).

- In order to better understand phase-separation in miniaturized systems, thin film metal hydrogen systems are frequently studied experimentally (Wagner et al., 2019). However, there are few models available for a computational investigation of these systems. Therefore we propose a new thermodynamic model, which allows us to study the phase-separation behavior in elasto-plastic thin film systems. We use both the Palladium-Hydrogen (Pd-H) and Niobium-Hydrogen (Nb-H) system as models and present results of analytical and numerical considerations, which are compared to experimental results.
- Depending on boundary conditions, polyamide can take up or release water from or to its surroundings. This is due to the hydrophilic nature of the amide group (Vlasveld et al., 2005) and has drastic consequences for the use of polyamide in engineering applications. We extend previous works on this coupled behavior, see, e.g., Sharma and Diebels (2021) and Sambale et al. (2021a), by proposing a chemo-mechanically coupled model that considers both diffusing water and the viscoelastic behavior of polyamide 6 (PA 6). We apply the model to simulate the drying of specimens and relaxation tests and compare the results to experimental observations summarized in Kehrer et al. (2023).

1.2 State of the art

1.2.1 Numerical simulation of coupled systems

The numerical solution of partial differential equations (PDEs) using Finite-Element-Methods (FEM) has been the topic of numerous works. Pioneering works in the context of chemo-mechanical coupling as well as thermo-mechanical coupling date back more than three decades, see, e.g., Sofronis and McMeeking (1989) and Simo and Miehe (1992). Initially, authors primarily relied on specifically developed in-house software. Later, commercial solvers such as ABAQUS (Smith, 2009) and open source libraries such as dealII (Arndt et al., 2023) became available, allowing an increase in the use of FEM in coupled problems of engineering applications.

As the amount of publications dealing with coupled problems relying on the FEM is too vast to be covered in this thesis, we discuss only publications relying on the commercial FEM solver ABAQUS in the context of chemo-mechanically coupled settings of hydrogen diffusion and embrittlement. The pioneering work of Sofronis and McMeeking (1989) established the basis of hydrogen embrittlement in metals relying on FEM. The basic concept was the coupling of hydrogen diffusion to stress gradients by considering the chemical potential as the driving force for diffusion, which was previously not attainable. Thereby both diffusion of hydrogen atoms to interstitial lattice sites as well as to defects of the lattice (so called trap sites) was considered. This concept was extended by considering the multiplication of trap sites due to plastic deformations in Krom et al. (1999) and, starting with the work of Oh et al. (2010), used in the commercial FEM solver ABAQUS. To this end, the authors Oh et al. (2010) noted, that the diffusion equation is similar to the heat-equation that is available in the solver library. Thus, in order to solve chemo-mechanically coupled problems, it is sufficient to interpret the gradient of the chemical potential as the heat flux by using subroutines developed by the users.

This so called heat-transfer analogy makes it possible to use the features of ABAQUS (such as visualization of results, contact formulations and different element formulations) with the flexibility of user-defined diffusion behavior through minimal coding. The heat-transfer analogy was extended in the works of Barrera et al. (2016), Díaz et al. (2016), Gobbi et al. (2019) and Fernández-Sousa et al. (2020) in order to include decohesion, fatigue and more efficient strategies of implementing the necessary subroutines.

All publications mentioned so far rely on hydrogen concentration as the degree of freedom. In contrast, Di Leo and Anand (2013) proposed using chemical potential as the degree of freedom, in order to study so-called open systems. These are exposed to an atmosphere containing gaseous hydrogen. In Di Leo and Anand (2013), this was also implemented in ABAQUS. Instead of using the heat-transfer analogy they relied on a user defined element formulation, which requires a more elaborate implementation for the same result.

1.2.2 Phase-separating metal hydrogen systems[1]

Intercalating systems such as metal-ion battery systems, metal hydrides or doped transition-metal oxides are often mentioned as a cornerstone in a future carbon free energy system, as they can serve as storage systems for renewable energies, see, e.g, Zï¿½ttel et al. (2008), Armand and Tarascon (2008), Adams and Chen (2011), Schneemann et al. (2018), McCay and Shafiee (2020) and Xia et al. (2023), or they possess a strong potential for electronic device applications, see, e.g., Nichols et al. (2013), Fruchter et al. (2018), Matsumoto et al. (2020) and Cichy and Świerczek (2021). The usability of a specific intercalating system is mainly determined by thermodynamical phase-boundaries and phase stabilities (Durbin and Malardier-Jugroot, 2013), as they define the systems' storage capacity and the temperature range of operation. In order to engineer both phase-boundaries and phase stabilities, miniaturization is a possible pathway, as these properties are strongly affected by microstructural and size effects (Schneemann et al., 2018; Wagner et al., 2019).

This mainly results from constraint conditions restricting the volumetric swelling of the host system during intercalation of another species. Commonly, intercalated atoms induce a volumetric, stress-free swelling

---

[1] Subsection 1.2.2 is based on section 1 of the publication "Hydride formation in open thin film metal hydrogen systems: Cahn-Hilliard-type phase-field simulations coupled to elasto-plastic deformations" (Dyck et al., 2025).

of the lattice (Fukai, 2005). However, interfaces and constraints can suppress this expansion, especially in miniaturized systems such as thin metal films adhered to a rigid substrate, c.f. Wagner et al. (2011), Hamm et al. (2015), Burlaka et al. (2015), Spatschek et al. (2016), Burlaka et al. (2016), Wagner et al. (2019) and Nichols et al. (2013), but also other materials systems with coherent interfaces, as shown in Armand and Tarascon (2008), Di Leo et al. (2014) and Phan et al. (2019). Mechanical stresses result from the constraints of these miniaturized systems, which have been shown to strongly influence solubility, stability of storage, catalytic or conductive phases, or phase transformations, c.f. Wagner et al. (2019), Liu et al. (2024) and Fernandez et al. (2021).

Among intercalating systems, metal-hydrogen systems with a capacity to form metal-hydrides offer efficient conditions to store hydrogen produced, e.g., from water electrolysis. The hydride phase acts as the storage phase, and the storage capacity is mainly given by the width of the miscibility gap between solid solution and hydride phases (Zï¿½ttel et al., 2008; Adams and Chen, 2011; Schneemann et al., 2018; McCay and Shafiee, 2020). In order to engineer or modify solubility and hydride phase stabilities of metal hydrogen systems by constraints, thin films of Pd-H as well as Nb-H widely serve as model systems due to the ease of their experimental handling. Extensive studies on these systems have been performed both on films loaded by gaseous hydrogen or by means of electrochemistry, using experimental methods such as X-Ray diffraction (XRD), transmission electron microscopy (TEM), scanning tunneling microscopy (STM), substrate curvature measurements or electromotoric force measurements (EMF) in the last decades, see, e.g., Zabel and Peisl (1979), Abromeit et al. (1997), Song et al. (2002), Gremaud et al. (2009), Pivak et al. (2011), Nörthemann and Pundt (2011), Baldi et al. (2014), Hamm et al. (2015), Burlaka et al. (2015), Griessen et al. (2016) and Wagner et al. (2019). Besides experimental methods, simulative approaches can lead to a better quantitative understanding of phase boundaries and phase stabilities. For both the Titanium-Hydrogen (Ti-H) as well as the Zirconium-Hydrogen (Zr-H) system, phase-field models are routinely used to predict hydride formation, growth or reorientation under applied loads on the continuum scale. For recent extensive reviews, we refer to Zhu et al. (2022) for the Ti-H system as well as Jia and Han (2023) for the Zr-H system.

Phase-field models introduce a diffuse interface between phases, which allows the application of numerical methods to compute the formation of different phases, while considering mechanical stresses in a coherent system (Schwarz and Khachaturyan, 1995). The basis of a phase-field model is a free energy functional, capturing chemical contributions of the bulk material and especially its tendency to form different phases, mechanical stresses and interface effects. The latter are introduced by considering gradients of so-called order parameters in the free energy functional (Steinbach, 2009; Steinbach and Shchyglo, 2011). A popular model relying on concentration or composition as a physical order parameter has been presented by Cahn and Hilliard (1958), who described the decomposition of a two-phase system. The Cahn-Hilliard equation has been used extensively in phase-field models, see, e.g., Voskuilen and Pourpoint (2013), Bair et al. (2017), Han et al. (2019), Heo et al. (2019) and Simon et al. (2021) for applications in the Zr-H systems, as well as Armand and Tarascon (2008), Di Leo et al. (2014) and Castelli et al. (2021) and the references mentioned therein for applications in battery materials. In the context of hydrogen-based direct reduction of iron oxide, a phase-field model was proposed in Bai et al. (2022).

For hydrogen storage metals, to the best of our knowledge, besides Spatschek et al. (2016), no such model has been presented in order to gain a more quantitative understanding of the complex phase separation behavior of thin film metal-hydrogen systems. These are frequently chosen as a model system, as they offer several beneficial aspects from the experimental point of view. This includes strong adhesion of the Nb film to the substrate, lattice matching between film and substrate and a small number of lattice defects such as grain boundaries (Wagner et al., 2019).

1.2.3 Water diffusion in polymers[2]

Polymer-based composites are widely used in engineering applications due to their potential as lightweight materials, combining low weight with high specific stiffness and strength, accompanied by design freedom for structural parts (Böhlke et al., 2019; Kehrer et al., 2017). For the characterization and modeling of the behavior of the composite material, an understanding of chemo-thermo-mechanical processes within the polymer matrix is a key factor. In this context, numerous models have been presented, considering both thermal and chemical effects in order to predict, e.g., ageing (Johlitz and Lion, 2013) or changes in the viscoelastic response (Sharma and Diebels, 2021). As the amount of publications is vast, we focus on the thermoplastic polymer PA 6 in the following.

The hydrophilic nature of the amide functional group of the PA 6 monomers leads to an uptake of water into the polymer network when PA 6 is exposed to humid environments. This water uptake can reach $9\,\mathrm{wt.\%}$ in dry weight (Vlasveld et al., 2005). The consequences are increased chain mobility, a shift in the glass transition temperature of PA 6 (Puffr and Šebenda, 1967; Jia et al., 2004) and a swelling of the polymer, as chain molecules are pushed apart due to diffusing water molecules (Sharma et al., 2020).

Depending on operating conditions, drying processes also occur in PA 6. In this context, experimental results of tests performed on injection molded PA 6, presented in Kehrer et al. (2023), showed unusual relaxation behavior, indicating drying effects. These have, to the best of

---

[2] Subsection 1.2.3 is based on section 1 of the publication "Modeling and FE simulation of coupled water diffusion and viscoelasticity in relaxation tests of polyamide 6" (Dyck et al., 2024c).

our knowledge, not been in the focus of investigation using chemo-mechanically coupled models.

1.3 Originality and outline

Chapter 2 This chapter establishes the fundamental continuum theory necessary for the remainder of this thesis. Besides kinematics, the governing equations of mixtures of two or more components are presented and discussed. This includes diffusion equations for diffusing components and a balance of internal energy and entropy for arbitrary mixtures of multiple components. The chapter closes with the thermodynamic principles that guide the derivation of the thermodynamically consistent continuum theories used in this thesis.

Chapter 3 In this chapter, a scheme is presented, that allows the simulation of arbitrary chemo-mechanically coupled problems using the commercial Finite-Element solver ABAQUS relying on chemical potential as the degree of freedom. This is an extension to previous publications such as Oh et al. (2010), Barrera et al. (2016), Gobbi et al. (2019) and Fernández-Sousa et al. (2020) that rely on the concentration of the diffusing component as the degree of freedom. Advantages and details for the implementation of the proposed scheme are presented. The process of hydrogen embrittlement in steels is considered as an example and the scheme is validated against the analytical and numerical results of Sofronis and McMeeking (1989) and Di Leo and Anand (2013). The process of deriving a thermodynamically consistent constitutive theory, outlined schematically in Chapter 2, is provided in detail.

Chapter 4 In contrast to the example of hydrogen embrittlement in the previous chapter, we consider metal hydrogen systems that show phase-separating behavior. Thus we focus on hydride forming metals, that show a phase separation into hydrogen poor α- and hydrogen rich hydride-phase upon hydrogen absorption. For these phase-separating metal hydrogen systems we propose a thermodynamic model, that incorporates both elasto-plastic deformations of the metal as well as their coupling to the diffusion of interstitial hydrogen atoms. We apply the model to Pd-H and Nb-H, using both analytical investigations and numerical computations in order to study phase-separation and its suppression, depending on constraint or boundary conditions and material behavior.

Chapter 5 In this chapter, we turn our investigation towards chemo-mechanically coupled processes in viscoelastic PA 6. Relaxation experiments presented by Kehrer et al. (2023) indicated significant drying and a coupling to the viscous behavior of PA 6. To explain the observed behavior we propose a chemo-mechanically coupled theory that allows us to predict water uptake and release coupled to visco-elastic deformations of PA 6 for varying boundary conditions, such as temperature and relative humidity. We compare model predictions to experimental results to validate the proposed model.

Chapter 6 We close this thesis by summarizing our most important results and presenting possible pathways for future research.

1.4 Remarks on the notation

A direct tensor notation is used throughout the text. Tensor components are expressed using Latin indices and Einstein's summation convention is applied. All vector and tensor components are expressed with respect to the orthonormal basis $\{\boldsymbol{e}_1, \boldsymbol{e}_2, \boldsymbol{e}_3\}$. Vectors and second-order tensors are denoted by lower case and upper case bold letters, respectively (e.g., $\boldsymbol{a}$ and $\boldsymbol{A}$). Within this thesis, the highest tensor rank is four and tensors of this rank are denoted as blackboard bold, e.g., $\mathbb{A}$. In some instances, such as in Chapter 4, tensor components are expressed with respect to a Voigt-Mandel basis, i.e. in Voigt-Mandel notation. In these cases, column vectors and matrices are used, which are denoted via underscores, e.g.,

$\underline{a}, \underline{\underline{A}}$.

The following operations between tensors are necessary for this work:

- The scalar product between tensors of equal rank is denoted by $\cdot$, e.g., $\boldsymbol{a} \cdot \boldsymbol{b} = a_i b_i$.
- The tensor product, or dyadic product, is $\otimes$.
- The linear mapping of a vector is $\boldsymbol{Ab} = A_{ij} b_j \boldsymbol{e}_i$.
- The composition of two second-rank tensors is $\boldsymbol{AB} = A_{ij} B_{jk} \boldsymbol{e}_i \otimes \boldsymbol{e}_k$.
- To express the mapping of a second-rank tensor via a fourth-rank tensor we use $\mathbb{A}\left[\boldsymbol{B}\right] = A_{ijkl} B_{kl} \boldsymbol{e}_i \otimes \boldsymbol{e}_j$.
- The transposed form of a second-rank tensor is denoted as $\boldsymbol{A}^{\mathsf{T}}$.
- The Rayleigh product between $\boldsymbol{Q}$ and a tensor of rank four $\mathbb{A}$ is denoted as $\boldsymbol{Q} \star \mathbb{A} = A_{ijkl} (\boldsymbol{Q}\boldsymbol{e}_i) \otimes (\boldsymbol{Q}\boldsymbol{e}_j) \otimes (\boldsymbol{Q}\boldsymbol{e}_k) \otimes (\boldsymbol{Q}\boldsymbol{e}_l)$.

In this thesis, all newly introduced quantities are defined upon their first appearance in each chapter.

Chapter 2

Fundamentals of multi-component continuum chemo-mechanics

2.1 Introduction

In this chapter a brief summary of fundamentals of continuum chemo-mechanics for a small-strain setting is set out. This includes kinematic relations and governing equations (or balance equations) for multi-component systems. The governing equations are closed, i.e. specified for a specific material, using a thermodynamically consistent constitutive theory relying on the evaluation of the entropy principle. Applications of the closed equations are presented in Chapter 3 for the case of hydrogen embrittlement, in Chapter 4 for phase-separating metal hydrogen systems and in Chapter 5 for water diffusion in PA 6. The constitutive theory is detailed in each chapter.

2.2 Kinematics

We restrict the following considerations to three-dimensional material bodies that consist of material points in an arbitrarily chosen reference placement Ω_0 (Šilhavï¿½, 1997). Each material point has a position in this reference placement, described by $\boldsymbol{X} \in \Omega_0$. For all times $t \geq 0$, the motion of each material point is then, described by the mapping

$\boldsymbol{\chi}(\boldsymbol{X},t)$, where $\boldsymbol{\chi}(\boldsymbol{X},0) = \boldsymbol{X}$ holds. We restrict our presentation to Boltzmann continua, also called non-polar material bodies. These are material bodies without additional rotational degrees of freedom.
Following the definition of the motion, the current placement Ω_t of a material body is given as (Šilhavï¿½, 1997)

$$\boldsymbol{x} = \boldsymbol{\chi}(\boldsymbol{X},t). \tag{2.1}$$

Any tensorial field Θ can be expressed as a function of either the current or the reference placement, where the former is called Eulerian and the latter Lagrangian. Both descriptions are related by (Haupt, 2002)

$$\Theta_\mathrm{L}(\boldsymbol{X},t) = \Theta_\mathrm{E}(\boldsymbol{\chi}(\boldsymbol{X},t),t) \quad \text{and} \quad \Theta_\mathrm{E}(\boldsymbol{x},t) = \Theta_\mathrm{L}(\boldsymbol{\chi}^{-1}(\boldsymbol{x},t),t). \tag{2.2}$$

The material time derivative of a tensorial field $\Theta_\mathrm{L}(\boldsymbol{X},t)$ in Lagrangian description is defined as

$$\dot{\Theta}_\mathrm{L}(\boldsymbol{X},t) = \frac{\partial \Theta_\mathrm{L}(\boldsymbol{X},t)}{\partial t}. \tag{2.3}$$

The Lagrangian velocity $\boldsymbol{v}_\mathrm{L}$ and acceleration $\boldsymbol{a}_\mathrm{L}$ thus follow as

$$\boldsymbol{v}_\mathrm{L}\left(\boldsymbol{X},t\right) = \frac{\partial \boldsymbol{\chi}}{\partial t}\left(\boldsymbol{X},t\right), \quad \boldsymbol{a}_\mathrm{L}\left(\boldsymbol{X},t\right) = \frac{\partial^2 \boldsymbol{\chi}}{\partial t^2}\left(\boldsymbol{X},t\right). \tag{2.4}$$

Using the chain rule, the material time derivative of a tensorial field in an Eulerian $\Theta_\mathrm{E}(\boldsymbol{x},t)$ description is given by

$$\dot{\Theta}_\mathrm{E}(\boldsymbol{x},t) = \frac{\partial \Theta_\mathrm{E}(\boldsymbol{x},t)}{\partial t} + \frac{\partial \Theta_\mathrm{E}(\boldsymbol{x},t)}{\partial \boldsymbol{x}} \cdot \boldsymbol{v}_\mathrm{E}(\boldsymbol{x},t). \tag{2.5}$$

In the following, the Lagrangian description will be used predominantly. We will distinguish different placements by means of their arguments, while the indices $(\cdot)_\mathrm{E}$ and $(\cdot)_\mathrm{L}$ will be omitted to shorten notation.
In order to measure the deformation of a material body, we introduce

the deformation gradient

$$\boldsymbol{F} = \frac{\partial \boldsymbol{\chi}(\boldsymbol{X}, t)}{\partial \boldsymbol{X}}. \tag{2.6}$$

It maps infinitesimal line, oriented area and volume elements from the reference placement to the current placement via (Haupt, 2002)

$$\mathrm{d}\boldsymbol{x} = \boldsymbol{F}\mathrm{d}\boldsymbol{X}, \quad \mathrm{d}\boldsymbol{a} = \det(\boldsymbol{F})\boldsymbol{F}^{-\mathsf{T}}\mathrm{d}\boldsymbol{A}, \quad \mathrm{d}v = \det(\boldsymbol{F})\mathrm{d}V. \tag{2.7}$$

A suitable measure for deformations should comprise vanishing deformations for zero displacements, without any rigid body rotations (Bertram, 2012). Thus, to describe the deformation of a material body, the deformation gradient is not a suitable measure, as it does not vanish for zero displacements and may contain rigid body rotations. In order to separate the stretch part of $\boldsymbol{F}$ from its rotational part, the deformation gradient is decomposed by means of the unique polar decomposition (Haupt, 2002)

$$\boldsymbol{F} = \boldsymbol{R}\boldsymbol{U} = \boldsymbol{V}\boldsymbol{R}. \tag{2.8}$$

Here, $\boldsymbol{R}$ is an orthogonal tensor representing rigid body rotations, while $\boldsymbol{U}$ and $\boldsymbol{V}$ are the right and left stretch tensors respectively. In large strain continuum mechanics, deformation measures are commonly defined relying on either the right or left stretch tensors, see, e.g, Haupt (2002) and Bertram (2012). However, in this work, we restrict our presentation to a small-strain setting. For this, we introduce the following assumptions, which are based on the displacement field $\boldsymbol{u}$ defined as the difference between current and initial placement

$$\boldsymbol{u}(\boldsymbol{X}, t) = \boldsymbol{\chi}(\boldsymbol{X}, t) - \boldsymbol{X}. \tag{2.9}$$

The gradient of the displacement field is called the displacement gradient $\boldsymbol{H}$, defined as

$$\boldsymbol{H} = \frac{\partial \boldsymbol{u}}{\partial \boldsymbol{X}} = \boldsymbol{F} - \boldsymbol{I}, \tag{2.10}$$

where $\boldsymbol{I}$ is the identity tensor. Based on the definition of $\boldsymbol{H}$, we call a deformation small if

$$\|\boldsymbol{H}\| \ll 1, \tag{2.11}$$

where $\|\boldsymbol{H}\|$ denotes the Frobenius norm of the displacement gradient. When this condition holds, we linearize the deformation gradient at $\boldsymbol{F} \approx \boldsymbol{I}$ and the right stretch and rotation tensor can be approximated by (Haupt, 2002)

$$\boldsymbol{U} \approx \boldsymbol{I} + \boldsymbol{\varepsilon}, \quad \boldsymbol{R} \approx \boldsymbol{I} + \boldsymbol{\omega}. \tag{2.12}$$

Here

$$\boldsymbol{\varepsilon} = \frac{1}{2}\left(\boldsymbol{H} + \boldsymbol{H}^{\mathsf{T}}\right) \tag{2.13}$$

is the infinitesimal strain tensor and

$$\boldsymbol{\omega} = \frac{1}{2}\left(\boldsymbol{H} - \boldsymbol{H}^{\mathsf{T}}\right) \tag{2.14}$$

the infinitesimal rotation tensor. The infinitesimal strain tensor does vanish for vanishing deformation, i.e. $\boldsymbol{\varepsilon} = \boldsymbol{0}$ and is thus a suitable measure of the deformation of a body. Based on the small-strain assumption, the current and reference configuration coincide up to rigid body movements, so that the current and reference configuration cannot be distinguished anymore (Haupt, 2002).

2.3 Balance equations for multi-component systems

2.3.1 Preliminaries

The behavior of material bodies is governed by balance equations. Typically, balance equations are specified in global (or integral) form for extensive quantities. Extensive quantities are those, that are proportional to the mass of the system (Papenfuß, 2020). Generally speaking, an extensive quantity within a control volume can change due to production, supply or fluxes over the system's boundary. Using Reynold's transport theorem as well as Gauss' theorem, local balance equations can be derived, valid for any material point within a domain (Šilhavï¿½, 1997; Papenfuß, 2020). All balance equations are valid for any material, but need to be tailored to the material under consideration via constitutive theories. This is commonly done by evaluating the entropy principle, in order to derive restrictions on the constitutive behavior. This procedure is discussed in detail in Sec. 2.4.

In classic continuum mechanics, only a single component is considered to occupy a domain. However, in many cases multiple components appear within the considered domain and contribute to the overall behavior of the mixture of the individual components. Examples of such multi-component systems are, e.g., materials used in energy storage applications like Li-Ion batteries (Schoof et al., 2024), hydrogen diffusion through metals (Dyck et al., 2024b) or PA 6 taking up humidity from its surroundings (Dyck et al., 2024c).

To this end, we extend the classic concepts of the balance equations of mass, momentum, energy and entropy to mixtures or multi-component systems. Each component is described by an individual set of governing equations, which are called partial balance equations in the following. Balance equations for the mixture are given by superposition of the individual balance equations, c.f. Müller (1968) and Mï¿½ller (1985). With this notion, we assume that a material point within a domain can be occupied by several components at the same time (Greve, 2003). In contrast to single-component systems, conserved quantities such as the mass of individual components are not necessarily conserved in multi-component systems, e.g., due to chemical reactions between the components.

Before proceeding we introduce the notion of specific quantities and densities. Specific quantities are expressed with respect to the mass, while densities are expressed with respect to the volume, such as a mass density in $\mathrm{kg/m^3}$. In addition we point out that domains without singular surfaces are considered, such that balance equations for singular surfaces are not presented. Extensions to systems containing singular surfaces can be found in, e.g., Papenfuß (2020).

2.3.2 Partial densities

When a continuous system is composed of multiple components $\gamma = 1 \ldots \xi$, where ξ denotes the number of components, the partial densities for each component are (Greve, 2003)

$$\rho_\gamma = \frac{\mathrm{d}m_\gamma}{\mathrm{d}V}. \tag{2.15}$$

Here $\mathrm{d}V$ is the infinitesimal total volume element and $\mathrm{d}m_\gamma$ the infinitesimal mass of component γ at a material point. We use small-strain theory and therefore do not distinguish between the infinitesimal volume element $\mathrm{d}V$ in current and reference placement. Extensions to large deformation theories can be found in Mï¿½ller (1985) and Gurtin et al. (2010).

Building upon the partial densities of each component, the density of the mixture follows by (Greve, 2003)

$$\rho = \sum_{\gamma=1}^{\xi} \rho_\gamma. \tag{2.16}$$

The dimensionless mass fraction or concentration c_γ of each component is given by

$$c_\gamma = \frac{\rho_\gamma}{\rho}. \tag{2.17}$$

The concentration c_γ of each component at a material point can also be expressed in moles per infinitesimal volume element $\mathrm{d}V$, by dividing the mass fraction by the molar mass M_γ of component γ. In the context of metal hydrogen systems it is common to express the concentration in number of hydrogen molecules to the number of metal atoms. To remain close to publications in the respective community, we use the concentration c in moles per unit volume in Chapter 3, while in Chapter 4 we use the concentration in number of hydrogen atoms per metal atom, expressed as c_{H}. In Chapter 5, both the mass fraction, expressed as c, as well as the concentration in moles per unit volume, expressed as ϑ, will be used. In each chapter it will be made clear, which definition for the concentration is being used.

2.3.3 Motion of each component

The motion of each component is given by the function $\boldsymbol{\chi}_\gamma(\boldsymbol{X}, t)$, which allows for the definition of the partial velocity

$$\boldsymbol{v}_\gamma = \frac{\partial \boldsymbol{\chi}_\gamma}{\partial t}. \tag{2.18}$$

The so-called barycentric velocity, i.e. the velocity of the mixture, follows as (Greve, 2003)

$$\boldsymbol{v} = \frac{1}{\rho} \sum_{\gamma=1}^{\xi} \rho_\gamma \boldsymbol{v}_\gamma. \tag{2.19}$$

From the barycentric velocity, the diffusion velocity $\tilde{\boldsymbol{j}}$ of component γ follows as

$$\tilde{\boldsymbol{j}}_\gamma = \boldsymbol{v}_\gamma - \boldsymbol{v}. \tag{2.20}$$

2.3.4 A special case of multi-component systems

In order to solve PDEs governing the behavior of multi-component systems with ξ components, it is necessary to determine a partial density ρ_γ, the motion $\boldsymbol{\chi}_\gamma$ and, in some cases, the temperature θ_γ of each component. This equates to 5ξ unknowns. In addition, constitutive laws have to be derived for each component, in order to close the governing equations. Examples of such approaches can be found in, e.g., Johlitz and Lion (2013) and Sharma and Diebels (2021). However, the partial densities of individual components are, in many applications, small in comparison to other components and thus their contribution to equations governing the behavior of the mixture can be neglected (Greve, 2003). In fact, this occurs in many engineering applications. Examples include hydrogen diffusion in a metal, c.f. Dyck et al. (2024b), water diffusion in a polymer, c.f. Dyck et al. (2024c) or Li diffusion in Li-Ion batteries, c.f. Schoof et al. (2024).

In the following, we restrict all considerations to multi-component systems where

- ξ components are considered,
- component 1 is a solid material, serving as host material through which diffusion occurs, and
- the partial density $\rho_1 \gg \rho_\gamma,\ \gamma \in [2, \xi]$.

For these multi-component systems, the behavior of the mixture is dominated by the solid host material (Greve, 2003). The behavior of the mixture can be modeled by a combination of

- a balance equation for each concentration $c_\gamma,\ \gamma \in [2, \xi]$,
- a quasi-static balance of linear momentum for the mixture,
- a balance equation for the internal energy density e of the mixture and
- a balance equation for the mixture entropy density η.

These mixture balance equations are (Greve, 2003)

$$
\begin{aligned}
\dot{c}_\gamma &= -\mathrm{div}\left(\boldsymbol{j}_\gamma\right) + \pi_\gamma,\ \gamma \in [2, \xi]\,, \\
\boldsymbol{0} &= \mathrm{div}\left(\boldsymbol{\sigma}\right), \\
\dot{e} &= w + \boldsymbol{\sigma} \cdot \dot{\boldsymbol{\varepsilon}} - \mathrm{div}\left(\boldsymbol{q}_\mathrm{e}\right), \\
\dot{\eta} &= s_\eta + p_\eta - \mathrm{div}\left(\boldsymbol{q}_\eta\right),
\end{aligned}
\tag{2.21}
$$

where the concentrations c_γ are expressed in moles per unit volume. The newly introduced quantities are the diffusion flux $\boldsymbol{j}_\gamma$, describing the diffusion of component γ with respect to the solid host material in moles per unit area and time, reaction rates between different components π_γ in moles per unit volume and time, the Cauchy stress tensor of the mixture $\boldsymbol{\sigma}$, the heat source density w, the internal power density for small deformations $\boldsymbol{\sigma} \cdot \dot{\boldsymbol{\varepsilon}}$, the flux of internal energy $\boldsymbol{q}_\mathrm{e}$, the supply density of entropy s_η, the entropy production density p_η and the entropy flux $\boldsymbol{q}_\eta$. Before proceeding, some comments regarding Eq. (2.21) are in order:

- The mass density of the mixture ρ is a conserved quantity, such that $\sum_\gamma \pi_\gamma = 0$.
- We assume the host material to be incompressible, such that $\dot{\rho} = 0$ holds.
- Diffusive processes are slow compared to inertia effects, which is why a quasi-static balance of linear momentum is considered.
- As the components considered are non-polar, the Cauchy stress tensor is symmetric, i.e. $\boldsymbol{\sigma} = \boldsymbol{\sigma}^\mathsf{T}$.
- Only one temperature field θ is introduced for the mixture.
- A heat-equation governing changes in the mixture temperature field can be derived by using the balance equation for the internal energy density, c.f. Di Leo and Anand (2013). However, since thermal conductivity is orders of magnitudes faster than chemical diffusion, we do not derive such an equation and focus on isothermal cases at a given temperature.
- The constitutive quantities are the diffusion fluxes $\boldsymbol{j}_\gamma$, the symmetric Cauchy stress tensor of the mixture $\boldsymbol{\sigma}$, the flux of internal energy of the mixture $\boldsymbol{q}_\mathrm{e}$, the entropy supply density s_η and the entropy flux of the mixture $\boldsymbol{q}_\eta$.

- In the next section we use the second law of thermodynamics, i.e. a non-negative entropy production density of the mixture p_η, to derive restrictions on the constitutive equations.

2.4 Constitutive theory and entropy principle

The balance equations presented above are valid for any multi-component system for which the assumptions introduced above hold. To describe a particular multi-component system, constitutive relations need to be introduced, in order to arrive at a closed form of the balance equations. Over the years, numerous different approaches towards finding constitutive laws have been developed. These include thermostatics or equilibrium thermodynamics, irreversible thermodynamics (with or without internal variables), rational thermodynamics and extended thermodynamics. For a brief introduction we refer to Papenfuß (2020). Without going into more detail, each approach requires the definition of a state space, i.e. the independent variables of the considered thermodynamic processes, as well as the thermodynamic potential. In this thesis, the thermodynamic potential used is the free energy density ψ, which is another constitutive quantity. The free energy follows from the internal energy density e, the entropy density η and the mixture temperature θ by means of the Legendre transformation $\psi = e - \eta\theta$. The set of constitutive quantities is

$$\Pi = \{\boldsymbol{j}_\gamma, \boldsymbol{\sigma}, \boldsymbol{q}_\mathrm{e}, \boldsymbol{q}_\eta, s_\eta, \psi\}. \tag{2.22}$$

These are functions of the independent variables, which are, in the context of this thesis, denoted as the set

$$\Lambda = \{c_1, c_2, ..., c_\gamma, \boldsymbol{\varepsilon}, \theta, \underline{\alpha}\}, \tag{2.23}$$

where $\underline{\alpha}$ denotes a tuple of internal variables, that allow the introduction of plastic strains, c.f. Chapter 3 and 4, or viscoelastic strains, c.f. Chapter 5. By inserting the Legendre transformation and a non-negative entropy production density $p_\eta > 0$ into Eq. (2.21) (4), the entropy inequality results as (Johlitz and Lion, 2013)

$$\frac{1}{\theta}\left(\dot{e} - \eta\dot{\theta}\right) - \frac{\dot{\psi}}{\theta} + \operatorname{div}\left(\boldsymbol{q}_\eta\right) - s_\eta \geq 0. \tag{2.24}$$

This entropy inequality introduces restrictions for all constitutive quantities, both in equilibrium and non-equilibrium processes.

There is a need to distinguish two different schools for the evaluation of the entropy inequality. The first one is the Coleman-Noll procedure, introduced by Coleman and Noll (1963). It relies upon assumptions for the entropy flux $\boldsymbol{q}_\eta$ and the entropy supply density s_η. The second school for evaluating the entropy inequality was introduced by Liu (1972) and is commonly called Liu-Müller entropy principle, see also Mï¿½ller (1985). In this school, no further assumptions regarding the entropy supply and flux are necessary. Besides Eq. (2.24), all balance equations and all equations governing the evolution of internal variables are added to the entropy inequality by means of Lagrange multipliers. This procedure is less commonly used in continuum chemo-mechanics, but offers a more general framework for the derivation of thermodynamically consistent constitutive relations.

Within the context of this work, we use the Coleman-Noll procedure to derive restrictions on the constitutive quantities. We introduce another assumption with respect to the flux of the internal energy of the mixture: it can be additively decomposed into a contribution due to heat flux $\boldsymbol{q}_\theta$ and a flux of the diffusing, non-dominant components with concentration c_γ, $\gamma \in [2, \xi]$. The contribution of the diffusive fluxes are weighted by the respective chemical potential μ_γ, which implies that

$$\boldsymbol{q}_{\mathrm{e}} = \boldsymbol{q}_\theta + \sum_{\gamma=2}^{\xi} \mu_\gamma \boldsymbol{j}_\gamma. \tag{2.25}$$

This approach was popularized by Gurtin and Vargas (1971) and is used frequently for the modeling of chemo-mechanically coupled processes, see, e.g., Di Leo et al. (2014) and Di Leo et al. (2015). By inserting the balance of internal energy of the mixture (Eq. (2.21) (3)), the flux of the internal energy introduced in Eq. (2.25) and the assumptions of Coleman and Noll for the entropy flux $\boldsymbol{q}_\eta = \boldsymbol{q}_{\mathrm{e}}/\theta$ and the entropy supply density $s_\eta = w/\theta$ into the entropy inequality (2.24), we arrive at the entropy inequality relevant for all constitutive theories discussed in this thesis. After some simplifications, the entropy inequality can be expressed as

$$\begin{gathered} -\dot{\psi} - \eta\dot{\theta} + \boldsymbol{\sigma} \cdot \dot{\boldsymbol{\varepsilon}} - \frac{1}{\theta}\boldsymbol{q}_\theta \cdot \operatorname{grad}(\theta) - \\ \sum_{\gamma=2}^{\xi} \operatorname{grad}(\mu_\gamma) \cdot \boldsymbol{j}_\gamma - \sum_{\gamma=2}^{\xi} \mu_\gamma \operatorname{div}\left(\boldsymbol{j}_\gamma\right) \geq 0. \end{gathered} \tag{2.26}$$

Before proceeding, we comment on this specific form of the entropy inequality:

- The contribution of the diffusing components is limited to the flux of internal energy within this framework (Gurtin and Vargas, 1971).
- The resulting inequality has to hold for all thermodynamic processes.
- The concentration balances of Eq. (2.21) (1) can be inserted to introduce the time derivative of the concentrations $\dot{c}_\gamma$. This results in

$$\begin{gathered} -\dot{\psi} - \eta\dot{\theta} + \boldsymbol{\sigma} \cdot \dot{\boldsymbol{\varepsilon}} - \frac{1}{\theta}\boldsymbol{q}_\theta \cdot \operatorname{grad}(\theta) + \\ \sum_{\gamma=2}^{\xi} \mu_\gamma \dot{c}_\gamma - \sum_{\gamma=2}^{\xi} \operatorname{grad}(\mu_\gamma) \cdot \boldsymbol{j}_\gamma - \sum_{\gamma=2}^{\xi} \mu_\gamma \pi_\gamma \geq 0. \end{gathered} \tag{2.27}$$

- By inserting the set Λ of independent quantities into the free energy density, i.e. $\psi = \psi(\Lambda)$, relations between the Cauchy stress tensor $\boldsymbol{\sigma}$ and the free energy density ψ as well as the chemical potentials μ_γ and the free energy density ψ are derived. We call these results potential relations, which are assumed to be valid in both equilibrium and non-equilibrium conditions.
- Introducing the potential relations results in a dissipation inequality, which presents restrictions on the heat flux $\boldsymbol{q}_\theta$, the diffusion fluxes $\boldsymbol{j}_\gamma$ as well as the evolution equations for the internal variables $\dot{\underline{\alpha}}$. This dissipation inequality reads

$$-\frac{\partial \psi}{\partial \underline{\alpha}} \cdot \dot{\underline{\alpha}} - \sum_{\gamma=2}^{\xi} \operatorname{grad}(\mu_\gamma) \cdot \boldsymbol{j}_\gamma - \frac{1}{\theta} \boldsymbol{q}_\theta \cdot \operatorname{grad}(\theta) - \sum_{\gamma=2}^{\xi} \mu_\gamma \pi_\gamma \geq 0. \quad (2.28)$$

In Chapters 3 and 4, where we study different cases of hydrogen diffusion in metals, the entropy inequality (2.26) will be used to derive a constitutive theory. The same applies to Chapter 5, where the entropy inequality (2.26) will serve as a basis for the constitutive theory of a two-component system consisting of PA 6 and water.

Chapter 3

Hydrogen diffusion and embrittlement in elasto-plastically deforming metals

3.1 Introduction

In this chapter a novel scheme for the implementation of chemo-mechanically coupled processes in the commercial Finite-Element solver ABAQUS is presented. In contrast to previous publications, we use chemical potential as the degree of freedom for the chemical field. This choice has certain advantages, namely:

- Solving the diffusion equation for the concentration requires solving for a bounded solution variable, since the concentration is by definition greater than or equal to zero and bounded by a maximum concentration. Enforcing this inequality constraint is either numerically challenging (Lu et al., 2013) or impossible in commercial FEM packages. The chemical potential is, however, unbounded.
- The flux term in the diffusion equations relies on gradients of mechanical stresses, when the concentration is the chemical degree of freedom (Barrera et al., 2016). This necessitates the approximation of gradients of mechanical stresses on FEM meshes, which makes solutions mesh sensitive and less generally applicable. In addition, this results in the requirement of C^2-continuous functions to interpolate

the displacement field, as second order gradients of the displacements have to be computed. In contrast, when the chemical potential is the degree of freedom, this is avoided, as the flux is proportional to the gradient of the chemical potential.

- An open system, i.e. a system that is exposed to an atmosphere with a given partial pressure of the diffusing species, cannot be readily simulated in a concentration based setting, as the coupling of strains and concentrations at the system's boundary can only be computed sequentially (Fernández-Sousa et al., 2020). When the chemical potential is the degree of freedom this coupling is inherently incorporated at the system's boundary.

However, using concentration as the chemical degree of freedom allows using the often cited heat-transfer analogy, i.e. the analogy of the diffusion and heat-transfer equation, first presented by Oh et al. (2010) and later used, e.g., in Barrera et al. (2016), Díaz et al. (2016), Gobbi et al. (2019) and Fernández-Sousa et al. (2020). This analogy makes it possible to use the commercial FEM solver ABAQUS and a `coupled temperature-displacement` step to solve chemo-mechanically coupled processes. In contrast, Di Leo and Anand (2013) already proposed to use chemical potential as the degree of freedom. However, for the implementation, they rely on a `User-Defined-Element` (UEL). This implementation requires much more coding and lacks the flexibility of some of the basic built-in functionalities of ABAQUS, such as the visualization of results or the built-in element library.

These observations motivate the approach chosen in the present chapter. We use chemical potential as the chemical degree of freedom and introduce a novel heat-transfer analogy. We thus extend the well established analogy to a formulation where the chemical degree of freedom is the chemical potential. We apply this scheme to the process of hydrogen diffusion in a metal lattice, inspired by the model of Di Leo and Anand (2013). The proposed scheme is applicable to various two-field problems and was used in Dyck et al. (2024c) to study water diffusion in PA 6, c.f. Chapter 5. We note, that for the scheme to be applicable, the non-mechanical degree of freedom has to be scalar and its evolution has to be governed by a PDE similar to the heat-equation.

The remainder of this chapter is organized as follows: we start by deriving a closed set of fully coupled balance equations which fulfill thermodynamic restrictions in Sec. 3.2. To this end we focus on hydrogen embrittlement in metals as a model. Subsequently, a reformulation of the resulting diffusion equation is presented, see Sec. 3.3, followed by implementation details for the commercial Finite-Element solver ABAQUS in Sec. 3.4. We show some illustrative examples in Sec. 3.5 and conclude the chapter in Sec. 3.6.

3.2 Model

3.2.1 Preliminaries

In this section, we present a chemo-elasto-plastic coupled model in a thermodynamically consistent framework, which is later implemented in the commercial FEM solver ABAQUS. We explicitly work out the thermodynamic restrictions for all constitutive quantities imposed by the entropy inequality introduced in Chapter 2. We specify the model for hydrogen diffusion in elasto-plastically deforming metals. The diffusing species hydrogen can either reside in interstitial sites or trap sites. Trap sites are defects of the lattice structure, e.g., grain boundaries or dislocations, which provide space for the diffusing hydrogen within the host metal (Sofronis and McMeeking, 1989). This implies that the total number of components is three, namely the solid host metal, a concentration in moles per unit volume of hydrogen in lattice sites, denoted as c_{L} and a concentration in moles per unit volume of hydrogen in trap sites, denoted by c_{T}. Using constitutive theory, this is reduced to

two, such that a two-field problem results.
Before proceeding with the model presentation we want to point out that arbitrary two-field problems can be considered, as long as two requirements are fulfilled. The first requirement is, that the field being solved for is scalar. The second requirement is a second order PDE governing the evolution of the scalar field. In Chapter 5 we use the same methodology as in this Chapter and apply it to water diffusion in PA 6. In contrast, in Chapter 4, a PDE of order four governs the evolution of the additional scalar field, which necessitates a different approach for the implementation.

3.2.2 Balance equations

The balance equations for the diffusing hydrogen components are, c.f. Eq. (2.21) (1),

$$\begin{aligned} \dot{c}_{\mathrm{L}} &= -\mathrm{div}\left(\boldsymbol{j}_{\mathrm{L}}\right) + \pi_{\mathrm{L}\to\mathrm{T}}, \\ \dot{c}_{\mathrm{T}} &= -\mathrm{div}\left(\boldsymbol{j}_{\mathrm{T}}\right) + \pi_{\mathrm{T}\to\mathrm{L}}. \end{aligned} \tag{3.1}$$

Here the production terms $\pi_{\mathrm{L}\to\mathrm{T}}$ and $\pi_{\mathrm{T}\to\mathrm{L}}$ describe the fact that hydrogen atoms can switch from lattice sites to trap sites and vice versa. No further production terms are considered, such that $\pi_{\mathrm{L}\to\mathrm{T}} = -\pi_{\mathrm{T}\to\mathrm{L}}$. Changes in the total hydrogen concentration c result by summing up both contributions, i.e.

$$\dot{c} = \dot{c}_{\mathrm{L}} + \dot{c}_{\mathrm{T}} = -\mathrm{div}\left(\boldsymbol{j}_{\mathrm{L}}\right) - \mathrm{div}\left(\boldsymbol{j}_{\mathrm{T}}\right). \tag{3.2}$$

The quasi-static balance of linear momentum is, c.f. Eq. (2.21) (2),

$$\mathrm{div}\left(\boldsymbol{\sigma}\right) = \boldsymbol{0}. \tag{3.3}$$

The diffusion equations given in Eq. (3.1) and the relation between the production terms result in the balance of internal energy of the mixture

$$\begin{aligned} \dot{e} = \boldsymbol{\sigma} \cdot \dot{\boldsymbol{\varepsilon}} - \operatorname{div}\left(\boldsymbol{q}_\theta\right) + \omega + \mu_\mathrm{L}\dot{c}_\mathrm{L} + \mu_\mathrm{T}\dot{c}_\mathrm{T} - \\ \boldsymbol{j}_\mathrm{L} \cdot \operatorname{grad}\left(\mu_\mathrm{L}\right) - \boldsymbol{j}_\mathrm{T} \cdot \operatorname{grad}\left(\mu_\mathrm{T}\right). \end{aligned} \tag{3.4}$$

As we rely on the Coleman-Noll procedure, the balance of entropy of the mixture is

$$\dot{\eta} \geq -\operatorname{div}\left(\frac{\boldsymbol{q}_\theta}{\theta}\right) + \frac{\omega}{\theta}, \tag{3.5}$$

where the second law of thermodynamics of a non-negative entropy production density is used.

3.2.3 Thermodynamically consistent constitutive theory

For this three-component system, relying on the Coleman-Noll procedure, the entropy inequality results in, c.f. Eq. (2.26) and Eq. (2.27),

$$\begin{aligned} -\dot{\psi} - \eta\dot{\theta} + \boldsymbol{\sigma} \cdot \dot{\boldsymbol{\varepsilon}} - \frac{1}{\theta}\boldsymbol{q}_\theta \cdot \operatorname{grad}\left(\theta\right) + \mu_\mathrm{L}\dot{c}_\mathrm{L} + \mu_\mathrm{T}\dot{c}_\mathrm{T} - \\ \operatorname{grad}\left(\mu_\mathrm{L}\right) \cdot \boldsymbol{j}_\mathrm{L} - \operatorname{grad}\left(\mu_\mathrm{T}\right) \cdot \boldsymbol{j}_\mathrm{T} \geq 0. \end{aligned} \tag{3.6}$$

The set of independent variables Λ, on which the constitutive quantities depend is, in this context, $\Lambda = [\boldsymbol{\varepsilon}, c_\mathrm{L}, c_\mathrm{T}, \theta, \underline{\alpha}]$, where $\underline{\alpha}$ denotes internal variables, later specified to be plastic strains $\boldsymbol{\varepsilon}_\mathrm{p}$ and the equivalent plastic strain ε_eq. Inserting these independent variables in the free energy density, i.e. $\psi = \psi\left(\Lambda\right)$, and evaluating the time derivative of Eq. (3.6), we arrive at

$$\begin{aligned} \left(-\frac{\partial\psi}{\partial\boldsymbol{\varepsilon}} + \boldsymbol{\sigma}\right) \cdot \dot{\boldsymbol{\varepsilon}} - \left(\frac{\partial\psi}{\partial\theta} + \eta\right)\dot{\theta} + \left(-\frac{\partial\psi}{\partial c_\mathrm{L}} + \mu_\mathrm{L}\right)\dot{c}_\mathrm{L} + \\ \left(-\frac{\partial\psi}{\partial c_\mathrm{T}} + \mu_\mathrm{T}\right)\dot{c}_\mathrm{T} - \frac{\partial\psi}{\partial\underline{\alpha}} \cdot \dot{\underline{\alpha}} - \operatorname{grad}\left(\mu_\mathrm{L}\right) \cdot \boldsymbol{j}_\mathrm{L} - \\ \operatorname{grad}\left(\mu_\mathrm{T}\right) \cdot \boldsymbol{j}_\mathrm{T} - \frac{1}{\theta}\boldsymbol{q}_\theta \cdot \operatorname{grad}\left(\theta\right) \geq 0. \end{aligned} \tag{3.7}$$

This inequality has to hold for all thermodynamic processes. We deduce the potential relations

$$\begin{aligned} \boldsymbol{\sigma} &= \frac{\partial \psi}{\partial \boldsymbol{\varepsilon}}, \\ \eta &= -\frac{\partial \psi}{\partial \theta} \\ \mu_{\mathrm{L}} &= \frac{\partial \psi}{\partial c_{\mathrm{L}}}, \\ \mu_{\mathrm{T}} &= \frac{\partial \psi}{\partial c_{\mathrm{T}}}, \end{aligned} \tag{3.8}$$

which are assumed to be valid for equilibrium and non-equilibrium processes. The dissipation inequality remains as, c.f. Eq. (2.28),

$$-\frac{\partial \psi}{\partial \underline{\alpha}} \cdot \dot{\underline{\alpha}} - \operatorname{grad}(\mu_{\mathrm{L}}) \cdot \boldsymbol{j}_{\mathrm{L}} - \operatorname{grad}(\mu_{\mathrm{T}}) \cdot \boldsymbol{j}_{\mathrm{T}} - \frac{1}{\theta} \boldsymbol{q}_{\theta} \cdot \operatorname{grad}(\theta) \geq 0. \tag{3.9}$$

Eq. (3.8) implies that for a thermodynamically consistent theory we have to specify the free energy density $\psi(\Lambda)$. Eq. (3.9) presents restrictions for the fluxes $\boldsymbol{j}_{\mathrm{L}}, \boldsymbol{j}_{\mathrm{T}}$ and $\boldsymbol{q}_{\theta}$ as well as the evolution of the internal variables $\underline{\alpha}$.

The free energy density is additively decomposed into an elastic part ψ_{e} and a chemical part ψ_{c} as (Di Leo and Anand, 2013)

$$\psi = \psi_{\mathrm{e}}(\boldsymbol{\varepsilon}_{\mathrm{e}}) + \psi_{\mathrm{c}}(c_{\mathrm{L}}, c_{\mathrm{T}}, \theta). \tag{3.10}$$

As our model is specified for isothermal conditions, we neglect purely caloric contributions to the free energy density. In addition, no contribution to the free energy density due to the accumulation of plastic deformations is introduced. This implies, that the entire plastic work is dissipated as heat. However, as we consider isothermal cases, we neglect this temperature change. An approach to incorporate a partition of plastic power into stored and dissipated parts can be found in, e.g., Rosakis et al. (2000).

The elastic strains are

$$\boldsymbol{\varepsilon}_{\mathrm{e}} = \boldsymbol{\varepsilon} - \boldsymbol{\varepsilon}_{\mathrm{c}} - \boldsymbol{\varepsilon}_{\mathrm{p}}, \tag{3.11}$$

where $\boldsymbol{\varepsilon}_{\mathrm{p}}$ are plastic strains and $\boldsymbol{\varepsilon}_{\mathrm{c}}$ are chemical strains, which are

$$\boldsymbol{\varepsilon}_{\mathrm{c}} = \beta \, \Delta c \, \boldsymbol{I}. \tag{3.12}$$

This expresses an isotropic dilatation due to hydrogen in lattice and trap sites, depending linearly on the difference between the hydrogen concentration $c = c_{\mathrm{L}} + c_{\mathrm{T}}$ to a reference value $c_0 = c_{\mathrm{L}0} + c_{\mathrm{T}0}$, i.e. $\Delta c = c - c_0$. The hydrogen expansion coefficient of the host metal is β.
The elastic part of the free energy density is quadratic in the elastic strains and reads

$$\psi_{\mathrm{e}}\left(\boldsymbol{\varepsilon}_{\mathrm{e}}\right) = \frac{1}{2}\left(\boldsymbol{\varepsilon} - \boldsymbol{\varepsilon}_{\mathrm{c}} - \boldsymbol{\varepsilon}_{\mathrm{p}}\right) \cdot \mathbb{C}\left[\boldsymbol{\varepsilon} - \boldsymbol{\varepsilon}_{\mathrm{c}} - \boldsymbol{\varepsilon}_{\mathrm{p}}\right], \tag{3.13}$$

where $\mathbb{C} = 3K\mathbb{P}_1 + 2G\mathbb{P}_2$ is the isotropic stiffness tensor with compression modulus K and shear modulus G. The projectors $\mathbb{P}_1$ and $\mathbb{P}_2$ map onto spherical and deviatoric tensors of rank two, respectively.
The chemical part of the free energy density is additively split into parts comprising the mixing of hydrogen in lattice and trap sites. Both parts are computed via the entropy of mixing for an ideal gas in a regular solution as (DeHoff, 2006; Di Leo and Anand, 2013)

$$\begin{aligned}
\psi_{\mathrm{c}} &= \psi_{\mathrm{c,L}}(c_{\mathrm{L}}, \theta) + \psi_{\mathrm{c,T}}(c_{\mathrm{T}}, \theta) \\
\psi_{\mathrm{c,L}}(c_{\mathrm{L}}, \theta) &= \mu_{\mathrm{L}0} c_{\mathrm{L}} + R\theta N_{\mathrm{L}}\left(\vartheta_{\mathrm{L}} \ln\left(\vartheta_{\mathrm{L}}\right) + \left(1 - \vartheta_{\mathrm{L}}\right)\ln\left(1 - \vartheta_{\mathrm{L}}\right)\right), \\
\psi_{\mathrm{c,T}}(c_{\mathrm{T}}, \theta) &= \mu_{\mathrm{T}0} c_{\mathrm{T}} + R\theta N_{\mathrm{T}}\left(\vartheta_{\mathrm{T}} \ln\left(\vartheta_{\mathrm{T}}\right) + \right. \\
&\qquad \left. \left(1 - \vartheta_{\mathrm{T}}\right)\ln\left(1 - \vartheta_{\mathrm{T}}\right)\right).
\end{aligned} \tag{3.14}$$

Here $\mu_{\mathrm{L}0}$ as well as $\mu_{\mathrm{T}0}$ are reference chemical potentials of hydrogen in lattice and trap sites and ϑ_{L} as well as ϑ_{T} are the hydrogen occupancy in lattice and trap sites. They are normalized concentrations, defined by

$$\vartheta_{\mathrm{L}} = \frac{c_{\mathrm{L}}}{N_{\mathrm{L}}}, \quad \vartheta_{\mathrm{T}} = \frac{c_{\mathrm{T}}}{N_{\mathrm{T}}}, \tag{3.15}$$

where the densities of lattice and trap sites in moles per unit volume are N_{L} and N_{T}. These can be calculated via

$$\begin{aligned} N_{\mathrm{L}} &= \varphi \frac{\rho}{M_{\mathrm{M}}}, \\ N_{\mathrm{T}} &= N_{\mathrm{T}} \left(\varepsilon_{\mathrm{eq}}\right), \end{aligned} \tag{3.16}$$

with the number of lattice sites per metal atom φ, the mass density ρ of the metal and the molar mass of the host metal M_{M}. Eq. (3.16) (2), i.e. $N_{\mathrm{T}} \left(\varepsilon_{\mathrm{eq}}\right)$ implies, as indicated by measurements (Kumnick and Johnson, 1980), that the number of trap sites changes due to plastic deformation. This becomes obvious when we consider that the dislocation density increases by several orders of magnitude and thus the number of possible hydrogen sites increases. Kumnick and Johnson (1980) deduce the function

$$\log \left(N_{\mathrm{T}}\right) = 23.6 - 2.33 \exp \left(-5.5\, \varepsilon_{\mathrm{eq}}\right) \tag{3.17}$$

from measurements on iron based metals. The occupancies ϑ_{L} and ϑ_{T} are bounded, i.e. $\vartheta_{\mathrm{L,T}} \in [0, 1]$, for vanishing and maximum hydrogen concentration in lattice and trap sites.

The free energy density, c.f. Eq. (3.13) and Eq. (3.14), as well as the potential relations derived in Eq. (3.8) result in

$$\begin{aligned} \boldsymbol{\sigma} &= \mathbb{C} \left[\boldsymbol{\varepsilon} - \boldsymbol{\varepsilon}_{\mathrm{c}} - \boldsymbol{\varepsilon}_{\mathrm{p}}\right], \\ \mu_{\mathrm{L}} &= \mu_{\mathrm{L0}} + R\theta \ln \left(\frac{\vartheta_{\mathrm{L}}}{1 - \vartheta_{\mathrm{L}}}\right) - \beta \mathrm{tr} \left(\boldsymbol{\sigma}\right), \\ \mu_{\mathrm{T}} &= \mu_{\mathrm{T0}} + R\theta \ln \left(\frac{\vartheta_{\mathrm{T}}}{1 - \vartheta_{\mathrm{T}}}\right) - \beta \mathrm{tr} \left(\boldsymbol{\sigma}\right). \end{aligned} \tag{3.18}$$

The dissipative parts, i.e. plasticity, the diffusive fluxes as well as the heat flux are now introduced. We use a rate-independent, isotropic plasticity model after von Mises (1928). The yield condition is

$$\varphi(\boldsymbol{\sigma}', \varepsilon_{\mathrm{eq}}) = ||\boldsymbol{\sigma}'|| - \sqrt{\frac{2}{3}}\sigma_{\mathrm{F}}\left(\varepsilon_{\mathrm{eq}}\right) \leq 0, \tag{3.19}$$

where $\sigma_{\mathrm{F}}\left(\varepsilon_{\mathrm{eq}}\right)$ denotes the yield stress, which monotonically increases with $\varepsilon_{\mathrm{eq}}$. An associated plastic flow criterion leads to the evolution equation for plastic strains

$$\dot{\boldsymbol{\varepsilon}}_{\mathrm{p}} = \sqrt{\frac{3}{2}}\gamma\boldsymbol{N}, \tag{3.20}$$

where $\boldsymbol{N} = \boldsymbol{\sigma}'/\|\boldsymbol{\sigma}'\|$ is the direction of the Cauchy stress and γ is the consistency parameter. The evolution of accumulated plastic strain is computed based on

$$\dot{\varepsilon}_{\mathrm{eq}} = \sqrt{\frac{2}{3}}\gamma. \tag{3.21}$$

The consistency parameter evolves according to the Karush-Kuhn-Tucker conditions $\gamma \geq 0,\ \varphi \leq 0,\ \gamma\varphi = 0$ (Simo and Hughes, 1998). For the hardening function σ_{F} we rely on (Di Leo and Anand, 2013)

$$\sigma_{\mathrm{F}}\left(\varepsilon_{\mathrm{eq}}\right) = \sigma_{\mathrm{F0}}\left(\frac{\varepsilon_{\mathrm{eq}}}{\varepsilon_{\mathrm{p0}} + 1}\right)^{m}, \tag{3.22}$$

with an initial yield stress σ_{F0}, an exponent m and a reference strain $\varepsilon_{\mathrm{p0}}$. As we progress our the derivation of a thermodynamically consistent theory, we turn our attention towards the fluxes of heat $\boldsymbol{q}_{\theta}$ and hydrogen $\boldsymbol{j}_{\mathrm{L}}$ and $\boldsymbol{j}_{\mathrm{T}}$. Fourier's law is $\boldsymbol{q}_{\theta} = \kappa \mathrm{grad}\left(\theta\right)$. Similar to Fourier's law, an extension of Fick's law is used to model hydrogen fluxes, where the flux is proportional to the gradient of the chemical potential (Gurtin et al., 2010). The isotropic version reads

$$\boldsymbol{j}_{\mathrm{L}} = -m_{\mathrm{L}} \mathrm{grad}\left(\mu_{\mathrm{L}}\right), \quad \boldsymbol{j}_{\mathrm{T}} = -m_{\mathrm{T}} \mathrm{grad}\left(\mu_{\mathrm{T}}\right), \tag{3.23}$$

where $m_{\mathrm{L}} \geq 0$ and $m_{\mathrm{T}} \geq 0$ are the mobility of the diffusing hydrogen in lattice and trap sites. In agreement with literature for hydrogen diffusion, c.f. Sofronis and McMeeking (1989), Di Leo and Anand (2013) and Díaz et al. (2016), we assume the mobility of hydrogen in trap sites to vanish, i.e. $m_{\mathrm{T}} = 0$. This leads to a vanishing hydrogen flux in trap sites, i.e. $\boldsymbol{j}_{\mathrm{T}} = \mathbf{0}$, making the notion of hydrogen trapping clear. The mobility in lattice sites depends on the temperature θ, the diffusion coefficient $D \geq 0$, the ideal gas constant R and the lattice concentration c_{L} via (Anand, 2012)

$$m_{\mathrm{L}} = \frac{D}{R\theta} c_{\mathrm{L}} \left(1 - \vartheta_{\mathrm{L}}\right). \tag{3.24}$$

This formulation leads to a vanishing mobility for $c_{\mathrm{L}} = 0$ and $\vartheta_{\mathrm{L}} = 1$. The final part of the constitutive theory is the introduction of Oriani's equilibrium (Oriani, 1970; 1978)

$$\mu_{\mathrm{L}} = \mu_{\mathrm{T}}. \tag{3.25}$$

As outlined in the next section, this equilibrium implies that only one additional component has to be considered explicitly in the following. All quantities for the other component follow the constitutive theory outline above. We choose, in agreement with Di Leo and Anand (2013), the component related to lattice sites as the degree of freedom.

3.3 Reformulation of the diffusion equation

At this point the diffusion Eq. (3.2) is still specified for changes in the hydrogen concentrations c_{L} and c_{T}. As one of the main objectives of this chapter is the development of a theory using chemical potential as the chemical degree of freedom, we reformulate the diffusion equation. For $\boldsymbol{j}_{\mathrm{T}} = \mathbf{0}$, changes in total hydrogen concentration are expressed as

$$\dot{c}_{\mathrm{L}} + \dot{c}_{\mathrm{T}} = \operatorname{div}\left(m_{\mathrm{L}} \operatorname{grad}\left(\mu_{\mathrm{L}}\right)\right). \tag{3.26}$$

From Oriani's equilibrium in Eq. (3.25) an analytic relation between the hydrogen occupancy in lattice and in trap sites can be derived. This relation is

$$\vartheta_{\mathrm{T}} = \frac{K_{\mathrm{T}} \vartheta_{\mathrm{L}}}{\left(K_{\mathrm{T}} - 1\right) \vartheta_{\mathrm{L}} + 1}, \tag{3.27}$$

where $K_{\mathrm{T}} = \exp\left(\left(\mu_{\mathrm{L}0} - \mu_{\mathrm{T}0}\right)/R/\theta\right)$. Inserting the relations between hydrogen occupancy and concentration, i.e. $c_{\mathrm{T}} = N_{\mathrm{T}} \vartheta_{\mathrm{T}}$ and $c_{\mathrm{L}} = N_{\mathrm{L}} \vartheta_{\mathrm{L}}$, we arrive at a relation between concentrations in trap and lattice sites. We now proceed by deriving a relation between $\dot{\mu}_{\mathrm{L}}$ and $\dot{c}_{\mathrm{L}}$. Using Eq. (3.27) we conclude

$$\begin{aligned}
\dot{c}_{\mathrm{T}} &= \frac{\partial c_{\mathrm{T}}}{\partial c_{\mathrm{L}}} \dot{c}_{\mathrm{L}} + \frac{\partial c_{\mathrm{T}}}{\partial \varepsilon_{\mathrm{eq}}} \dot{\varepsilon}_{\mathrm{eq}}, \\
\frac{\partial c_{\mathrm{T}}}{\partial c_{\mathrm{L}}} &= \frac{c_{\mathrm{T}}}{c_{\mathrm{L}}} \left(\frac{N_{\mathrm{L}}}{\left(K_{\mathrm{T}} - 1\right) c_{\mathrm{L}} + N_{\mathrm{L}}} \right), \\
\frac{\partial c_{\mathrm{T}}}{\partial \varepsilon_{\mathrm{eq}}} &= \vartheta_{\mathrm{T}} \frac{\mathrm{d} N_{\mathrm{T}}}{\mathrm{d} \varepsilon_{\mathrm{eq}}}.
\end{aligned} \tag{3.28}$$

The next step is taking the time derivative of Eq. (3.18) (2), which yields

$$\dot{\mu}_{\mathrm{L}} = \frac{R\theta}{c_{\mathrm{L}}} \frac{\dot{c}_{\mathrm{L}}}{1 - \vartheta_{\mathrm{L}}} - \beta \operatorname{tr}\left(\dot{\boldsymbol{\sigma}}\right). \tag{3.29}$$

The rearrangement of Eq. (3.29) for $\dot{c}_{\mathrm{L}}$ allows us, together with Eq. (3.28), to reformulate Eq. (3.26) as a balance equation for the chemical potential in lattice sites. Introducing

$$\begin{aligned} D^* &= \frac{c_\mathrm{T}}{c_\mathrm{L}} \left(\frac{N_\mathrm{L}}{\left(K_\mathrm{T} - 1\right) c_\mathrm{L} + N_\mathrm{L}} \right), \\ D^{**} &= \left(1 - \vartheta_\mathrm{L}\right) \left(D^* + 1\right) \end{aligned} \tag{3.30}$$

to shorten the notation, we finally arrive at a balance equation for the chemical potential in lattice sites

$$D^{**} \frac{c_\mathrm{L}}{R\theta} \dot{\mu}_\mathrm{L} = \mathrm{div}\left(m_\mathrm{L} \mathrm{grad}\left(\mu_\mathrm{L}\right)\right) - D^{**} \frac{c_\mathrm{L}}{R\theta} \beta \mathrm{tr}\left(\dot{\boldsymbol{\sigma}}\right) - \vartheta_\mathrm{T} \frac{\mathrm{d}N_\mathrm{T}}{\mathrm{d}\varepsilon_\mathrm{eq}} \dot{\varepsilon}_\mathrm{eq}. \tag{3.31}$$

Boundary conditions for this balance equation are either specified directly for the chemical potential in lattice sites μ_L (Dirichlet boundary conditions), or the flux (Neumann boundary conditions).
The choice of the chemical potential in lattice sites as the chemical degree of freedom allows us to simulation so-called open systems, which are exposed to an atmosphere with a partial hydrogen gas pressure. Using the concentration, this is not possible, as the coupling between strains and concentrations at the system's boundary, c.f. Eq. (3.18) (2), can not be considered. Following Di Leo and Anand (2013), we propose to apply such a boundary condition by equating $\overline{\mu}_\mathrm{L}$ with the chemical potential of gaseous hydrogen by (Di Leo and Anand, 2013)

$$\overline{\mu}_\mathrm{L} = \frac{1}{2} \mu_\mathrm{H2} = \mu^0_\mathrm{H2} + R\theta \ln \left(\frac{f_\mathrm{H2}}{p^0} \right), \tag{3.32}$$

with reference chemical potential of gaseous H2 μ^0_H2, fugacity f_H2 and reference pressure p^0. From our perspective, it is important to note that a constant chemical potential at the boundary is different from a constant concentration at the boundary, as the relation of μ_L and c_L depends on the stress state $\boldsymbol{\sigma}$, c.f. Eq. (3.18) (2). The set of coupled equations is the quasi-static balance of linear momentum, c.f. Eq. (2.21) (2), and Eq. (3.31). In the next section, an analogy between Eq. (3.31) and the heat-equation implemented in the commercial Finite-Element solver ABAQUS is proposed, in order to solve the equations describing the diffusion of hydrogen in lattice and trap sites coupled to elasto-plastic deformations of the host metal.

3.4 Heat-Transfer analogy[1]

In ABAQUS, the heat-equation being solved is (Smith, 2009)

$$\dot{e} = -\mathrm{div}\left(\boldsymbol{q}_\theta\right) + w. \tag{3.33}$$

The left-hand side of the equation is the rate of change of the internal energy density $\dot{e}$, which occurs due to heat fluxes $\boldsymbol{q}_\theta$ and a term accounting for a heat source density and heat production w. In the following, we call w heat source density. When the analogies presented in Tab. 3.1 are considered, the diffusion Eq. (3.31) is identical to the heat-equation and built-in ABAQUS procedures can be used to study diffusion driven by gradients in the chemical potential. Using the proposed analogy, we interpret $D^{**}c_\mathrm{L}\dot{\mu}_\mathrm{L}/R/\theta$ as the rate of change of the internal energy density, while the heat source density is $w = -D^{**}c_\mathrm{L}\mathrm{tr}\left(\dot{\boldsymbol{\sigma}}\right)/R/\theta - \vartheta_\mathrm{T}\dot{\varepsilon}_\mathrm{eq}\,\mathrm{d}N_\mathrm{T}/\,\mathrm{d}\varepsilon_\mathrm{eq}$ and the heat flux is $\boldsymbol{q}_\theta = m_\mathrm{L}\mathrm{grad}\left(\mu_\mathrm{L}\right)$.

A version of this analogy has been previously used in the context of hydrogen diffusion in metals (Oh et al., 2010; Barrera et al., 2016). In contrast to these studies, the scheme outlined in this chapter relies on the chemical potential of hydrogen in lattice sites μ_L as the nodal degree of freedom instead of the concentration which offers the advantages outlined in Sec. 3.1. To exploit the heat-transfer analogy, the user

---

[1] Section 3.4 is adapted from the appendix of the publication "Modeling and FE simulation of coupled water diffusion and viscoelasticity in relaxation tests of polyamide 6" (Dyck et al., 2024c), c.f. also Chapter 5. The original content has been adapted to the multi-component system considered in this chapter, i.e. formulas have been modified. Several passages have been extended.

subroutines `UMAT` and `UMATHT` are used. ABAQUS calls the subroutines `UMAT` and `UMATHT` consecutively at each integration point for each increment of the solution procedure.

	Heat-equation	Diffusion equation
Equation number	(3.33)	(3.31)
Degree of freedom	θ	μ_{L}
`FLUX`	$\boldsymbol{q}$	$m_{\mathrm{L}} \mathrm{grad}\left(\mu_{\mathrm{L}}\right)$
$\dot{\mathtt{U}}$	$\dot{e}$	$D^{**} \frac{c_{\mathrm{L}}}{R\theta} \dot{\mu}_{\mathrm{L}}$
`RPL`	w	$-D^{**} \frac{c_{\mathrm{L}}}{R\theta} \mathrm{tr}\left(\dot{\boldsymbol{\sigma}}\right) - \vartheta_{\mathrm{T}} \frac{\mathrm{d}N_{\mathrm{T}}}{\mathrm{d}\varepsilon_{\mathrm{eq}}} \dot{\varepsilon}_{\mathrm{eq}}$

Table 3.1: Analogy of heat and diffusion equation. Table adapted from Table 4 from Dyck et al. (2024c). The `FLUX`, $\dot{\mathtt{U}}$ and `RPL` term in the third column have been adapted to the multi-component system considered in this chapter.

Within the subroutines, the internal energy is called `U`, the heat flux is `FLUX`, the heat source density is `RPL`, and internal variables are stored in the vector `statev`. The user has to specify the material response to the increments $\Delta\mu_{\mathrm{L}}$ and $\Delta\boldsymbol{\varepsilon}$ by computing all constitutive quantities at the end of the increment[2]. In the constitutive framework outlined in Sec. 3.2, the quantities to be defined by the user are stresses $\boldsymbol{\sigma}^{n+1}$, internal variables $\underline{\alpha}^{n+1}$ (i.e., the plastic strains and the equivalent plastic strain), the concentration of hydrogen in lattice sites c_{L}^{n+1}, the concentration of hydrogen in trap sites c_{T}^{n+1} as well as the hydrogen flux $\boldsymbol{j}_{\mathrm{L}}^{n+1}$[3]. In addition, the heat source density `RPL` and the updated internal energy `U` have to be computed. The computation within the subroutine `UMAT` is used to update the `statev` vector as well as the stresses and the

---

[2] Quantities at the end of the increment will be marked with the superscript $(.)^{n+1}$.

[3] We store both the internal variables $\underline{\alpha}$ as well as the concentrations in lattice and trap sites c_{L} and c_{T} in the vector `statev`.

heat source density `RPL`. In the subroutine `UMATHT`, `FLUX` and `U` are computed. In addition to the constitutive quantities, tangents have to be computed for the global Newton method of ABAQUS, i.e., derivatives with respect to the solution variables μ_{L} and $\boldsymbol{u}$. The necessary tangents to be computed are

$$\begin{aligned} \texttt{DDSDDE} &= \frac{\partial \boldsymbol{\sigma}}{\partial \boldsymbol{\varepsilon}}, \quad \texttt{DDSDDT} = \frac{\partial \boldsymbol{\sigma}}{\partial \mu_{\mathrm{L}}}, \\ \texttt{DRPLDE} &= \frac{\partial \texttt{RPL}}{\partial \boldsymbol{\varepsilon}}, \quad \texttt{DRPLDT} = \frac{\partial \texttt{RPL}}{\partial \mu_{\mathrm{L}}}, \end{aligned} \tag{3.34}$$

for the `UMAT` subroutine and

$$\begin{aligned} \texttt{DUDT} &= \frac{\partial\, \texttt{U}}{\partial \mu}, \quad \texttt{DUDG} = \frac{\partial\, \texttt{U}}{\partial\, \mathrm{grad}\,(\mu)}, \\ \texttt{DFDT} &= \frac{\partial\, m\, \mathrm{grad}\,(\mu)}{\partial \mu}, \quad \texttt{DFDG} = \frac{\partial\, m\, \mathrm{grad}\,(\mu)}{\partial\, \mathrm{grad}\,(\mu)}, \end{aligned} \tag{3.35}$$

for the `UMATHT` subroutine. All tangents can be computed analytically for the model presented in this chapter. When the tangents are not, or are incorrectly supplied, the convergence of the global Newton's method to compute $\Delta\mu_{\mathrm{L}}$ and $\Delta\boldsymbol{u}$ is severely slowed down. A schematic of the usage of these subroutines is depicted in Fig. 3.1. We want to point out that the global solver computes an increment in the displacements. However, in the subroutine, an increment in the infinitesimal strain tensor $\Delta\boldsymbol{\varepsilon}$ is supplied, c.f. Fig. 3.1.

We now proceed by summarizing the necessary computations within the `UMAT` subroutine. We use an implicit time integration scheme to integrate the chemo-elasto-plastic constitutive theory at each integration point. This results in $\boldsymbol{\sigma}$, the internal variables $\underline{\alpha}$, c_{L} and c_{T}[4]. In total there are 15 unknown quantities. As the chemically induced strains are spherical

---

[4] To shorten notation we do not write $(.)^{\mathrm{n}+1}$ and instead only use $(.)^{\mathrm{n}}$, to specify results from the previous converged increment in the following.

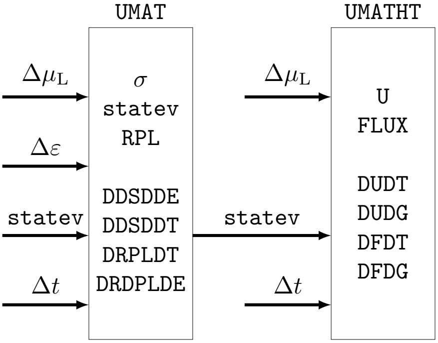

Figure 3.1: Schematic display of the interplay of the used subroutines. `UMAT` is called first and used to define stresses $\boldsymbol{\sigma}$, updated internal variables $\underline{\alpha}$ and $c_\mathrm{L}, c_\mathrm{T}$ and N_T, which are summarized in the vector `statev`. The heat source density is calculated and saved in `RPL`. In addition, several tangents are computed, i.e. the derivatives detailed in Eq. (3.34). `UMATHT` is called subsequently and used to update the internal energy `U` as well as the heat flux `FLUX`. The `statev` vector is already updated in the `UMAT`. Tangents are computed as detailed in Eq. (3.35). Figure adapted from Figure 6 from Dyck et al. (2024c). The input variables to each subroutine were modified for the multi-component system considered in this chapter.

they do not interfere with the plasticity theory. Thus, c_L as well as c_T can be computed independently of $\boldsymbol{\varepsilon}_\mathrm{p}$ and ε_eq. Using a radial return method, c.f. Simo and Hughes (1998), the inelastic time-integration scheme can be reduced to a single unknown, i.e. the plastic multiplier γ. The scalar residual equation r_ε to be solved is

$$r_\varepsilon = \sqrt{\frac{3}{2}}\|\boldsymbol{\sigma}'_\mathrm{TR}\| - 2G\Delta\gamma - \sigma_\mathrm{F}\left(\varepsilon^n_\mathrm{eq} + \sqrt{\frac{2}{3}}\Delta\gamma\right) = 0, \tag{3.36}$$

where $\boldsymbol{\sigma}'_\mathrm{TR} = 2G\left(\boldsymbol{\varepsilon} - \boldsymbol{\varepsilon}^n_\mathrm{p}\right)$ is the deviatoric trial stress, which is computed based on the assumption that there are no plastic deformations in the current increment. The solution of this scalar residual equation is retrieved by means of Newton's method. Subsequently c_L and c_T can be computed. This is done by solving the residual equation

$$\begin{aligned} r_\vartheta = & -\mu_\mathrm{L} + \mu_\mathrm{L0} + R\theta \ln\left(\frac{\vartheta_\mathrm{L}}{1-\vartheta_\mathrm{L}}\right) \\ & - \beta \mathrm{tr}\left(\mathbb{C}\left[\boldsymbol{\varepsilon} - \beta\left(N_\mathrm{L}\vartheta_\mathrm{L} + N_\mathrm{T}\vartheta_\mathrm{T}\right)\right]\right) = 0, \end{aligned} \tag{3.37}$$

for the lattice occupancy ϑ_L. This is Eq. (3.18) (2) rearranged to an implicit equation. Again, Newton's method is used to solve this scalar residual equation for ϑ_L, while Eq. (3.27) relates ϑ_T to ϑ_L. The solution to this equation is bounded by $\vartheta_\mathrm{L} \in [0, 1]$. This inequality constraint can be ensured by projecting the Newton update to be within these bounds, not affecting the convergence rate (Nesterov, 2004). We once again want to remind the reader, that this is a specific advantage of using the chemical potential as the degree of freedom, as the global solver of ABAQUS can not enforce this inequality constraint for the concentration.

As soon as the plastic strains and the concentrations are known, stresses $\boldsymbol{\sigma}$ as well as the heat source density `RPL` can be computed as

$$\begin{aligned} \boldsymbol{\sigma} &= \mathbb{C}\left[\boldsymbol{\varepsilon} - \boldsymbol{\varepsilon}_\mathrm{p} - \beta\left(c_\mathrm{L} + c_\mathrm{T}\right)\boldsymbol{I}\right], \\ \mathtt{RPL} &= -D^{**}\frac{c_\mathrm{L}}{R\theta}\mathrm{tr}\left(\dot{\boldsymbol{\sigma}}\right) - \vartheta_\mathrm{T}\frac{\mathrm{d}N_\mathrm{T}}{\mathrm{d}\varepsilon_\mathrm{eq}}\dot{\varepsilon}_\mathrm{eq}. \end{aligned} \tag{3.38}$$

We approximate $\mathrm{tr}\left(\dot{\boldsymbol{\sigma}}\right) \approx \mathrm{tr}\left(\boldsymbol{\sigma} - \boldsymbol{\sigma}^\mathrm{n}\right)/\Delta t$ and $\dot{\varepsilon}_\mathrm{eq} \approx \Delta\varepsilon_\mathrm{eq}/\Delta t$ using an implicit Euler time integration scheme.

We now proceed to presenting the computations in the subroutine `UMATHT`. Besides the updated internal energy density `U` and the heat flux `FLUX`, certain tangents have to be computed in `UMATHT`. These are `DUDT` (change in internal energy due to a change in μ_L), `DUDG` (change in internal energy due to $\mathrm{grad}\left(\mu_\mathrm{L}\right)$), `DFDT` (change of heat flux due to a change in μ_L) and `DFDG` (change in flux due to $\operatorname{grad}(\mu_\mathrm{L})$). We compute

$$\begin{aligned}\mathtt{U} &= \mathtt{U}^\mathrm{n} + \Delta t D^{**} \frac{c_\mathrm{L}}{R\theta} \dot{\mu}_\mathrm{L}, \\ \mathtt{FLUX} &= -m_\mathrm{L}\, \mathtt{DTEMDX},\end{aligned} \tag{3.39}$$

where, as above, $\dot{\mu}_\mathrm{L} \approx \Delta\mu_\mathrm{L}/\Delta t$. The gradient of the chemical potential is $\mathtt{DTEMDX} = \operatorname{grad}(\mu_\mathrm{L})$, which is supplied by ABAQUS. This means that we do not have to compute gradient terms manually, which is a significant advantage compared to the implementations presented in Díaz et al. (2016), Barrera et al. (2016), Gobbi et al. (2019) and Fernández-Sousa et al. (2020). In these works, approximations and the shape functions are used to compute $\operatorname{grad}(\operatorname{tr}(\boldsymbol{\sigma}))$, which requires a new implementation for every chosen element type and shape function.

3.5 Applications

3.5.1 Preliminaries

In this section, we use the model and implementation scheme presented in this chapter to first validate the scheme (inspired by Barrera et al. (2016)) and subsequently investigate the frequently studied case of a blunting crack tip in the presence of hydrogen, studied, e.g., by Sofronis and McMeeking (1989), Di Leo and Anand (2013), Díaz et al. (2016) and Fernández-Sousa et al. (2020). All material parameters used are summarized in Tab. 3.2.

3.5.2 Simple diffusion

We start by validating the proposed heat-transfer analogy and our implementation of the diffusion equation. To this end, a rectangular bar of length l is considered. We neglect all deformations and set the

R	$8.314\,\mathrm{J/mol/K}$	E	$207\,\mathrm{GPa}$
N_{Avo}	$6.0221 \times 10^{23}\,\mathrm{1/mol}$	ν	0.3
θ	$300\,\mathrm{K}$	σ_{F0}	$250\,\mathrm{MPa}$
N_{L}	$8.47 \times 10^{5}\,\mathrm{mol/m^3}$	$\varepsilon_{\mathrm{p0}}$	σ_{F0}/E
D	$1.27 \times 10^{-8}\,\mathrm{m^2/s}$	m	0.2
μ_{L0}	$28.6\,\mathrm{kJ/mol}$	β	$6.67 \times 10^{-5}\,\mathrm{m^3/mol}$
μ_{T0}	$-31.4\,\mathrm{kJ/mol}$		

Table 3.2: Material parameters used in all simulations of this section, taken from Di Leo and Anand (2013). The lattice diffusion coefficient D has been corrected by two orders of magnitude to conform with the simulations of Krom et al. (1999) and others.

number of trap sites to zero, implying $c_{\mathrm{T}} = 0$. We, thus, solve a diffusion equation

$$(1 - \vartheta_{\mathrm{L}}) \frac{c_{\mathrm{L}}}{R\theta} \dot{\mu}_{\mathrm{L}} = -\mathrm{div}\left(-\frac{Dc_{\mathrm{L}}}{R\theta} (1 - \vartheta_{\mathrm{L}})\, \mathrm{grad}\,(\mu_{\mathrm{L}}) \right), \tag{3.40}$$

using the scheme outlined above.

An analytical benchmark solution can be obtained by simplifying Eq. (3.40) to the classical diffusion equation

$$\dot{\vartheta}_{\mathrm{L}} = \mathrm{div}\,(D\mathrm{grad}\,(\vartheta_{\mathrm{L}}))\,. \tag{3.41}$$

For initial conditions $\vartheta_{\mathrm{L}}(x,0) = \vartheta_0, \forall x \in (0,l)$ and boundary conditions $\vartheta_{\mathrm{L}}(0,t) = \vartheta_1$, $\vartheta_{\mathrm{L}}(l,t) = \vartheta_2$ the analytic solution is (Crank, 1979)

$$\begin{gathered}\vartheta_{\mathrm{L}}(x,t) = \vartheta_1 + (\vartheta_2 - \vartheta_1)\frac{x}{l} - \\ \sum_{i=1}^{\infty} \left(\frac{2\left((\vartheta_0 - \vartheta_2)(-1)^i - \vartheta_0 + \vartheta_1\right) \sin\left(\frac{i\pi x}{l}\right)}{\exp\left(\frac{D_{\mathrm{L}}\pi^2 i^2 t}{l^2}\right) i\pi} \right).\end{gathered} \tag{3.42}$$

For the numerical simulation, we impose an initial chemical lattice potential of $\mu_{\mathrm{L}}(x,0) = -1.0\,\mathrm{kJ/mol}$, corresponding to $\vartheta_{\mathrm{L0}} = 0.4$. The boundary values are $\mu_{\mathrm{L}}(0,t) = -5.5\,\mathrm{kJ/mol}$ and $\mu_{\mathrm{L}}(l,t) = 2.1\,\mathrm{kJ/mol}$, such that $\vartheta_\mathrm{L}(0) = 0.1$ and $\vartheta_\mathrm{L}(l) = 0.7$. On all sides of the bar a no-flux boundary condition is prescribed. Due to the boundary conditions, the problem solved is one-dimensional. The length of the bar is chosen to be $l = 50\,\mathrm{mm}$. The bar is discretized using linear heat-conduction elements (DC3D8) with an edge length of $1\,\mathrm{mm}$ and a `heat transfer` step is used.

A comparison of the numerically obtained solution and the analytic solution is depicted in Fig. 3.2 a) and b) for $t = 1000\,\mathrm{s}, t = 5000\,\mathrm{s}$ and $t = 10000\,\mathrm{s}$. In Fig. 3.2 a) the absolute values of the lattice occupancy are depicted, while in Fig. 3.2 b) the relative difference between the numerically obtained solution and the analytic solution is shown. The results match exceptionally well for all time steps, which proves, that the instationary solution to the diffusion equation can be obtained by the presented scheme.

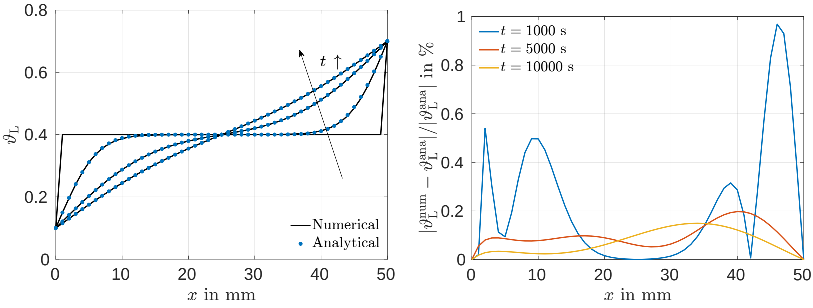

(a) **(b)**

Figure 3.2: Comparison of the analytic and numerical solution to the simple diffusion Eq. (3.41) for three time steps. a) Absolute values, including the initial lattice occupancy. b) Relative difference in %.

3.5.3 Semi-coupled process

The next investigation aims to validate the coupling between deformations and a redistribution of hydrogen atoms. Again, no defects are considered and both plastic and chemical strains are neglected. This implies that the chemical degree of freedom does not influence the mechanical degree of freedom. However, an inhomogeneous stress distribution can lead to a diffusion of hydrogen due to the stress-dependent term in the diffusion equation. A notched plate in plane strain setting, depicted in Fig. 3.3 a) with edge length $l = 500\,\mathrm{mm}$ and notch radius $a = 4\,\mathrm{mm}$, is considered. In the first simulation step, a traction boundary condition $\sigma_0 = 50\,\mathrm{MPa}$ in $\boldsymbol{e}_y$-direction is applied. Initially the chemical potential and concentration in lattice sites are homogeneous and the plate is stress free. The initial lattice occupancy is $\vartheta_{\mathrm{L}0} = 0.1$. Due to the notch, the stress state becomes inhomogeneous, leading to a redistribution of hydrogen atoms. As noted by Barrera et al. (2016), the stress state around a notched plate is known in a cylindrical coordinate system, c.f. Kirsch (1898),

$$\begin{aligned}\sigma_{rr} &= 0,\\ \sigma_{r\varphi} &= 0,\\ \sigma_{\varphi\varphi}(\varphi) &= \sigma_0\left(1 - 2\cos\left(2\varphi\right)\right).\end{aligned}\tag{3.43}$$

Due to the plane strain setting $\sigma_{zz} = \nu\sigma_{\varphi\varphi}$, where ν is Poisson's ratio. Thus, the trace of the stress tensor along the notch radius can be computed to be $\mathrm{tr}(\boldsymbol{\sigma}) = (1+\nu)\sigma_{\varphi\varphi}(\varphi)$. In the second simulation step, the boundary condition is held constant and the hydrogen is allowed to diffuse until the chemical potential in lattice sites is homogeneous again. Due to the heterogeneous stress state, the resulting occupancy distribution is heterogeneous as well. Building upon the known stress

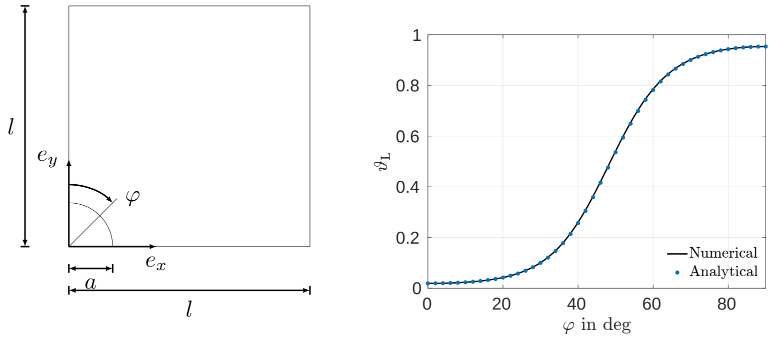

(a) **(b)**

Figure 3.3: Semi-coupled chemo-mechanical process. (a) The simulation domain is a notched plate. A traction boundary condition in e_y-direction is applied. (b) The numerically obtained occupancy distribution along the notch radius is shown in addition to the analytic solution.

state this can be analytically expressed as

$$\vartheta_{\mathrm{L}} = \frac{\exp\left(\frac{\mu_{\mathrm{L}}(\vartheta_{\mathrm{L}0})+\beta(1+\nu)\sigma_{\varphi\varphi}(\varphi)}{R\theta}\right)}{\exp\left(\frac{\mu_{\mathrm{L}}(\vartheta_{\mathrm{L}0})+\beta(1+\nu)\sigma_{\varphi\varphi}(\varphi)}{R\theta}\right)+1}. \tag{3.44}$$

We discretize the notched plate with linear, hexahedral coupled temperature displacement elements (C3D8T). Around the notch a high mesh resolution is used, which becomes coarser in a sufficient distance to the notch. The two simulation steps are prescribed using a `coupled temperature-displacement` step.

In Fig. 3.3 b) a comparison between the analytical and numerically obtained solution is shown at the end of step two. Again, as in the case of the simple diffusion, both results are in exceptional agreement. We thus conclude that the proposed scheme is indeed capable of predicting a concentration redistribution due to a heterogeneous stress state as well as an instationary diffusion problem.

3.5.4 Blunting crack tip

The final application is a comparison of results obtained using our implementation scheme to previously published results. We, therefore, study a blunting crack tip in the presence of hydrogen. Sofronis and McMeeking (1989) were the first to study this problem. Numerous publications (e.g., Krom et al. (1999); Di Leo and Anand (2013)) presented new theories or implementation strategies. The simulation domain is a blunting crack tip, c.f. Fig. 3.4 a), studied in a plane strain setting. Plastic deformations are confined to a small area around the crack tip (or notch). A displacement field is applied remotely and ramped up incrementally. In a second simulation step the displacement is held constant for a long time, i.e. $1 \times 10^6\,\mathrm{s}$ to study the diffusion processes in the vicinity of the crack tip, where inelastic deformations and large stress gradients occur. The applied displacement field for crack mode I is

$$\begin{aligned} u_x &= \frac{K_\mathrm{I}}{2G}\sqrt{\frac{R}{2\pi}}\cos\left(\frac{\varphi}{2}\right)\left(2 - 4\nu + 2\sin\left(\frac{\varphi}{2}\right)^2\right), \\ u_y &= \frac{K_\mathrm{I}}{2G}\sqrt{\frac{R}{2\pi}}\sin\left(\frac{\varphi}{2}\right)\left(4 - 4\nu - 2\cos\left(\frac{\varphi}{2}\right)^2\right), \end{aligned} \tag{3.45}$$

where R and φ are polar coordinates as depicted in Fig. 3.4 a). The stress intensity factor K_I is taken from linear elastic fracture mechanics (Sofronis and McMeeking, 1989). All our boundary and initial conditions match the ones chosen in Di Leo and Anand (2013) and are briefly summarized in the following. We set $b_0 = 10\,\mu\mathrm{m}$ and $c_{\mathrm{L}0} = 3.46 \times 10^{-3}\,\mathrm{mol/m^3}$. As the domain is initially stress free, this initial concentration results in a boundary chemical potential of $\bar{\mu}_\mathrm{L} = -19.576\,\mathrm{kJ/mol}$ according to Eq. (3.32). This value is prescribed in the crack tip and at the surface where the displacements are applied. We model half of the crack and prescribe symmetry boundary conditions at the bottom. The front and back side are traction-free and the hydrogen flux $\boldsymbol{j}_{\mathrm{L}}$ vanishes. We discretize the structure with approximately 27000 linear, hexahedral coupled temperature-displacement elements (C3D8T). The implementation of the given displacement field requires usage of the subroutine `DISP` of ABAQUS, as pointed out, e.g., by Fernández-Sousa et al. (2020). Our results, c.f. Fig. 3.4 b), are similar to the results presented by Di Leo and Anand (2013). We want to emphasize the difference between initial lattice concentration $c_{\mathrm{L}0}$ and lattice concentration at the crack tip right after loading, which can only be obtained by simulating an open system. Using c_{L} as the chemical degree of freedom would not allow to retrieve this solution, as the concentration would remain equal to the boundary value. As proposed by Krom et al. (1999), an analytic solution to the hydrogen lattice concentration in steady state, i.e. for 1×10^6 s, ahead of the crack tip can be retrieved. This is depicted in comparison to the FEM solution in steady state, showing perfect alignment.

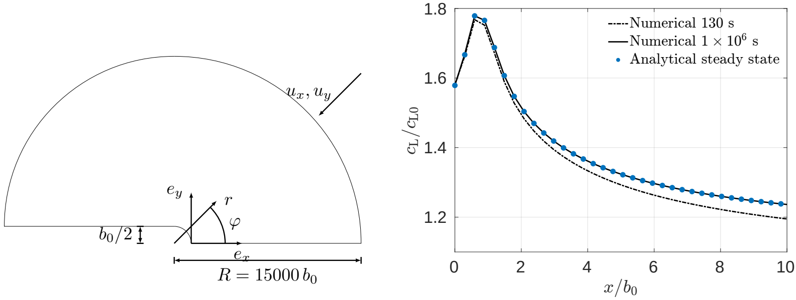

(a) **(b)**

Figure 3.4: Fully coupled chemo-mechanical process. (a) Blunting Crack Tip with applied displacement field. (b) Normalized concentration distribution ahead of the crack tip. Distributions after loading ($t = 130\,\mathrm{s}$) and in steady state ($t = 1 \times 10^6$ s) are presented in addition to the analytic solution.

3.6 Conclusion

In this chapter we presented a multi-component system, considering three components. To this end, hydrogen diffusion to lattice and trap sites coupled to elasto-plastic deformations of a host metal were considered. The model equations and the thermodynamic considerations were presented in detail, following the Coleman-Noll procedure outlined in Chapter 2. Subsequently, we reformulated the diffusion equation for an advantageous degree of freedom, namely the chemical potential. For this reformulated set of coupled balance equations we presented a heat-transfer analogy, allowing us to use the commercial FEM solver ABAQUS to study chemo-mechanically coupled processes with chemical potential as the chemical degree of freedom. We verified the scheme by comparing numerically obtains results to analytic benchmark solutions. We showed that both a simple diffusion problem as well as a semi-coupled chemo-mechanical process can be simulated correctly. Finally, we studied a classic example in the hydrogen embrittlement community and showed that our scheme reproduces results presented in previous works.

Chapter 4

Hydrogen diffusion in thin film, phase-separating metals[1]

4.1 Introduction to thin film metal hydrogen systems[2]

In this chapter some basics for phase-separating thin film metal hydrogen systems, which form the basis of the developed model, are summarized. We focus on the Nb-H system but want to point out, that many of the results are applicable to both the Pd-H system and the Nb-H system. We summarize experimental results on both bulk and thin film Nb-H systems, which have been previously published in Schober and Wenzl (1978), Nörthemann and Pundt (2008), Nörthemann and Pundt (2011), Hamm et al. (2015), Burlaka et al. (2015), Burlaka et al. (2016) and Wagner et al. (2019). In Nörthemann and Pundt (2008), Nörthemann

---

[1] Chapter 4 is based on the publications "Phase transformation in the palladium hydrogen system: Effects of boundary conditions on phase stabilities" (Dyck et al. (2024b)), "Phase transformation in the Niobium Hydrogen system: Effects of elasto-plastic deformations on phase stability predicted by a thermodynamic model" (Dyck et al. (2024a)) and "Hydride formation in open thin film metal hydrogen systems: Cahn-Hilliard-type phase-field simulations coupled to elasto-plastic deformations" (Dyck et al. (2025)). Further details are given for each section.

[2] Section 4.1 is based on section 2 of the publication "Hydride formation in open thin film metal hydrogen systems: Cahn-Hilliard-type phase-field simulations coupled to elasto-plastic deformations" (Dyck et al., 2025).

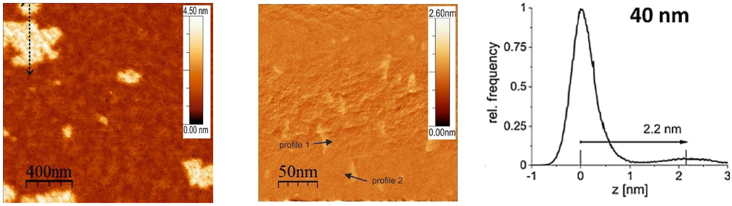

(a) **(b)** **(c)**

Figure 4.1: a) STM surface topography image of a 40 nm epitaxial Nb thin film adhered to sapphire substrate upon hydrogen loading at $p_{\mathrm{H2}} = 1 \times 10^{-6}$ mbar and 293 K, showing cylindrical hydride precipitates surrounded by α-phase. Reproduced with permission from Wagner et al. (2019). b) STM surface topography difference image of an 8 nm Nb film after cyclic hydrogen loading at $p_{\mathrm{H2}} = 8 \times 10^{-6}$ mbar at 293 K, showing no evidence of phase separation. Reproduced with permission from Wagner et al. (2019). c) Relative height distributions in a 40 nm film loaded under the same conditions as in a). Large differences in the out-of-plane expansion of α- and hydride-phase are visible. Reproduced with permission from Nörthemann and Pundt (2008). Figure based on Figure 1 d) e) and f) from Dyck et al. (2025).

and Pundt (2011), Hamm et al. (2015), Burlaka et al. (2015), Burlaka et al. (2016) and Wagner et al. (2019), thin Nb films were produced by means of argon-ion beam sputtering on sapphire substrates, such that epitaxial Nb films with desired thickness and $[110]$-orientation grow on the substrates. To avoid oxidation and to facilitate hydrogen loading, the films were covered with a Pd capping layer or, if the vacuum was not broken between film preparation and hydrogen loading, with Pd islands. Hydrogen loading occurred mainly from the gaseous phase at a given temperature and increasing but stepwise constant gas pressures p_{H2}. This implies, that we will focus on open systems in the following, i.e. systems with the possibility to take up hydrogen from their surrounding at a given chemical potential. To measure the films stress state and the chemical potential as a function of hydrogen concentration, hydrogen loading was performed electrochemically with defined stepwise increase of the hydrogen concentration. The latter system is therefore a closed system. We here assume that the stresses measured as a function of concentration for closed systems can be transferred to the open system (Wagner et al., 2019).

By means of in-situ XRD, STM, TEM, substrate curvature and EMF measurements, the thermodynamics (EMF) as well as in-plane stress states (substrate curvature), height changes (STM) and changes in crystal structure (XRD, TEM) were studied, both for open and closed systems. In open systems, upon hydrogen adsorption these experiments reveal hydride formation and coexistence of a hydrogen poor α-phase and a hydrogen rich hydride-phase at certain hydrogen pressures. In bulk Nb-H both an α'- and β-hydride-phase have been reported, with equilibrium concentrations of $c_\alpha^{\max} = 0.06\,\mathrm{H/Nb}$ and $c_\beta^{\min} = 0.72\,\mathrm{H/Nb}$ (Schober and Wenzl, 1978). In thin Nb-H films these equilibrium concentrations change due to occurring stresses resulting from constraint conditions, c.f. Wagner et al. (2019), and measurements hint on the hydride phase to keep the bcc structure of the matrix phase, c.f. Burlaka et al. (2017). We therefore, in this work, consider an α'-hydride phase to simplify the model. The constraint conditions of thin films, imposed by their adherence to a substrate being much stiffer than the films, introduce large compressive stresses. These stresses strongly alter the onset conditions of phase separation behavior and lead to drastic changes in equilibrium concentrations or even to suppression of phase transition in the case of very thin Nb-H films deforming purely elastic.

During coexistence of α- and hydride-phase, the large difference in hydrogen concentration between both phases leads to marked differences in height, which can be measured by STM, c.f. Fig. 4.1 a) and b) (Nörthemann and Pundt, 2008; Nörthemann and Pundt, 2011). The hydride-phase expands significantly stronger than the α-phase due to the larger number of interstitial hydrogen atoms. Due to the in-plane constraint, this expansion manifests itself in an increased local height and it leads to coherency stresses at the phase interfaces, superimposed by substrate-induced stresses. These stresses affect the progression of the phase transition.

The larger the concentration gradient at the interfaces, the bigger the measured height difference between the local hydride and the surrounding α-phase. As can be seen in Fig. 4.1 a), in a $40\,\mathrm{nm}$ film, the presence of cylindrical hydrides of different radii in the film is confirmed by means of this height change, c.f. also Nörthemann and Pundt (2008). Only upon further hydrogen absorption due to increased gas pressures, the precipitates can loose their cylindrical shape and become more irregular. This is accompanied by misfit dislocation formation at the phase interfaces. Thus, the interfaces can become semicoherent at later stages of hydride formation. However, the phase interfaces remain coherent for films below $39(2)\,\mathrm{nm}$ thickness (Wagner et al., 2019). In films thinner than $8(2)\,\mathrm{nm}$ the phase separation is found to be suppressed (Wagner et al., 2019). This could be attributed to the large substrate-induced compressive stresses. This becomes evident, when the corresponding STM measurements are studied, where no hydride-related height distribution is observed. This is evidence for a continuous transition of the α-phase into a state with a large hydrogen concentration, c.f Fig. 4.1 b). Also in this state dislocation formation can happen, resulting in misfit dislocations at the film-substrate interface. Traces of such dislocations are detected by STM as surface glide steps, see the yellowish lines in 4.1 b).

The height difference between α- and hydride-phase in a $40\,\mathrm{nm}$ film becomes more evident, when the relative frequency of measured heights is studied, c.f. Fig. 4.1 c). We point out, that the average height change of the α-phase has been set to zero in the figure. This reveals, that on average the circular hydride precipitates that form within the α-phase expand $2.2\,\mathrm{nm}$ more in normal direction in the $40\,\mathrm{nm}$ film. This has been studied using Finite Element calculations and linked to cylindrical precipitates extending all the way from the free surface of the thin film down to the substrate interface, with an average radius of $20-40\,\mathrm{nm}$ (Nörthemann and Pundt, 2008).

The coherency of Nb film-substrate and α- and hydride-phase interfaces has been studied in detail by means of the STM measurements in Nörthemann and Pundt (2011). It has been shown, that above a critical film thickness of $5(2)\,\mathrm{nm}$ dislocations form at the interface between film and substrate early upon hydrogen absorption, c.f. Nörthemann and Pundt (2011) and Wagner et al. (2019). This strongly affects the resulting stress states, as misfit dislocations reduce the transmitted stresses (Rahm et al., 2022). Coherency loss at the substrate interface thus leads to reduced in-plane stresses of the films. In contrast, as indicated above the interface between the α- and the hydride-phase has been shown to stay coherent for Nb films below $39(2)\,\mathrm{nm}$ thickness, even for large hydrogen pressures and large hydride precipitates (Nörthemann and Pundt, 2011; Wagner et al., 2019). The loss of cylindrical shape of the hydride precipitates is linked to coherency loss at the phase interfaces, which was only observed for larger film heights and long exposure to gaseous hydrogen.

4.2 Theory of hydride formation in thin film metal hydrogen systems[3]

4.2.1 Basic assumptions

In order to replicate the experimentally observed hydride formation behavior in thin film open metal hydrogen systems we propose a thermodynamically consistent, chemo-mechanically coupled phase-field model. Our model is based on EMF and stress measurements on both the thin film Pd-H and the Nb-H system. This allows us to identify both the chemical part as well as the mechanical part of the systems

---

[3] Section 4.2 is based on section 3 of the publication "Hydride formation in open thin film metal hydrogen systems: Cahn-Hilliard-type phase-field simulations coupled to elasto-plastic deformations" (Dyck et al., 2025).

thermodynamic potential. The model is related to previously published phase-field models in the context of phase separating metals, see, e.g., Anand (2012), Di Leo et al. (2014), Spatschek et al. (2016), Castelli et al. (2021), Han et al. (2019), Heo et al. (2019), Simon et al. (2021) and references therein. In order to arrive at a compact theory, we introduce several basic assumptions from the outset. These are discussed at the end of this section. The basic assumptions are:

- The governing equations are the mass balance of diffusing hydrogen and the balance of linear momentum. Hydrogen is assumed to occupy interstitial lattice sites in both α- and α'-phase. The hydrogen content is not conserved, as an open system exposed to gaseous hydrogen is considered, which is inspired by Di Leo and Anand (2013). Inertia effects are neglected.
- The formation of hydrogen poor α- and hydrogen rich α'- or hydride-phase is described by means of a phase-field model, relying on the concentration as a physical order parameter (Steinbach, 2009). No structural order parameter as in Guo et al. (2008), Han et al. (2019), Heo et al. (2019) and Simon et al. (2021) is introduced.
- A normalized concentration $c_\mathrm{H} = c/c_\mathrm{max}$ of hydrogen atoms per niobium atom $\mathrm{H/Nb}$ is introduced, where c_max is the maximum number of moles of hydrogen per molar volume of the host metal.
- Deformations are assumed to be small, i.e. below $10\,\%$ total deformation, and the total strain $\boldsymbol{\varepsilon}$ is additively decomposed into an elastic part $\boldsymbol{\varepsilon}_\mathrm{e}$, a chemical part $\boldsymbol{\varepsilon}_\mathrm{c}$ and a plastic part $\boldsymbol{\varepsilon}_\mathrm{p}$.
- The free energy density ψ is used as thermodynamic potential, depending on strains, hydrogen concentration, temperature and plastic variables. To introduce the phase-field, both a double well potential ψ_c, introducing the system's tendency to form α- and hydride-phase and an interfacial term ψ_i, modeling the tendency of the system to minimize the interface between different phases, are considered. This

was first proposed by Cahn and Hilliard (1958) and is used in all works cited above.

- The interface between the α- and the hydride-phase is treated as coherent at all times, in agreement with the experimental observations for films. Thus the lattice mismatch between α- and hydride-phase is proportional to the concentration difference between both phases. In addition, the interface between thin film and substrate is treated as staying coherent by keeping the lateral dimensions of the simulation domain constant, yielding in-plane stresses linearly increasing with hydrogen concentration. However, the experimentally informed in-plane stress state of the simulated films may be divided into two regimes with different linear stress increase as a function of hydrogen concentration, mimicking the elasto-plastic deformation of the film-substrate interface (Dyck et al., 2024a).
- The barrier for forming hydride precipitates is the coherency strain barrier introduced in Schwarz and Khachaturyan (1995) and Schwarz and Khachaturyan (2006). No further energetic barrier for precipitate formation is assumed. This implies, that as soon as the concentration limiting the stability region of the α-phase is surpassed, hydride precipitates form within the α-phase (Schwarz et al., 2020). The critical concentration c_α^{sp} is defined by the local maximum of the chemical potential. This is equal to the spinodal concentration in spinodally decomposing systems, and hence we use the same index sp to denote the critical concentration of the α-phase as c_α^{sp}.
- Changes in temperature, e.g. due to plastic deformations, are neglected (Dyck et al., 2024a).
- The Coleman-Noll procedure is used to derive thermodynamic restrictions of the constitutive equations and resulting potential relations and a dissipation inequality. To not further increase the length of this chapter, the derivation is not presented in detail. It can be found for

similar models in, e.g, Gurtin et al. (2010), Anand (2012), Di Leo and Anand (2013) and Dyck et al. (2024c).

- All constitutive functions are modeled isotropic, including stiffness, hydrogen mobility and plasticity (Dyck et al., 2024a). All material parameters are assumed independent of hydrogen concentration. This implies, that changes in elastic parameters, predicted by Cahn and Larché for open systems (Larché and Cahn, 1973; 1978) and recently experimentally verified by Shi et al. (2018), are not considered. An application of the Cahn-Larché theory in the context of a phase-field model can be found in, e.g., Schwarze et al. (2017).

4.2.2 Constitutive theory

A thermodynamically consistent constitutive theory is presented in the following by introducing a free energy density ψ. To this end, a set of independent variables $\Lambda = [\boldsymbol{\varepsilon}, \theta, c_{\mathrm{H}}, \underline{\alpha}]$ is used, where θ is the temperature and $\underline{\alpha}$ is a tuple of internal variables, later considered to be plastic strains $\boldsymbol{\varepsilon}_{\mathrm{p}}$ and the equivalent plastic strain $\varepsilon_{\mathrm{eq}}$. As proposed in previous works in the context of phase-separating, elasto-plastically deforming materials, see, e.g., Anand (2012), Di Leo et al. (2014) and Castelli et al. (2021), we introduce an additive split of the free energy density into an elastic part ψ_{e}, a chemical part ψ_{c} and an interfacial part ψ_{i} via

$$\psi(\Lambda) = \psi_{\mathrm{e}}(\boldsymbol{\varepsilon}_{\mathrm{e}}) + \psi_{\mathrm{c}}(c_{\mathrm{H}}, \theta) + \psi_{\mathrm{i}}(\operatorname{grad}(c_{\mathrm{H}})). \tag{4.1}$$

The elastic part depends on the elastic strains

$$\boldsymbol{\varepsilon}_{\mathrm{e}} = \boldsymbol{\varepsilon} - \boldsymbol{\varepsilon}_{\mathrm{c}} - \boldsymbol{\varepsilon}_{\mathrm{p}}, \tag{4.2}$$

where the volumetric chemical strains are given as

$$\boldsymbol{\varepsilon}_{\mathrm{c}} = \eta_{\mathrm{H}} c_{\mathrm{H}} \boldsymbol{I} \tag{4.3}$$

and η_H is an expansion coefficient describing the dilatation of the metal lattice due to the presence of hydrogen atoms (Wagner et al., 2019). The concentration c_H is expressed in number of hydrogen atoms per number of metal atoms, c.f. Sec. 2.3.2. The elastic part ψ_e is quadratic in the elastic strains

$$\psi_\mathrm{e} = \frac{1}{2}\boldsymbol{\varepsilon}_\mathrm{e} \cdot \mathbb{C}\left[\boldsymbol{\varepsilon}_\mathrm{e}\right], \tag{4.4}$$

where $\mathbb{C}$ is the stiffness tensor. The chemical part ψ_c is given by (Dyck et al., 2024b;a)

$$\begin{aligned}\psi_\mathrm{c} = \mu_0\, c_\mathrm{H}\, c_\mathrm{max} + R\theta c_\mathrm{max}\left(-r\ln\left(\frac{r}{r - c_\mathrm{H}}\right) + c_\mathrm{H}\ln\left(\frac{c_\mathrm{H}}{r - c_\mathrm{H}}\right)\right)\\ - \frac{c_\mathrm{max}}{2}E_\mathrm{HH}c_\mathrm{H}^2.\end{aligned} \tag{4.5}$$

Here μ_0 is a reference chemical potential, R is the gas constant and E_HH is a long-range attractive hydrogen-hydrogen interaction energy. It results from the interaction of dissolved hydrogen atoms via the H-induced dilatation field of the metal lattice. Hence, E_HH defines the driving force for the initiation of the phase transition in the metal hydrogen system (Wagner and Pundt, 2016), as it introduces a second well in ψ_c, indicating the system's tendency to form two phases. The parameter r is introduced to consider electronic interactions and related second nearest neighbor blocking of H atoms on tetrahedral interstitial sites (Switendick, 1979; Wicke et al., 1978; Fukai, 2005), limiting the maximum concentration of hydrogen atoms within the lattice. The parameter r can be identified by means of EMF measurements (Wagner et al., 2019). This implies, that our form of ψ_c considers both the electronic interaction of hydrogen atoms with Nb (by means of r) and the maximum number of interstitial sites available (by means of c_max). As the electronic interaction dominates at large concentrations, which is the case for the considered Pd-H and Nb-H systems, the parameter r determines the maximum hydrogen concentration (Dyck et al., 2024b;a).

Before proceeding we want to briefly comment on the specific form of ψ_{c}, which differs from oftentimes used approaches Anand (2012); Di Leo et al. (2014); Han et al. (2019); Heo et al. (2019); Simon et al. (2021). The logarithmic part is, also in our approach, based on the classic mixture entropy model for ideal gases. However, in the thin films considered in this work, not all geometrically available interstitial sites can be occupied by hydrogen atoms, due to electronic interactions between them. This implies, that the hydrogen concentration is capped at a value $c_{\mathrm{H}} < 1$. In our model, this is accounted for by the introduction of the parameter r, which implies mathematically $0 \leq c_{\mathrm{H}} \leq r$. The classic expression for entropy of mixing is retrieved from our formulation by setting $r = 1$. In addition, commonly, the double well form of ψ_{c} is introduced by considering a mixture enthalpy model, see, e.g., Gurtin et al. (2010), Anand (2012) and Spatschek et al. (2016), that introduces the system's tendency to form a second phase. In our approach E_{HH} is introduced to that end, allowing us to incorporate the mentioned EMF and stress measurements by fitting E_{HH}, and hence to couple the theory to the experiment.

The final contribution to the free energy density is the interfacial part ψ_{i}, which describes the system's tendency to minimize the interface between the two phases. It is given by (Cahn and Hilliard, 1958; Anand, 2012)

$$\psi_{\mathrm{i}} = \frac{1}{2} R\theta c_{\mathrm{max}} \lambda_{\mathrm{c}} \|\mathrm{grad}\,(c_{\mathrm{H}})\|^2. \tag{4.6}$$

The parameter λ_{c} describes the width of the interface separating α- and α'-phase and $\|\mathrm{grad}\,(c_{\mathrm{H}})\|$ denotes the Frobenius norm of the concentration gradient. The chemical potential of hydrogen and the Cauchy stresses follow from potential relations via (Anand, 2012; Di Leo et al., 2014)

$$\begin{aligned}
\mu &= \frac{\partial \psi}{\partial c_{\mathrm{H}}} \frac{1}{c_{\max}} = \frac{1}{c_{\max}} \frac{\partial \psi_{\mathrm{c}}}{\partial c_{\mathrm{H}}} - \eta_{\mathrm{H}} \nu_0 \mathrm{tr}\left(\boldsymbol{\sigma}\right) - \frac{1}{c_{\max}} \mathrm{div}\left(\frac{\partial \psi_{\mathrm{i}}}{\partial \mathrm{grad}\left(c_{\mathrm{H}}\right)}\right) \\
&= \mu_0 + R\theta \ln\left(\frac{c_{\mathrm{H}}}{r - c_{\mathrm{H}}}\right) - E_{\mathrm{HH}} c_{\mathrm{H}} - \eta_{\mathrm{H}} \nu_0 \mathrm{tr}\left(\boldsymbol{\sigma}\right) - R\theta \lambda_{\mathrm{c}} \Delta c_{\mathrm{H}}, \\
\boldsymbol{\sigma} &= \frac{\partial \psi}{\partial \boldsymbol{\varepsilon}} = \mathbb{C}\left[\boldsymbol{\varepsilon}_{\mathrm{e}}\right],
\end{aligned} \tag{4.7}$$

where $\nu_0 = 1/c_{\max}$. The Laplace operator applied to the concentration is Δc_{H}. The potential relations are assumed to hold for both elastic and elasto-plastic deformations. Having specified all equilibrium contributions, the dissipative parts, i.e. plasticity and hydrogen flux $\boldsymbol{j}$ have to be introduced. The plasticity model is a rate-independent, isotropic von Mises theory (Mises, 1928). The yield function, limiting the range of purely elastic deformations, is

$$\varphi(\boldsymbol{\sigma}', \varepsilon_{\mathrm{eq}}) = ||\boldsymbol{\sigma}'|| - \sqrt{\frac{2}{3}} \sigma_{\mathrm{F}}\left(\varepsilon_{\mathrm{eq}}\right) \leq 0, \tag{4.8}$$

where $\sigma_{\mathrm{F}}\left(\varepsilon_{\mathrm{eq}}\right) = \sigma_{\mathrm{F0}} + h\varepsilon_{\mathrm{eq}}$ denotes the yield stress with initial yield stress σ_{F0} and hardening modulus h. The deviatoric part of the stress is $\boldsymbol{\sigma}'$. This captures the measured in-plane stresses as detailed in Dyck et al. (2024a). In an associated plastic flow theory, both internal variables evolve according to

$$\dot{\boldsymbol{\varepsilon}}_{\mathrm{p}} = \sqrt{\frac{3}{2}} \gamma \boldsymbol{N}, \quad \dot{\varepsilon}_{\mathrm{eq}} = \sqrt{\frac{2}{3}} \gamma, \tag{4.9}$$

where $\boldsymbol{N} = \boldsymbol{\sigma}'/\|\boldsymbol{\sigma}'\|$ and γ is the consistency parameter. The consistency parameter is only non-zero, when the yield condition $\varphi = 0$ and the loading condition $\boldsymbol{\sigma} \cdot \dot{\varepsilon} > 0$ are fulfilled.

The hydrogen flux is given as (Anand, 2012)

$$\boldsymbol{j} = -m(c_{\mathrm{H}}) \,\mathrm{grad}\left(\mu\right), \tag{4.10}$$

where $m(c_\mathrm{H})$ is the mobility of hydrogen in Nb. It is a function of hydrogen concentration and diffusion constant D via (Anand, 2012)

$$m(c_\mathrm{H}) = \frac{D c_\mathrm{max}}{R\theta} c_\mathrm{H}(1 - c_\mathrm{H}). \tag{4.11}$$

4.2.3 Closed set of governing equations

Inserting the hydrogen flux (Eq. (4.10)) and the potential relations (Eqs. (4.7)) into the balance of mass and linear momentum (c.f. Eq. (2.21)) yields a set of coupled PDEs, that describe diffusing hydrogen and the formation of hydrides and elasto-plastic deformations in thin film metals. The diffusion equation is, due to the interfacial contribution to the free energy density, a fourth-order PDE. The solution of this coupled system is detailed in the following section. The coupled system of PDE is

$$\begin{aligned} \mathrm{div}\,(\boldsymbol{\sigma}) &= \mathbf{0}, \\ c_\mathrm{max}\, \dot{c}_\mathrm{H} &= \mathrm{div}\left(\frac{D c_\mathrm{max} c_\mathrm{H}\,(1 - c_\mathrm{H})}{R\theta} \mathrm{grad}\,(\mu)\right). \end{aligned} \tag{4.12}$$

Both boundary conditions (expressed via $\bar{(\cdot)}$) and initial conditions (expressed via $(\cdot)_0$) have to be specified for the degrees of freedom c_H and $\boldsymbol{u}$ in order to obtain a solution. Commonly, a Cahn-Hilliard equation is considered for mass conserving systems, i.e. the amount of hydrogen remains constant, c.f. Voskuilen and Pourpoint (2013) and Bair et al. (2017). However, in our work, the metal is exposed to gaseous hydrogen and diffusion into and out of the thin film can occur. This exposure is best mimicked by a boundary condition for the chemical potential of hydrogen, i.e.

$$\bar{\mu} = \bar{\mu}(p_\mathrm{H2}) = \frac{1}{2}\mu_\mathrm{H2}(p_\mathrm{H2}) = \frac{1}{2}\left(\mu^0_\mathrm{H2} + R\theta \ln\left(\frac{p_\mathrm{H2}}{p_0}\right)\right), \tag{4.13}$$

where p_{H2} is the partial pressure of gaseous hydrogen, p_0 a reference pressure and μ^0_{H2} the reference chemical potential of hydrogen molecules, discussed in greater detail in Di Leo and Anand (2013). This will be used in the following, when hydride formation in open is investigated by means of numerical simulations and analytical considerations.

4.2.4 Discussion of the model equations and assumptions

Before proceeding with details on the implementation of our model, the following remarks are in order:

- Defects of the lattice structure in a metal, e.g. grain boundaries or dislocations, can serve as potential traps for hydrogen atoms, see, e.g. Sofronis and McMeeking (1989) and Di Leo and Anand (2013). These are not accounted for in our model, due to the low number of initial lattice defects in epitaxial Nb thin films (Wagner et al., 2019). In addition, hydrogen-induced vacancy formation is not considered (Čížek et al., 2004).
- The difference between occurring stresses in 5 and $40\,\mathrm{nm}$ Nb films is a size effect, which results from the balance of the total elastic energy stored in a thin film and the formation energy of dislocations Wagner and Pundt (2016). This is not captured by our model, which is a first gradient theory, in contrast to, e.g., Forest et al. (2000). Instead we use a size dependent increased initial yield stress σ_{F0} in order to study purely elastic behavior.
- In the Zr-H system, commonly both a Cahn-Hilliard as well as an Allen-Cahn equation are solved, see, e.g. Voskuilen and Pourpoint (2013), Han et al. (2019), Heo et al. (2019) and Simon et al. (2021). The latter describes the evolution of structural order parameters, capturing changes in crystallographic structure or different hydride variants. As we only consider a single hydride-phase with constant material

parameters, we refrain from incorporating an Allen-Cahn equation, in order to reduce the complexity of the model.

- As stated, the interface between thin film and substrate can become semicoherent upon hydrogen absorption by the formation of misfit dislocations. We indirectly incorporate this effect via the measured in-plane stress of the films. This is done via the hardening modulus h as well as the yield stress σ_{F0}, identified in Dyck et al. (2024a), resembling the experimentally observed stress release due to the coherency loss at the film-substrate interface. Still, coherency strains will occur at the substrate interface in our simulations, leading to the build up of additional in-plane stresses Rahm et al. (2022) of a magnitude not observed in the experiments. This difference results from inhomogeneous stress relaxation occurring at the interfaces of α-phase and substrate or hydride precipitates and substrate in the experiment.
- Open systems show strongly differing hydride formation patterns compared to closed systems, as has been recently pointed out for the Pd-H system in Schwarz et al. (2020), Rahm et al. (2022) and Weissmüller (2024). We only consider open systems in our work by prescribing a chemical potential μ for hydrogen in lattice sites at the upper boundary of the simulation domain. In this setup the α-phase transforms into the α'- or hydride-phase as soon as the unstable region of the phase diagram presented in Dyck et al. (2024a) is reached. Both phases are considered to have the same lattice structure and are therefore represented by one free energy density possessing two local minima and one local maximum.
- For Nb we propose to use an isotropic elastic and an isotropic, phenomenological plastic model. Both are simplifying assumptions for the considered thin film systems, as these grow epitaxially with a $[110]$ orientation (Wagner et al., 2019).

4.3 Numerical implementation of the theory[4]

4.3.1 General approach

In the context of chemo-mechanical coupling and phase separation, PDEs of order four and their numerical solution on a domain Ω using Finite Element methods have been studied before, see, e.g., Steinbach (2009), Ammar et al. (2009), Di Leo et al. (2014), Castelli et al. (2021) and many others. However, solving a PDE with derivatives of order > 2 leads to difficulties, that only a limited number of element formulations fulfill, see, e.g., Wodo and Ganapathysubramanian (2011) and Zhang et al. (2013). Instead of proceeding on using non-standard Finite Element techniques, a mixed formulation can be used, which introduces an additional degree of freedom in order to split the fourth-order PDE into two second-order PDEs, doubling the number of solution variables. For examples we refer to, e.g., Ubachs et al. (2004), Di Leo et al. (2014), Forest et al. (2011), Chen et al. (2014) and Castelli et al. (2021).

However, different strategies were used. In Ubachs et al. (2004) and Di Leo et al. (2014) a micromorphic approach is used, that introduces an artificial concentration and penalizes deviations from the actual concentration. In contrast, in Chen et al. (2014) and Castelli et al. (2021) both the concentration and the chemical potential are used as numerical degrees of freedom. For the latter approach both existence and uniqueness of Finite Element solutions have been studied, see, e.g. Elliott et al. (1989), Copetti and Elliott (1992) and Barrett and Blowey (1999).

For this reason we choose a mixed formulation introducing a second chemical degree of freedom, namely the chemical potential, to numeri-

---

[4] Section 3 is based on section 4 of the publication "Hydride formation in open thin film metal hydrogen systems: Cahn-Hilliard-type phase-field simulations coupled to elasto-plastic deformations" (Dyck et al., 2025).

cally solve the system of coupled PDEs outlined in the previous section. We rely on the commercial Finite Element solver ABAQUS and its User Defined Element (UEL) subroutine. This allows us to use the automatic time-stepping scheme as well as the graphical user interface of ABAQUS, while offering the flexibility to define individual PDEs. To this end, each balance equation is discretized using Finite Elements and the element residuals as well as their tangents are supplied to ABAQUS. A thorough explanation of each step necessary to write a UEL has been discussed by Chester et al. (2015). Here, we will not go into detail. Instead, we briefly present the discretization including the weak form of the PDEs.

4.3.2 Mixed formulation

In order to reduce the highest derivative in the diffusion equation to two, the total hydrogen concentration c_H as well as the chemical potential μ are used as the chemical degrees of freedom in our implementation. This implies, that the diffusion equation (4.12) (2) is replaced by two coupled PDEs, namely

$$\begin{aligned} c_\mathrm{max}\dot{c}_\mathrm{H} &= \mathrm{div}\left(\frac{Dc_\mathrm{max}c_\mathrm{H}(1-c_\mathrm{H})}{R\theta}\mathrm{grad}\left(\mu\right)\right), \\ \mu &= \frac{1}{c_\mathrm{max}}\frac{\partial\psi_\mathrm{c}}{\partial c_\mathrm{H}} - \eta_\mathrm{H}\nu_0\mathrm{tr}\left(\boldsymbol{\sigma}(\boldsymbol{\varepsilon}, c_\mathrm{H}, \boldsymbol{\varepsilon}_\mathrm{p})\right) - R\theta\lambda_\mathrm{c}\Delta c_\mathrm{H}. \end{aligned} \tag{4.14}$$

In both PDEs, the highest derivative is two. The strong form of balance equations, being solved using a Finite Element scheme is thus (c.f. Eqs. (4.12))

$$\begin{aligned} c_\mathrm{max}\dot{c}_\mathrm{H} &= \mathrm{div}\left(\frac{Dc_\mathrm{max}c_\mathrm{H}(1-c_\mathrm{H})}{R\theta}\mathrm{grad}\left(\mu\right)\right), \\ \mu &= \frac{1}{c_\mathrm{max}}\frac{\partial\psi_\mathrm{c}}{\partial c_\mathrm{H}} - \eta_\mathrm{H}\nu_0\mathrm{tr}\left(\boldsymbol{\sigma}(\boldsymbol{\varepsilon}, c_\mathrm{H}, \boldsymbol{\varepsilon}_\mathrm{p})\right) - R\theta\lambda_\mathrm{c}\Delta c_\mathrm{H}, \\ \mathbf{0} &= \mathrm{div}\left(\boldsymbol{\sigma}(\boldsymbol{\varepsilon}, c_\mathrm{H}, \boldsymbol{\varepsilon}_\mathrm{p})\right). \end{aligned} \tag{4.15}$$

The numerical degrees of freedom are the concentration c_{H}, the chemical potential μ as well as the displacement $\boldsymbol{u}$, while the plastic strains $\boldsymbol{\varepsilon}_{\mathrm{p}}$ and the equivalent plastic strain $\varepsilon_{\mathrm{pe}}$ are treated as internal variables, using a radial return method and an implicit Euler scheme for time integration (Simo and Hughes, 1998). We note, that using this splitting method, an open system can be studied by prescribing a boundary value for μ. All balance equations are non-dimensionalized (Castelli et al., 2021). To this end, Eq. (4.15) (1) is divided by $c_{\max}$, Eq. (4.15) (2) by $R\theta$ and Eq. (4.15) (3) by Young's modulus E. The dimensionless chemical potential is, in the following, denoted by $\hat{\mu}$.

4.3.3 Finite Element discretization

The non-dimensionalized strong form is converted to a weak form by multiplying each PDE with a test function, integration over the computational domain Ω and an integration by parts. The test functions for each degree of freedom are w_c, w_μ and $\boldsymbol{w}_u$. The resulting weak forms are

$$\begin{aligned}
0 &= -\int_\Omega \left(w_{\mathrm{c}}\dot{c}_{\mathrm{H}}\right)\mathrm{d}V - \int_\Omega \left(\frac{Dc_{\mathrm{H}}(1-c_{\mathrm{H}})}{R\theta}\operatorname{grad}(w_{\mathrm{c}})\cdot\operatorname{grad}(\hat{\mu})\right)\mathrm{d}V,\\
0 &= -\int_\Omega \left(w_\mu\left(\frac{1}{R\theta c_{\max}}\frac{\partial\psi_{\mathrm{c}}}{\partial c_{\mathrm{H}}}-\hat{\mu}\right)\right)\mathrm{d}V + \int_\Omega \left(\frac{\nu_0\eta_{\mathrm{H}}}{R\theta}w_\mu\operatorname{tr}(\boldsymbol{\sigma})\right)\mathrm{d}V\\
&\quad - \int_\Omega \left(\lambda_{\mathrm{c}}\operatorname{grad}(w_\mu)\cdot\operatorname{grad}(c_{\mathrm{H}})\right)\mathrm{d}V, \qquad (4.16)\\
\mathbf{0} &= -\int_\Omega \left(\operatorname{grad}(\boldsymbol{w}_u)\cdot\frac{\boldsymbol{\sigma}}{E}\right)\mathrm{d}V.
\end{aligned}$$

We use static condensation to express $\boldsymbol{\sigma}$ as a function of the nodal degrees of freedom, i.e, $\boldsymbol{u}$ and c_{H}. The tuple of internal variables $\underline{\alpha}$ is stored at each integration point (Simo and Hughes, 1998).

The loading and consistency condition are replaced by the Karush-Kuhn-Tucker conditions (Simo and Hughes, 1998)

$$\gamma \geq 0, \quad \varphi \leq 0, \quad \gamma\varphi = 0. \tag{4.17}$$

The simulation time is discretized in time steps, where $t^{n+1} = t^n + \Delta t^n$ and the automatic time stepping algorithm of ABAQUS is used to specify the non-constant Δt. The time derivative in the diffusion equation is approximated by means of an implicit Euler scheme (or backward differentiation formula of first order (Gear, 1967))

$$\dot{c}_{\mathrm{H}}^{n+1} = \frac{c_{\mathrm{H}}^{n+1} - c_{\mathrm{H}}^{n}}{\Delta t}. \tag{4.18}$$

Quantities from the previous converged increment are denoted by $(\cdot)^n$ in the following, while quantities from the current increment will not be marked to shorten notation. The computational domain Ω is discretized using fully integrated isoparameteric, hexahedral Finite Elements and linear shape functions for the continuous degrees of freedom. The solution variables as well as the test functions for all nodes in each element are collected in the vectors $\underline{c}_{\mathrm{E}}, \underline{w}_{\mathrm{E},c}, \underline{\hat{\mu}}_{\mathrm{E}}, \underline{w}_{\mathrm{E},\mu}, \underline{u}_{\mathrm{E}}$ and $\underline{w}_{\mathrm{E},u}$. A Galerkin ansatz is chosen, i.e. for each test function the same ansatz functions are used as for the nodal degrees of freedom. The linear ansatz functions are collected in matrices $\underline{N}_{\mathrm{c}}, \underline{N}_{\mu}$ and $\underline{\underline{N}}_{u}$. This results in

$$\begin{aligned}
c_{\mathrm{H}}^{\mathrm{h}}(\boldsymbol{x},t) &= \underline{N}_c^{\mathsf{T}}(\boldsymbol{x})\ \underline{c}_{\mathrm{E}}(t), & w_{\mathrm{c}}^{\mathrm{h}}(\boldsymbol{x},t) &= \underline{N}_c^{\mathsf{T}}(\boldsymbol{x})\ \underline{w}_{\mathrm{E},c}(t),\\
\hat{\mu}^{\mathrm{h}}(\boldsymbol{x},t) &= \underline{N}_\mu^{\mathsf{T}}(\boldsymbol{x})\ \underline{\hat{\mu}}_{\mathrm{E}}(t), & w_{\mu}^{\mathrm{h}}(\boldsymbol{x},t) &= \underline{N}_\mu^{\mathsf{T}}(\boldsymbol{x})\underline{w}_{\mathrm{E},\mu}(t),\\
\boldsymbol{u}^{\mathrm{h}}(\boldsymbol{x},t) &= \underline{\underline{N}}_u^{\mathsf{T}}(\boldsymbol{x})\ \underline{u}_{\mathrm{E}}(t), & \boldsymbol{w}_{u}^{\mathrm{h}}(\boldsymbol{x},t) &= \underline{\underline{N}}_u^{\mathsf{T}}(\boldsymbol{x})\underline{w}_{\mathrm{E},u}(t).
\end{aligned} \tag{4.19}$$

Gradients of the degrees of freedom are expressed via $\underline{\underline{B}}$-matrices as in

$$\begin{aligned}
\operatorname{grad}(c_{\mathrm{H}}^{\mathrm{h}}(\boldsymbol{x},t)) &= \underline{\underline{B}}_c^{\mathsf{T}}(\boldsymbol{x})\ \underline{c}_{\mathrm{E}}(t),\\
\operatorname{grad}(w_{\mathrm{c}}^{\mathrm{h}}(\boldsymbol{x},t)) &= \underline{\underline{B}}_c^{\mathsf{T}}(\boldsymbol{x})\ \underline{w}_{\mathrm{E},c}(t),\\
\operatorname{grad}(\hat{\mu}^{\mathrm{h}}(\boldsymbol{x},t)) &= \underline{\underline{B}}_\mu^{\mathsf{T}}(\boldsymbol{x})\ \underline{\hat{\mu}}_{\mathrm{E}}(t),\\
\operatorname{grad}(w_{\mu}^{\mathrm{h}}(\boldsymbol{x},t)) &= \underline{\underline{B}}_\mu^{\mathsf{T}}(\boldsymbol{x})\ \underline{w}_{\mathrm{E},\mu}(t),\\
\operatorname{grad}(\boldsymbol{u}^{\mathrm{h}}(\boldsymbol{x},t)) &= \underline{\underline{B}}_u^{\mathsf{T}}(\boldsymbol{x})\ \underline{u}_{\mathrm{E}}(t),\\
\operatorname{grad}(\boldsymbol{w}_{u}^{\mathrm{h}}(\boldsymbol{x},t)) &= \underline{\underline{B}}_u^{\mathsf{T}}(\boldsymbol{x})\underline{w}_{\mathrm{E},u}(t).
\end{aligned} \tag{4.20}$$

The discretized stresses and strains in each element are denoted as $\underline{\sigma}$ and $\underline{\varepsilon}$ and the trace of the stresses as $\operatorname{tr}(\underline{\sigma}) = \underline{I}^{\mathsf{T}}\underline{\sigma}$, where $\underline{I}$ is the identity tensor in Voigt-Mandel notation. The discretized mobility, its derivative, as well as derivatives of the chemical part of the free energy density are denoted as

$$\begin{aligned}
m &= \frac{D\underline{N}_c^{\mathsf{T}}\underline{c}_{\mathrm{E}}(1-\underline{N}_c^{\mathsf{T}}\underline{c}_{\mathrm{E}})}{R\theta},\\
m_{\mathrm{c}} &= \frac{D(1-2\underline{N}_c^{\mathsf{T}}\underline{c}_{\mathrm{E}})}{R\theta},\\
f_{\mathrm{c}} &= \frac{1}{R\theta c_{\max}}\ \frac{\partial\psi_{\mathrm{c}}}{\partial c_{\mathrm{H}}}\bigg|_{\underline{N}_c^{\mathsf{T}}\underline{c}_{\mathrm{E}}},\\
f_{\mathrm{cc}} &= \frac{1}{R\theta c_{\max}}\ \frac{\partial^2\psi_{\mathrm{c}}}{\partial c_{\mathrm{H}}^2}\bigg|_{\underline{N}_c^{\mathsf{T}}\underline{c}_{\mathrm{E}}}.
\end{aligned} \tag{4.21}$$

Inserting the discretized degrees of freedom into Eq. (4.16) results in the element residuals

$$\begin{aligned}
\underline{R}_{\mathrm{E,c}} &= \int_{\Omega_\mathrm{E}} \left(-\underline{N}_\mu \underline{N}_\mu^\mathsf{T} \underline{\hat{\mu}}_\mathrm{E} + \lambda_\mathrm{c} \underline{\underline{B}}_c \underline{\underline{B}}_c^\mathsf{T} \underline{c}_\mathrm{E} - \frac{\eta_\mathrm{H} \nu_0}{R\theta} \underline{N}_\mu \underline{I}^\mathsf{T} \underline{\sigma} + \underline{N}_\mu f_\mathrm{c} \right) \mathrm{d}V_\mathrm{E}, \\
\underline{R}_{\mathrm{E},\mu} &= \int_{\Omega_\mathrm{E}} \left(\frac{\underline{N}_c \left(\underline{N}_c^\mathsf{T} \underline{c}_\mathrm{E} - \underline{N}_c^\mathsf{T} \underline{c}_\mathrm{E}^n \right)}{\Delta t} + m \underline{\underline{B}}_\mu \underline{\underline{B}}_\mu^\mathsf{T} \underline{\hat{\mu}}_\mathrm{E} \right) \mathrm{d}V_\mathrm{E}, \\
\underline{R}_{\mathrm{E,u}} &= \int_{\Omega_\mathrm{E}} \left(\underline{\underline{B}}_u \frac{\underline{\sigma}}{E} \right) \mathrm{d}V_\mathrm{E},
\end{aligned} \tag{4.22}$$

where we have omitted the test functions, as the residuals have to hold for all test functions. The integrals are computed using gauß quadrature. The element residuals are evaluated for all elements and gathered in the residual vector of the system. To compute the increment $(\cdot)^{n+1}$ for each nodal degree of freedom, ABAQUS uses Newton's method.

To compute the Newton update, the derivatives of the element residuals with respect to the nodal degrees of freedom are required. These are collected in an element tangent matrix denoted as

$$\underline{\underline{K}}_\mathrm{E} = \begin{bmatrix} \underline{\underline{K}}_{\mathrm{E,uu}} & \underline{\underline{K}}_{\mathrm{E,u}\mu} & \underline{\underline{K}}_{\mathrm{E,uc}} \\ \underline{\underline{K}}_{\mathrm{E},\mu\mathrm{u}} & \underline{\underline{K}}_{\mathrm{E},\mu\mu} & \underline{\underline{K}}_{\mathrm{E},\mu\mathrm{c}} \\ \underline{\underline{K}}_{\mathrm{E,cu}} & \underline{\underline{K}}_{\mathrm{E,c}\mu} & \underline{\underline{K}}_{\mathrm{E,cc}} \end{bmatrix}. \tag{4.23}$$

Due to the way ABAQUS handles the Newton update (Smith, 2009; Chester et al., 2015), the residuals are multiplied by -1 before differentiation. The non-vanishing entries are given by

$$\begin{aligned}
\underline{\underline{K}}_{\mathrm{E,uu}} &= \int_{\Omega_{\mathrm{E}}} \left(\underline{\underline{B}}_{u} \frac{\partial \underline{\sigma}}{\partial \underline{\varepsilon}} \underline{\underline{B}}_{u}^{\mathsf{T}} \mathrm{d} \right) V_{\mathrm{E}}, \\
\underline{\underline{K}}_{\mathrm{E,uc}} &= \int_{\Omega_{\mathrm{E}}} \left(\underline{\underline{B}}_{u} \frac{\partial \underline{\sigma}}{\partial c_{\mathrm{H}}} \underline{N}_{c}^{\mathsf{T}} \mathrm{d} \right) V_{\mathrm{E}}, \\
\underline{\underline{K}}_{\mathrm{E},\mu\mathrm{c}} &= \int_{\Omega_{\mathrm{E}}} \left(\frac{1}{\Delta t} \underline{N}_{c} \underline{N}_{c}^{\mathsf{T}} + \underline{\underline{B}}_{\mu} \underline{\underline{B}}_{\mu}^{\mathsf{T}} \underline{\mu}_{\mathrm{E}} m_{\mathrm{c}} \right) \mathrm{d}V_{\mathrm{E}}, \\
\underline{\underline{K}}_{\mathrm{E},\mu\mu} &= \int_{\Omega_{\mathrm{E}}} \left(m \underline{\underline{B}}_{\mu} \underline{\underline{B}}_{\mu}^{\mathsf{T}} \right) \mathrm{d}V_{\mathrm{E}}, \\
\underline{\underline{K}}_{\mathrm{E,cu}} &= \int_{\Omega_{\mathrm{E}}} \left(\frac{-\eta_{\mathrm{H}} \nu_{0}}{R\theta} \underline{N}_{c} \underline{I}^{\mathsf{T}} \frac{\partial \underline{\sigma}}{\partial \underline{\varepsilon}} \underline{\underline{B}}_{u}^{\mathsf{T}} \right) \mathrm{d}V_{\mathrm{E}}, \\
\underline{\underline{K}}_{\mathrm{E,c}\mu} &= \int_{\Omega_{\mathrm{E}}} \left(-\underline{N}_{\mu} \underline{N}_{\mu}^{\mathsf{T}} \right) \mathrm{d}V_{\mathrm{E}}, \\
\underline{\underline{K}}_{\mathrm{E,cc}} &= \int_{\Omega_{\mathrm{E}}} \left(\underline{N}_{c} \underline{N}_{c}^{\mathsf{T}} f_{\mathrm{cc}} + \lambda_{\mathrm{c}} \underline{\underline{B}}_{c} \underline{\underline{B}}_{c}^{\mathsf{T}} - \frac{\eta_{\mathrm{H}} \nu_{0}}{R\theta} \underline{N}_{c} \underline{I}^{\mathsf{T}} \frac{\partial \underline{\sigma}}{\partial c_{\mathrm{H}}} \underline{N}_{c}^{\mathsf{T}} \right) \mathrm{d}V_{\mathrm{E}}.
\end{aligned} \tag{4.24}$$

The algorithmic tangent for an isotropic von Mises elasto-plastic material, i.e. $\partial \underline{\sigma} / \partial \underline{\varepsilon}$, has been summarized and discussed in detail in Simo and Hughes (1998) and is not repeated here. The change in stress due to a variation in hydrogen concentration is $\partial \underline{\sigma} / \partial c_{\mathrm{H}} = -\eta_{\mathrm{H}} \underline{\underline{C}}\, \underline{I}$, where the stiffness matrix in Voigt-Mandel notation is $\underline{\underline{C}}$.

4.4 Analytical results

4.4.1 General approach

In this section we study the proposed thermodynamic model analytically, i.e. without numerical simulations. To this end, we investigate the chemical potential μ resulting from the free energy density presented in Eq. (4.1), neglecting the interfacial contribution ψ_i. This implies, that we can not investigate a two-phase equilibrium of α- and hydride-phase. However, this gives us the possibility to compute both critical concentrations of hydride formation and critical temperatures for the suppression of hydride formation. The additional assumptions are (Dyck et al., 2024b;a):

- both chemical strains $\boldsymbol{\varepsilon}_\mathrm{c}$ and plastic strains $\boldsymbol{\varepsilon}_\mathrm{p}$ are considered to be non-vanishing,
- the concentration and all other fields are assumed to be homogeneous and
- the concentration is assumed to be monotonically increasing, i.e. only hydrogen loading is investigated.

Under these assumptions, the chemical potential and stress tensor are (Dyck et al., 2024b;a)

$$\begin{aligned} \mu &= \frac{\partial \psi}{\partial c_\mathrm{H}} \frac{1}{c_\mathrm{max}} = \mu_0 + R\theta \ln\left(\frac{c_\mathrm{H}}{r - c_\mathrm{H}}\right) - E_\mathrm{HH} c_\mathrm{H} - \eta_\mathrm{H} \nu_0 \mathrm{tr}\left(\boldsymbol{\sigma}\right), \\ \boldsymbol{\sigma} &= \frac{\partial \psi}{\partial \boldsymbol{\varepsilon}} = \mathbb{C}\left[\boldsymbol{\varepsilon} - \boldsymbol{\varepsilon}_\mathrm{c} - \boldsymbol{\varepsilon}_\mathrm{p}\right]. \end{aligned} \tag{4.25}$$

The analytic investigation relies on the fact, that the stress tensor $\boldsymbol{\sigma}$ can be analytically given as a function of hydrogen concentration c_H in constrained metal hydrogen systems, both for purely elastic deformations, c.f. Dyck et al. (2024b), and for elasto-plastic deformations, c.f. Dyck et al. (2024a). The considered constraint conditions are summarized in Fig. 4.2 for a free system (0D constraint) as well as systems with 1D, 2D and 3D constraints. We want to point out, that the 2D constraint depicted in Fig. 4.2 c) is equivalent to the condition of a thin film adhered to a rigid substrate (Dyck et al., 2024a). For the varying constraints the total strain tensors are (in Voigt-Mandel Notation)

$$\boldsymbol{\varepsilon}^{0\mathrm{D}} = \begin{pmatrix} \eta_{\mathrm{H}} c_{\mathrm{H}} \\ \eta_{\mathrm{H}} c_{\mathrm{H}} \\ \eta_{\mathrm{H}} c_{\mathrm{H}} \\ 0 \\ 0 \\ 0 \end{pmatrix}, \; \boldsymbol{\varepsilon}^{1\mathrm{D}} = \begin{pmatrix} 0 \\ \varepsilon_{22}^{1\mathrm{D}} \\ \varepsilon_{33}^{1\mathrm{D}} \\ 0 \\ 0 \\ 0 \end{pmatrix}, \; \boldsymbol{\varepsilon}^{2\mathrm{D}} = \begin{pmatrix} 0 \\ 0 \\ \varepsilon_{33}^{2\mathrm{D}} \\ 0 \\ 0 \\ 0 \end{pmatrix}, \tag{4.26}$$

while $\boldsymbol{\varepsilon}^{3\mathrm{D}} = \mathbf{0}$. For a given concentration c_{H}, the chemical strain is known as $\boldsymbol{\varepsilon}_{\mathrm{c}} = \eta_{\mathrm{H}} c_{\mathrm{H}} \boldsymbol{I}$. The last thing to note is the fact, that in any direction, in which the system can expand freely, the stresses vanish (Dyck et al., 2024b). This implies, that the stress tensors for each constraint condition have the form

$$\boldsymbol{\sigma}^{1\mathrm{D}} = \begin{pmatrix} \sigma_{11}^{1\mathrm{D}} \\ 0 \\ 0 \\ 0 \\ 0 \\ 0 \end{pmatrix}, \; \boldsymbol{\sigma}^{2\mathrm{D}} = \begin{pmatrix} \sigma_{11}^{2\mathrm{D}} \\ \sigma_{22}^{2\mathrm{D}} \\ 0 \\ 0 \\ 0 \\ 0 \end{pmatrix}, \; \boldsymbol{\sigma}^{3\mathrm{D}} = \begin{pmatrix} \sigma_{11}^{3\mathrm{D}} \\ \sigma_{22}^{3\mathrm{D}} \\ \sigma_{33}^{3\mathrm{D}} \\ 0 \\ 0 \\ 0 \end{pmatrix} \tag{4.27}$$

while $\boldsymbol{\sigma}^{0\mathrm{D}} = \mathbf{0}$. This implies, that the unconstrained system is stress free. Now the unknown, non-vanishing total strains $\varepsilon_{22}^{1\mathrm{D}}, \varepsilon_{33}^{1\mathrm{D}}$ and $\varepsilon_{33}^{2\mathrm{D}}$ can be computed by inserting the strain states of Eq. (4.26) into Eq. (4.25) (2) and solving for the unknown strain components, such that the stress states given in Eq. (4.27) result.

In case the metal deforms elasto-plastically, the plastic strains $\boldsymbol{\varepsilon}_{\mathrm{p}}$ and the equivalent plastic strain $\varepsilon_{\mathrm{eq}}$ have to be computed prior to the determination of the unknown total strains. For this, the radial return method for an isotropic elasto-plastic von Mises theory is used (Simo and Hughes, 1998). The process is as follows (c.f. the supplemental material of Dyck et al. (2024a)):

1) An elastic trial stress state $\boldsymbol{\sigma}_{\mathrm{TR}}$ is computed by assuming vanishing plastic strains as outlined above.
2) If the resulting stress state is below the yield stress $\sigma_{\mathrm{F}}(\varepsilon_{\mathrm{eq}})$ no plastic correction is necessary. If $\sqrt{3/2}\|\mathbb{P}_2\left[\boldsymbol{\sigma}^{\mathrm{Tr}}\right]\| > \sigma_{\mathrm{F}}(\varepsilon_{\mathrm{eq}})$ a plastic correction is necessary.
3) The equivalent plastic strain and the plastic strain are computed as a function of an increment $\Delta\gamma$ of the consistency parameter by

$$\Delta\varepsilon_{\mathrm{pe}} = \sqrt{\frac{2}{3}}\Delta\gamma, \quad \Delta\boldsymbol{\varepsilon}_{\mathrm{p}} = \Delta\gamma\boldsymbol{N}, \quad \boldsymbol{N} = \frac{\boldsymbol{\sigma}'}{\|\boldsymbol{\sigma}'\|}.$$

4) The stress state $\boldsymbol{\sigma}(c_{\mathrm{H}}, \Delta\gamma, \varepsilon_{ij})$, where ε_{ij} denotes the unknown total strains, is computed by inserting the result of step 3) in Eq. (4.25) (2).
5) The stress state computed in step 4) is, together with the equivalent plastic strain of step 3), inserted into $\varphi(c_{\mathrm{H}}, \Delta\gamma, \varepsilon_{ij}) = 0$, which is solved for $\Delta\gamma$. A semi-analytical expression $\Delta\gamma = \Delta\gamma(c_{\mathrm{H}}, \varepsilon_{ij})$ as a function of the unknown strain components ε_{ij} and the concentration c_{H} results.
6) Using the result of step 4), the unknown strain components are determined such that the stress free conditions in the unconstrained directions outlined above hold. Using these results, the stress state $\boldsymbol{\sigma}(c_{\mathrm{H}})$ is specified for any concentration surpassing the yield stress.

This solution scheme can be solved semi-analytically by relying on the Computer-Algebra-System MAPLE.

For the known stress state $\boldsymbol{\sigma}(c_{\mathrm{H}})$, the chemical potential μ is an analytic function of the hydrogen concentration c_{H}. The phase-separation behavior of the specific metal-hydrogen system under consideration is most easily investigated by studying the monotonicity of the chemical potential (Dyck et al., 2024b;a). The monotony can be investigated by differentiating with respect to the concentration and studying the sign

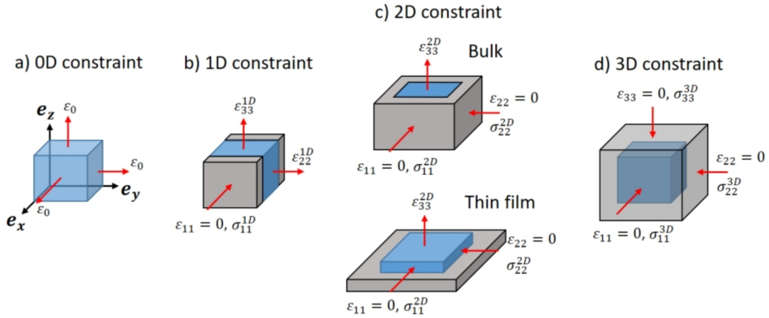

Figure 4.2: Metal-hydrogen systems with different constraint conditions. The grey frames visually indicate the directions of the constraint condition. Expansion of the sample cube is a) possible in all directions (0D constraint), b) suppressed in $\boldsymbol{e}_x$-direction, c) suppressed in $\boldsymbol{e}_x$- and $\boldsymbol{e}_y$-direction, and d) entirely suppressed by placing the cube in a rigid shell. The 2D constraint condition is equivalent to the 2D elastic constraint of an adhered thin film with thickness much smaller than the lateral dimensions. In this case, the lateral expansion is suppressed by the film's adherence to a rigid substrate, and the film can only expand in $\boldsymbol{e}_z$-direction (Laudahn et al., 1999). Figure based on Figure 2 from Dyck et al. (2024a).

of the resulting function. The differentiation results in

$$c_{\max}\frac{\partial^2\psi}{\partial c_{\mathrm{H}}^2} = \frac{\partial\mu}{\partial c_{\mathrm{H}}} = \frac{R\theta r}{r c_{\mathrm{H}} - c_{\mathrm{H}}^2} - \nu_0\eta_{\mathrm{H}} t - E_{\mathrm{HH}}, \tag{4.28}$$

where

$$t = \frac{\partial \operatorname{tr}(\boldsymbol{\sigma})}{\partial c_{\mathrm{H}}}. \tag{4.29}$$

Thus, for given temperature θ and hydrogen interaction strength E_{HH}, the resulting stresses either suppress or allow hydride formation to occur. As long as there exists a critical composition $c_{\mathrm{H}}^{\mathrm{sp}} \in [0, r]$, for which

$$\left.\frac{\partial\mu_{\mathrm{H}}}{\partial c_{\mathrm{H}}}\right|_{c_{\mathrm{H}}^{\mathrm{sp}}} = 0 \tag{4.30}$$

holds, phase separation is possible. Additionally, by rearranging Eq. (4.28), a critical temperature θ_{crit} can be determined, above which no phase separation is possible for given E_{HH} and t (Dyck et al., 2024b). In the following two subsections, we will use the proposed method to study hydride formation and its suppression in both the Pd-H and Nb-H system.

4.4.2 Palladium-Hydrogen system[5]

The material parameters considered in this subsection for the Pd-H system are summarized in Tab. 4.1. Pd thin films usually grow epitaxially with [111] texture. We here consider a Pd cubic single crystal with its [111] direction parallel to the $\boldsymbol{e}_{\text{z}}$-axis of the sample coordinate system,

θ	ν_0	r	E_{HH}	η_{H}
$300\,\text{K}$	$8.94 \times 10^{-6}\,\text{m}^3/\text{mol}$	0.62	$36.8\,\text{kJ/mol}$	0.063

C_{11}	C_{12}	C_{44}
$244\,\text{GPa}$	$173\,\text{GPa}$	$71.6\,\text{GPa}$

Table 4.1: Model parameters used in this subsection. All parameters are taken from Dyck et al. (2024b).

---

[5] Subsection 4.4.2 is based on the publication "Phase transformation in the palladium hydrogen system: Effects of boundary conditions on phase stabilities" (Dyck et al., 2024b).

c.f. Fig. 4.2. The stiffness in Voigt-Mandel notation is

$$\mathbb{C} = \boldsymbol{Q} \star \mathbb{C}_0 \hat{=} \begin{pmatrix} 270 & 158 & 142 & -31 & 0 & 0 \\ 158 & 270 & 142 & 31 & 0 & 0 \\ 142 & 142 & 285 & 0 & 0 & 0 \\ -31 & 31 & 0 & 82 & 0 & 0 \\ 0 & 0 & 0 & 0 & 82 & -43 \\ 0 & 0 & 0 & 0 & -43 & 112 \end{pmatrix} \text{GPa},$$

where $\boldsymbol{Q}$ is the rotation matrix rotating the $[111]$ to the $[001]$ plane. We assume no plastic deformations, i.e. a purely elastically deforming Pd film, and compute stress states using the scheme outlined above as

$$\begin{aligned} \boldsymbol{\sigma}^{1\mathrm{D}} &= \begin{pmatrix} -10 \\ 0 \\ 0 \\ 0 \\ 0 \\ 0 \end{pmatrix} c_{\mathrm{H}}\,\text{GPa}, \ \boldsymbol{\sigma}^{2\mathrm{D}} = \begin{pmatrix} -18 \\ -18 \\ 0 \\ 0 \\ 0 \\ 0 \end{pmatrix} c_{\mathrm{H}}\,\text{GPa and} \\ \boldsymbol{\sigma}^{3\mathrm{D}} &= \begin{pmatrix} -36 \\ -36 \\ -36 \\ 0 \\ 0 \\ 0 \end{pmatrix} c_{\mathrm{H}}\,\text{GPa}. \end{aligned} \tag{4.31}$$

The stresses of the constrained Pd-H system will strongly affect the stabilities of the solid solution phase and the hydride phase. The monotonicity of the chemical potential and thus the stability ranges of the phases in the (θ, c_{H})-space will be determined by the relation of E_{HH} and the stresses, which destabilize the hydride phase. This is illustrated in Fig. 4.3 for the chemical potential of the Pd-H system with the different

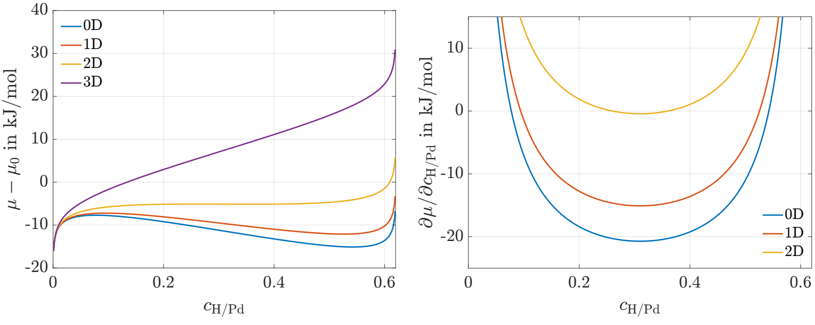

(a) **(b)**

Figure 4.3: a) Chemical potential of the linear-elastic Pd-H system with different constraint conditions as a function of the hydrogen concentration c_{H} at $\theta = 300\,\mathrm{K}$. For the free system (0D constraint) and the systems with 1D and 2D constraints, at 300 K, the chemical potential is a non-monotonous function, and hence there is a driving force for hydride formation. For 3D constraint, on the other hand, the solid solution phase is stable in the whole range of hydrogen concentrations. b) The derivative of the chemical potential with respect to the hydrogen concentration c_{H}, indicating phase-separation in the 2D constrained system at room temperature. Figure based on Figure 2 from Dyck et al. (2024b).

constraint conditions at $\theta = 300\,\mathrm{K}$. As long as $\partial\mu/\partial c_{\mathrm{H}} \leq 0$, there exists a critical temperature θ_{crit}, below which the chemical potential is a non-monotonic function in c_{H}. Then a thermodynamic driving force for the formation of the hydride phase exists. This statement is equivalent to the free energy being non-convex with respect to the concentration. According to Fig. 4.3 b), at room temperature even in a 2D constrained Pd-H system hydride formation is predicted. This depicts the ideal condition of thin films. These results distinguish the Pd-H system from the other widely studied model system of Nb-H, where the stress-impact upon 2D constraints suppresses hydride formation at all temperatures. This is considered in detail in the following subsection.

For the Pd-H system with a 3D constraint, $\theta_{\mathrm{crit}} < 0\,\mathrm{K}$ and thus hydride formation is suppressed at any temperature. This resembles the result of Alefeld (1972), yielding the absence of phase transformation in a 3D constrained Pd-H system. We note that the calculated critical temperature of the unconstrained Pd-H system of 686 K is larger than the experimental value of 563 K (Peisl, 1978). This is a known issue of the theory, see Wagner and Pundt (2016), that is often regarded for by an artificial reduction of the parameter r. However, this result primarily reveals the frontiers of the models describing the thermodynamics of metal-hydrogen systems. It might be more constructive to address possible H-concentration dependencies of the elastic and the electronic interactions.

For $\theta \leq \theta_{\text{crit}}$ critical concentrations c_{H}^{sp} result, where phase transformation is feasible from a thermodynamic point of view. The critical concentration of the systems with 0D, 1D and 2D constraints are shown in Fig. 4.4. Apparently, the miscibility gap areas shrink with increasing dimensionality of the constraints.

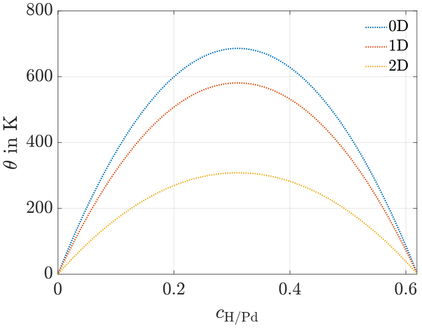

Figure 4.4: Two-phase field of the Pd-H system for different constraint conditions. The spinodal miscibility gaps are plotted. With increasing dimensionality of the constraint conditions the miscibility gaps shrink on the temperature and the concentration axes. Figure based on Figure 4 b) from Dyck et al. (2024b). The equilibrium concentrations of the original figure are not shown.

4.4.3 Niobium-Hydrogen system[6]

The investigated thin film Nb-H system deforms elasto-plastically for film thicknesses above a critical one. Below this critical film thickness, the behavior is purely elastic, i.e. plastic deformations are suppressed. This was shown experimentally by substrate curvature measurements, where the thin films are loaded by gaseous hydrogen and the curvature of the substrate is measured during hydrogen uptake. Using Stoney's formula (Stoney, 1909), the curvature is proportional to the in-plane stress state of the thin film. In Hamm et al. (2015) it was shown, that a $5\,\mathrm{nm}$ film deforms purely elastic, while a $40\,\mathrm{nm}$ film shows elasto-plastic deformations. This is shown in Fig. 4.5 a) in dots, wile fits to the measurements using a linear function for the $5\,\mathrm{nm}$ film and a piecewise linear function for the $40\,\mathrm{nm}$ film are shown as solid lines. As for the Pd-H system, we study phase separation behavior for a 0D and 2D constrained system. In addition, we investigate the influence of the occurrence of elasto-plastic deformations on the phase-separation behavior. However, in contrast to the Pd-H system, we consider an isotropic stiffness being determined by a Young's modulus E and Poisson's ratio ν.

For the 2D constrained system the occurring stresses are

$$\begin{aligned} \sigma_{11,\mathrm{e}}^{2\mathrm{D}} &= \sigma_{22,\mathrm{e}}^{2\mathrm{D}} = \frac{\eta_{\mathrm{H}} E}{\nu - 1} c_{\mathrm{H}} \\ \sigma_{11,\mathrm{p}}^{2\mathrm{D}} &= \begin{cases} \frac{\eta_{\mathrm{H}} E}{\nu - 1} c_{\mathrm{H}}, & c_{\mathrm{H}} \leq \hat{c}_{\mathrm{H}}, \\ m_{\mathrm{p}}^{2\mathrm{D}} c_{\mathrm{H}}, & c_{\mathrm{H}} > \hat{c}_{\mathrm{H}}. \end{cases} \end{aligned} \tag{4.32}$$

In Eq. (4.32), $\hat{c}_{\mathrm{H}} = 0.12\,\mathrm{H/Nb}$ is the concentration, for which the first plastic deformations occur and $m_{\mathrm{p}}^{2\mathrm{D}}$ is the slope of the stresses in the

---

[6] Subsection 4.4.3 is based on the publication "Phase transformation in the Niobium Hydrogen system: Effects of elasto-plastic deformations on phase stability predicted by a thermodynamic model" (Dyck et al., 2024a).

θ	ν_0	r	E_{HH}	η_{H}
$300\,\mathrm{K}$	$9.71 \times 10^{-6}\,\mathrm{m}^3/\mathrm{mol}$	0.67	$20.2\,\mathrm{kJ}/\mathrm{mol}$	0.058

E	ν	σ_{F0}	h	$m_{\mathrm{p}}^{\mathrm{2D}}$
$13\,\mathrm{GPa}$	0.3	$1365\,\mathrm{MPa}$	$10.7\,\mathrm{GPa}$	$-1.1\,\mathrm{GPa}$

Table 4.2: Model parameters used in this subsection. All parameters are taken from Dyck et al. (2024a).

plastic regime, which results from the scheme outlined above. Due to the assumed linear hardening of Nb, the stresses increase linearly with the concentration in the plastic regime. All material parameters considered are summarized in Tab. 4.2.

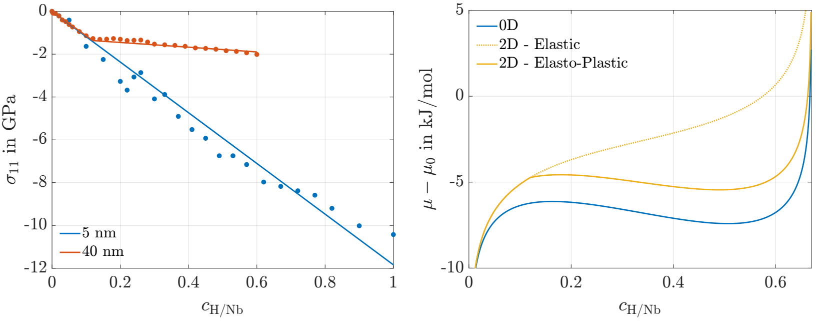

(a) **(b)**

Figure 4.5: a) Experimentally determined stresses in 5 and 40 nm thin Nb films using the substrate curvature measurement (dotted) Hamm et al. (2015) and piecewise linear fits to the data (solid lines), c.f. Eq. (4.32). b) Chemical potential of a linear elastic $5\,\mathrm{nm}$ and an elasto-plastically $40\,\mathrm{nm}$ deforming Nb-H film at $\theta = 300\,\mathrm{K}$ using the model and stress states identified. Figure based on Figures 1 c) and 3 a) from Dyck et al. (2024a).

We now proceed by investigating the chemical potential as a function of the concentration. To this end, a temperature of $\theta = 300\,\mathrm{K}$ is chosen and the chemical potential μ for purely elastic deformation (dotted yellow curve), mimicking a $5\,\mathrm{nm}$ film, and elasto-plastic deformation (solid yellow curve), mimicking a $40\,\mathrm{nm}$ film, are depicted in Fig. 4.5 b). The elastically deforming Nb thin films suppress phase separation at room temperature. This is reproduced by the derived model, as indicated by the monotonous increase of the chemical potential with respect to the overall hydrogen concentration in the 2D constrained system. This shows, that occurring stresses suppress phase separation at room temperature, in contrast to the 2D constrained Pd-H system studied in the previous subsection. This different behavior results mainly from the lower hydrogen-hydrogen interaction strength E_{HH} in the Nb-H, compared to the Pd-H system, where $E_{\mathrm{HH}} = 36.8\,\mathrm{kJ/mol}$. The stability of the hydride-phase is governed by the interplay of the stabilizing E_{HH} and the destabilizing contribution of $\eta_{\mathrm{H}}\nu_0\mathrm{tr}\,(\boldsymbol{\sigma})$. However, as plastic deformations drastically reduce occurring mechanical stresses, a $40\,\mathrm{nm}$ thin film with a slope of $m_{\mathrm{p}}^{\mathrm{2D}} = -1.1\,\mathrm{GPa}$ shows phase separation at room temperature. The proposed model confirms this finding, as the related chemical potential is a non-monotonous function of the concentration at room temperature in the 2D constrained case with plastic deformation.

In addition to the occurrence of phase separation, the outlined model allows to compute critical concentrations $c_{\mathrm{H}}^{\mathrm{sp}}$ as a function of temperature, c.f. Eq. (4.30). Results of this investigation are depicted in Fig. 4.6 for both $5\,\mathrm{nm}$ and $40\,\mathrm{nm}$ films in addition to a stress free system. Obviously, the occurrence of plastic deformations drastically increases the critical concentrations and the critical temperature θ_{crit} for hydride formation. In fact, the predicted critical temperature for the $40\,\mathrm{nm}$ film is only slightly lower compared to the stress free system, as occurring stresses are strongly reduced by plastic deformations. In the case of elastically deforming Nb with 2D constraint such as the $5\,\mathrm{nm}$ film, on the contrary, the critical temperature for hydride formation is about $160\,\mathrm{K}$. As a final note it is pointed out that Eq. (4.30) is discontinuous at $c_{\mathrm{H}} = \hat{c}_{\mathrm{H}}$, as the slope in the stresses changes discontinuously. This implies, that for concentrations around the onset of plastic deformations the predictions of the critical concentration are to be considered inaccurate, as this behavior is obviously non-physical.

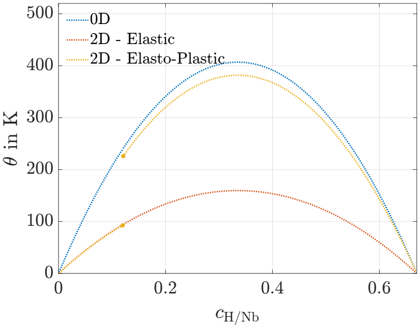

Figure 4.6: Critical concentrations of α- and hydride-phase for both films as a function of temperature. As the derivative of the chemical potential is non-continuous at $c_{\mathrm{H}} = \hat{c}_{\mathrm{H}}$ for the $40\,\mathrm{nm}$ film, a jump is predicted in the critical concentrations. The critical temperatures of hydride formation strongly differ for both films, enabling hydride formation at room temperature in the plastically deforming $40\,\mathrm{nm}$ film, while it is suppressed in the elastically deforming $5\,\mathrm{nm}$ film. Figure based on Figure 3 b) from Dyck et al. (2024a). The equilibrium concentrations of the original figure are not shown.

For a generalization of the obtained results we investigate different magnitudes of slopes $m_{\mathrm{p}}^{2\mathrm{D}}$ for each constraint in the following to study the influence of the hardening behavior on the thermodynamics of the system. Thereby, $m_{\mathrm{p}}^{2\mathrm{D}}$ is limited by a vanishing slope, i.e. no hardening, and the respective elastic slope, implying $m_{\mathrm{p}}^{2\mathrm{D}} \in \left[0, m_{\mathrm{e}}^{2\mathrm{D}}\right]$. The derivative of trace of the stress state, introduced in Eq. (4.29), can now be computed via $t^{2\mathrm{D}} = \sum_i m_i^{2\mathrm{D}}$. To illustrate the effect of this change, the critical temperature θ_{crit} is computed for a 0D and 2D constraint condition for both purely elastically deforming and elasto-plastically deforming Nb. The results are depicted in Fig. 4.7. Apparently, the critical temperature of hydride formation changes linearly with the plastic slope m_{p} for 2D constrained systems. For vanishing slopes $m_{\mathrm{p}} = 0$, the critical temperature of each film coincides with an unconstrained system, while at maximum slope, i.e. a slope identical to the elastic slope, the critical temperature is identical to the elastically deforming Nb. As a final note we want to point out, that $\theta_{\mathrm{crit}}^{0\mathrm{D}} = 407\,\mathrm{K}$ differs from the bulk value of $444\,\mathrm{K}$. This is due to the parameter E_{HH}, which differs in miniaturized Nb-H systems from the bulk value (Wagner et al., 2019).

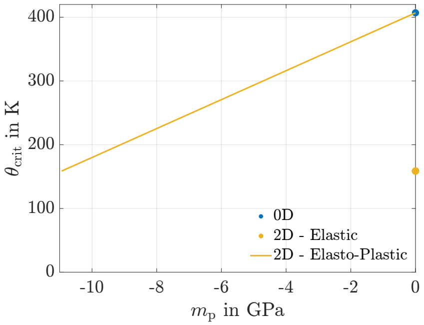

Figure 4.7: Critical temperatures θ_{crit} for different constraints for elastically and elasto-plastically deforming Nb for different slopes m_{p}. Figure based on Figure 4 from Dyck et al. (2024a). The results for the 1D constraint in the original figure are not shown.

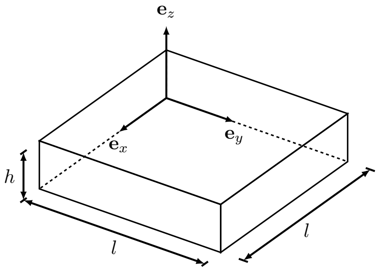

Figure 4.8: Schematic of the thin film geometry and the used coordinate system. Figure based on Figure 2 from Dyck et al. (2025).

4.5 Numerical results for the Niobium-Hydrogen system[7]

4.5.1 Simulation model

The thin Nb film adhered to a rigid substrate and exposed to gaseous hydrogen at its top is modeled as a cuboid, c.f. Fig. 4.8, while the dimensions l and h are summarized in Tab. 4.3. The domain is discretized by hexahedral elements with an edge length of $2.5\,\mathrm{nm}$. A resolution study using 1.5 and $2\,\mathrm{nm}$ edge length has revealed no deviation in the fields of interest, indicating a sufficient resolution. The adherence of the thin film to the substrate is introduced by means of a clamped condition at the bottom. In order to approximate the large in-plane extension in comparison to the height of the thin film, i.e. $h \ll l$, Periodic Boundary Conditions (PBCs) are used on the sides of the domain for $\underline{c}_\mathrm{E}$ and $\underline{\hat{\mu}}_\mathrm{E}$, while $\underline{u}_\mathrm{E}$ is restricted by symmetry conditions. On top, mimicking the exposure to an atmosphere with gaseous hydrogen, i.e. an open system,

---

[7] Section 4.5 is based on section 5 of the publication "Hydride formation in open thin film metal hydrogen systems: Cahn-Hilliard-type phase-field simulations coupled to elasto-plastic deformations" (Dyck et al., 2025).

a chemical potential is prescribed.

For all simulations conducted, the concentration is prescribed homogeneous initially and the corresponding strains, chemical potential, internal variables and stresses are computed in an initial step. All geometric and material parameters describing both the mechanical as well as the chemical properties are summarized in Tab. 4.3, where most material parameters are taken from Dyck et al. (2024a). Parameters not used in Dyck et al. (2024a) are the diffusion constant D and the interfacial parameter λ_c. The diffusion constant is chosen arbitrarily, as the main concern of this section is the study of an equilibrium between α- and hydride-phase. As the equilibrium state will be identical, irrespective of the chosen diffusion constant, this is suitable (Di Leo et al., 2014; Miehe et al., 2014). The interface parameter λ_c, specifying the width of the phase-separating interface, is chosen such that the used element size of $2.5\,\mathrm{nm}$ is at least five times smaller than the interface width, c.f. Cahn and Hilliard (1958), Di Leo et al. (2014) and Castelli et al. (2021) for details.

Symbol	Value	Symbol	Value
l	$200\,\mathrm{nm}$	h	$40\,\mathrm{nm}$
E	$132\,\mathrm{GPa}$	ν	0.3
σ_{F0}	$1365\,\mathrm{MPa}$	γ	$10.7\,\mathrm{GPa}$
R	$8.314\,\mathrm{J/mol/K}$	θ	$300\,\mathrm{K}$
$\nu_0 = 1/c_{\mathrm{max}}$	$9.713 \times 10^3\,\mathrm{mm}^3/\mathrm{mol}$	μ_0	$-15.2\,\mathrm{kJ/mol}$
η	0.058	E_{HH}	$20.2\,\mathrm{kJ/mol}$
λ_c	$1 \times 10^{-5}\,\mathrm{mm}$	r	0.67

Table 4.3: Geometrical, mechanical and chemical parameters. Table based on Table 1 from Dyck et al. (2025).

4.5.2 Homogeneous boundary conditions

We start by investigating model predictions for a homogeneous boundary chemical potential $\bar{\mu}$, resembling an open system exposed to gaseous hydrogen with constant and homogeneous partial pressure p_{H2} at the top surface of the film. We compare simulation results to the presented analytic considerations on the elasto-plastically deforming Nb-H system, c.f. Sec. 4.4, in order to verify the implementation presented in Sec. 4.3. In an adhered thin film loaded with hydrogen, the in-plane stress state can be computed analytically as a function of c_{H} for elastic and elasto-plastic deformations, as long as the concentration is homogeneous. For an elastic film no phase separation is present at room temperature, as the large compressive stresses suppress hydride formation and μ is monotonically increasing in c_{H}. However, in the elasto-plastic case, the chemical potential is non-monotonic due to the lower stresses. As soon as the coherency strain energy barrier of Schwarz and Khachaturyan (1995) and Schwarz and Khachaturyan (2006) is surpassed, i.e. $c_{\mathrm{H}} > c_{\alpha}^{\mathrm{sp}} \approx 0.17\,\mathrm{H/Nb}$ (Dyck et al., 2024a), the system will transform into the hydride-phase and take up hydrogen until it has fully transformed. As soon as $c_{\mathrm{H}} > c_{\alpha}^{\mathrm{sp}}$ the film takes up hydrogen until hydride has formed everywhere, which results in a flat plateau in the μ, c_{H}-diagram.

Both an elastically deforming as well as an elasto-plastically deforming film are simulated using the model and implementation outlined. The initial concentration is chosen to be $0.05\,\mathrm{H/Nb}$ at $t = t_0$, as the focus is on the onset of hydride formation. Subsequently, the boundary chemical potential is increased stepwise, mimicking a stepwise increase in p_{H2}, and held constant until an equilibrium between hydrogen in the thin film and the gaseous hydrogen has been reached, i.e. μ is homogeneous in the entire film. For this, the boundary condition is prescribed homogeneously on all nodes on top of the simulation domain. Results of Finite Element simulations are shown in Fig 4.9 in comparison with model predictions, where the numerical results are shown as black dots and dashed lines. Equilibrium configurations, i.e. simulation results with a homogeneous chemical potential and a homogeneous hydrogen concentration in the entire film, are denoted by dots. These are connected through non-equilibrium states indicated by dashed lines. Some important time steps in the simulation for $t > t_0$ are marked separately as discussed below for both the elastic and the elasto-plastic films. Until the onset of plastic deformation, both models result in the same μ, c_{H}-curve. Only after the onset of plastic deformation at $t = t_7$, where the concentration induced stresses surpass the yield limit, the curves separate.

The elastically deforming film does not show phase separation. Instead the α-phase takes up large amounts of hydrogen without forming the hydride, even for large hydrogen pressures, c.f. the time steps t_{10} and following denoted in blue in Fig. 4.9 a). In order to increase the absorbed amount of interstitial hydrogen within the α-phase, a large increase in the partial pressure of gaseous hydrogen is necessary, c.f. the increase in the boundary value from t_7 to t_{25} (blue). As a final remark concerning the purely elastic situation we want to point out, that the Finite Element result is identical to the analytical model prediction.

In contrast, the elasto-plastically deforming film forms a hydride-phase as soon as the increasing hydrogen gas pressure leads to a concentration $c_{\mathrm{H}} > c_{\alpha}^{\mathrm{sp}}$ at $t > t_{13}$. This will happen at the film surface first, since the increasing chemical potential is applied at the surface in the model. Hence, the film transforms into the hydride-phase at the entire top surface, due to the chosen homogeneous boundary condition. However, during $t_{13} < t < t_{14}$ the film is not in thermodynamic equilibrium and the hydride continues to grow all the way down to the substrate, where growth occurs solely in $\boldsymbol{e}_z$ direction. Thus the thin film takes up hydrogen at a constant chemical potential until it is fully transformed into the hydride phase, which can be seen by the horizontal dashed line in Fig. 4.9 connecting t_{13} and t_{14} (orange). This is a direct consequence of the elastic energy barrier resulting from the coherent phase interfaces according to the theory of Schwarz and Khachaturyan (1995) and Schwarz et al. (2020). Once the entire film has transformed, the chemical potential μ resulting from the Finite Element simulation again follows the analytic model of Sec. 4.4, c.f. the time steps in orange in Fig. 4.9 a). To more clearly outline the hydride formation, Fig. 4.9 b) shows non-equilibrium time steps of the phase boundary between the hydride- and α-phase in the range $t_{13} < t < t_{14}$. As the formation of hydride is initiated on the entire top surface, the only growth mode is in $\boldsymbol{e}_z$-direction. With increasing time, the phase boundary grows towards the substrate interface, while the thin film takes up hydrogen at the given constant boundary chemical potential, i.e. a constant hydrogen gas pressure p_{H2}. At $t = t_{14}$ the system is in equilibrium, i.e. the chemical potential is homogeneous, and has formed hydride entirely.

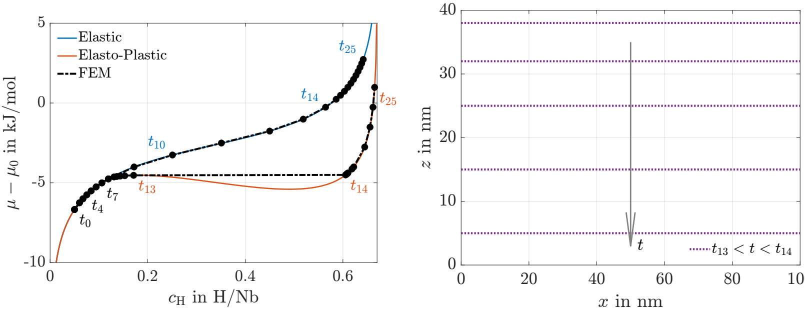

(a) **(b)**

Figure 4.9: a) Evolution of the total hydrogen concentration for a stepwise increasing homogeneous chemical potential. Both a linear elastic and an elasto-plastic material behavior are studied. The results of an analytic consideration presented in the previous section are shown in color, while the numerical results are shown in black. The dots mark time steps with prescribed chemical potential at equilibrium, while the dotted lines are the non-equilibrium states. Some simulation times are marked with the respective step number as discussed in the text. b) Propagation of the phase boundary between the α- and hydride-phase for $t_{13} < t < t_{14}$. The hydride-phase grows in $\boldsymbol{e}_z$-direction starting at the top. All lines shown are non-equilibrium states. As soon as $t \geq t_{14}$ the entire system has formed the hydride. Figure based on Figure 3 from Dyck et al. (2025).

4.5.3 Fluctuating boundary conditions

We now impose a fluctuating boundary condition $\bar{\mu}$, i.e. an artificially fluctuating hydrogen gas pressure p_{H2} on the top of the thin film, in order to study equilibrium concentrations, stress states, height changes of the thin film and hydride geometries during coexistence of α- and hydride-phase, observed in experiments presented in Burlaka et al. (2017), Burlaka et al. (2016) and Wagner et al. (2019). In order to do this, a homogeneous initial concentration of $0.13\,\mathrm{H/Nb}$ is applied. As this simulation is computationally more demanding and the initial steps are identical to the results shown above, this larger concentration value is chosen. Again, by prescribing a boundary value of the chemical potential we initiate hydride formation. Instead of prescribing a homogeneous boundary condition as in the discussion before, we use a locally fluctuating value. This only locally leads to concentrations surpassing the coherency strain energy barrier, while at other positions in the simulation domain this energy barrier is not surpassed. Thus, hydride precipitates form locally within the α-phase and their nucleation and growth is subsequently studied.
The fluctuating boundary value is chosen in $\bar{\mu} \in [-5.1, -3.9]\ \mathrm{kJ/mol}$ and applied during $t_0 < t \leq t_1$. As soon as locally a hydride precipitate forms in the simulation domain, $\bar{\mu} = -4.9\,\mathrm{kJ/mol}$ is applied and held constant, until an equilibrium is reached in the entire film at $t = t_2$. Subsequently, $\bar{\mu}$ is increased stepwise by $0.1\,\mathrm{kJ/mol}$ during $t \in [t_3, t_4, t_5, t_6]$ and the growth of the precipitate as well as equilibrium concentrations are investigated further. All equilibrium states are depicted in Fig. 4.10 a) and connected by a dashed line, denoting the non-equilibrium states. In Fig. 4.10 b), the volume averaged concentration $\langle c_{\mathrm{H}} \rangle$ in $\mathrm{H/Nb}$ is shown during this simulation, while in Fig. 4.10 c) - f) the resulting concentration field is shown for several time steps. In the equilibrium state at $t = t_2$, part of the thin film has transformed to the hydride-phase, c.f. Fig. 4.10 d).

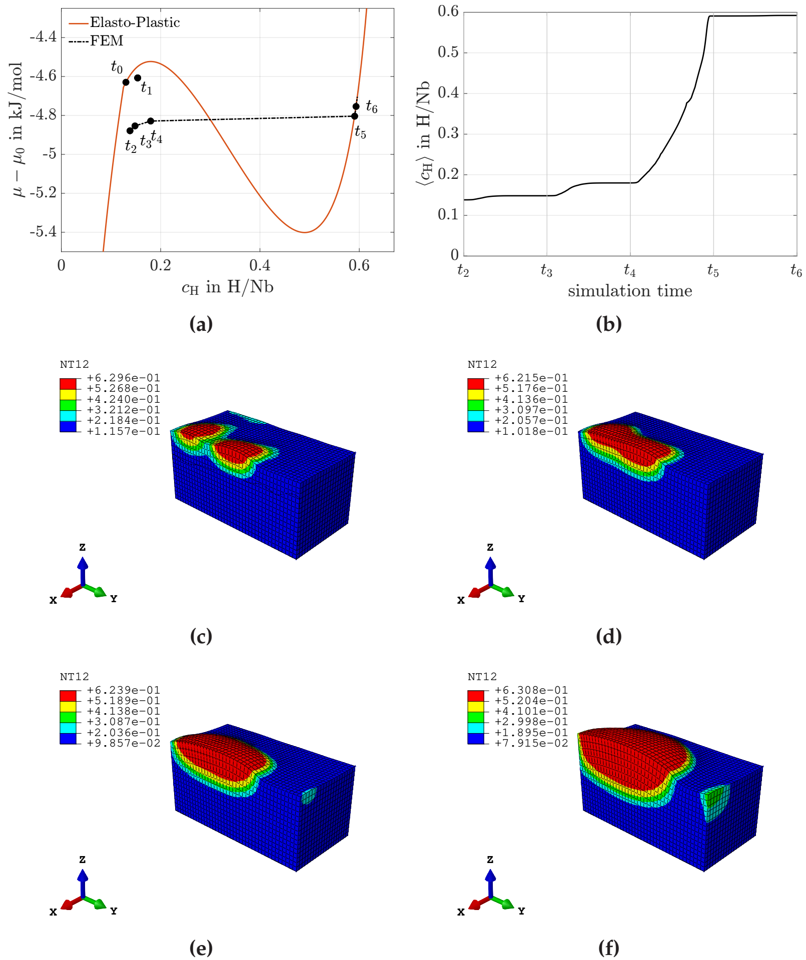

(a) **(b)**

(c) **(d)**

(e) **(f)**

Figure 4.10: a) $\mu(c_{\mathrm{H}})$ predicted by the analytical model of Sec. 4.4 is shown in orange. Finite Element results averaged over the simulation domain are shown in black. At $t = t_0$ the simulation is initiated in a homogeneous state. A fluctuating $\bar{\mu}$ is applied on top of the film and held until, at $t = t_1$, hydride has formed. Subsequently $\bar{\mu}$ is applied homogeneously until an equilibrium is reached at $t = t_2$. From then on, $\bar{\mu}$ is increased stepwise for $t > t_2$ and the resulting equilibrium states are depicted by dots. b) The volume averaged hydrogen concentration $\langle c_{\mathrm{H}} \rangle$ in the film for increasing time. c) - f) Simulation results for the concentration c_{H} at several time steps. A cut through the simulation domain at $x = 50\,\mathrm{nm}$ in the $\boldsymbol{e}_y$-$\boldsymbol{e}_z$-plane is depicted. c) c_{H} at $t = t_1$. d) c_{H} at $t = t_2$. e) c_{H} at $t = t_3$. f) c_{H} at $t = t_4$. Figure based on Figure 4 from Dyck et al. (2025).

Subsequent increases in $\bar{\mu}$ lead to an uptake of hydrogen, a growth of the precipitate and equilibrium states at $t = t_3$ and $t = t_4$, where both phases coexist, because the energy barrier has not yet been overcome in the entire film, see also Fig 4.10 e) and f). Accordingly, a subsequent increase in $\bar{\mu}$ from t_4 to t_5 leads to hydride-phase formation in the entire film, visible by the sharp increase in $\langle c_\mathrm{H} \rangle$ during $t_4 < t \leq t_5$ shown in Fig. 4.10 b). After the entire film has formed hydride, i.e. for $t > t_5$, a small increase in $\bar{\mu}$ leads only to a slight increase in $\langle c_\mathrm{H} \rangle$, as expected when considering the analytic model. Again, as in the discussion above, the Finite Element results are in good agreement with the analytical model prediction. A slight deviation is due to heterogeneous stress and plastic strain distribution, which will be discussed in Fig. 4.11 b) - d).

In order to reveal the effects of interface stresses and plastic strains on the phase transformation we proceed by studying the coexistence state of α- and hydride-phase in the model with fluctuating chemical potential in more detail, c.f. Fig. 4.11 a) - d). Shown are the concentration c_H, normal stress components σ_{11} and σ_{33} in addition to the equivalent plastic strain ε_eq along a vertical path, i.e. along the $\boldsymbol{e}_z$-axis, for the equilibrium states t_2, t_3, t_4 and t_5. The in-plane stress σ_{22} is not shown, as it is, due to the isotropic stiffness tensor, identical to σ_{11}. In addition, black dotted lines are shown, in order to indicate the interface of α- and hydride-phase to analyze the stress states depicted in Fig. 4.11 b) - c). The interface position is determined by averaging the maximum and minimum concentration along the path and choosing the z-coordinate, where c_H exceeds this value. For t_2 and t_3 the interface position coincides.

Notably, during the transformation stages, where α- and hydride-phase coexist, the equilibrium concentrations in both phases differ from their theoretical values predicted in Dyck et al. (2024a), c.f. Fig. 4.11 a). This results from the strongly heterogeneous stress state and corresponding stress gradients, c.f. Fig. 4.11 b) - c), when crossing the phase interface in the coexistence of α- and hydride-phase. Within the α-phase, i.e. close to the film-substrate interface below the hydride growing from the top,

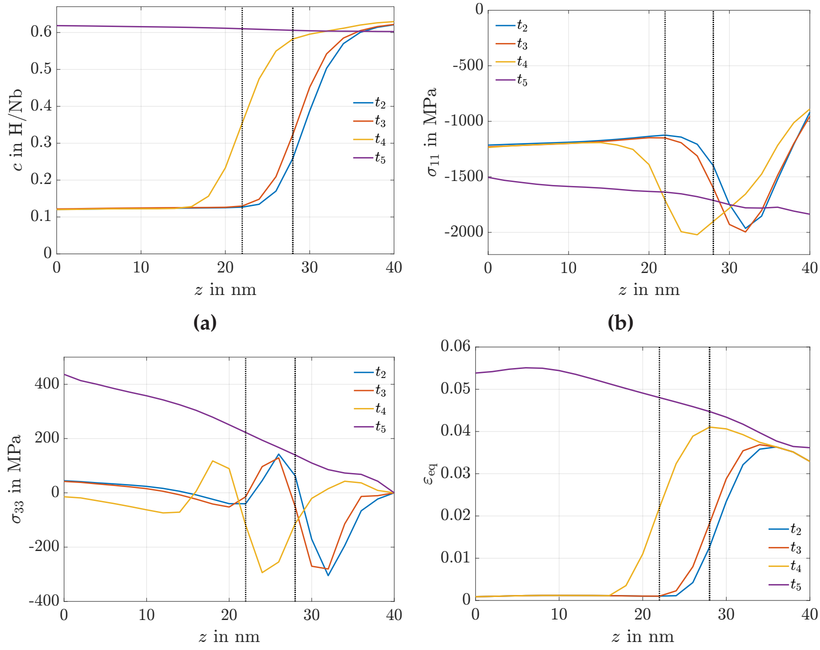

(a) **(b)**

(c) **(d)**

Figure 4.11: Concentration, stress profiles and equivalent plastic strain along a path in $\boldsymbol{e}_z$ direction. The simulation time increases from t_2 to t_5. The phase boundary between hydride and α-phase is indicated by the dotted black line. a) Conentration along the path. b) In-plane stress component σ_{11} along the path. σ_{22} is similar due to the assumed isotropic stiffness tensor. c) Out-of-plane stress component σ_{33} along the path. d) Equivalent plastic strain $\varepsilon_{\mathrm{eq}}$ along the path. Figure based on Figure 5 from Dyck et al. (2025).

the in-plane stresses σ_{11} and σ_{22} are homogeneous and the out-of-plane stresses σ_{33} vanish, as is to be expected for a single phase field in a 2D constrained system. However, in the vicinity of the phase interface this drastically changes. As there is a large concentration step between the hydride-phase and the α-phase and the phase interface is coherent, the stresses increase gradually and significantly in magnitude when crossing the phase-interface. This is due to the fact, that the hydride can not expand in-plane, as it is surrounded by α-phase, c.f. Fig. 4.12 b), and its out-of-plane expansion is hindered as well by the adjacent α-phase, yielding additional in-plane stress contributions due to Poisson's effect. Hence, increasingly compressive in-plane stresses result when crossing the phase interface in direction from the α-phase to the hydride-phase. Only at the free boundary, i.e. close to $z = 40\,\mathrm{nm}$, the hydride expands not only vertically but also in-plane, as it is not surrounded by α-phase. This leads to decreasing in-plane stresses σ_{11} and σ_{22} at the top of the film. Consequently, the out-of-plane stresses σ_{33} are also markedly heterogeneous in the vicinity of the phase interface. At the stress free top of the thin film they vanish, while they vary significantly when crossing the phase interface.

In vertical direction the hydride-phase imposes tensile stress in the α-phase, while the α-phase imposes compressive stress in the hydride due to the different local hydrogen concentrations and the resulting different lattice expansions. Remarkably, the stress gradients resulting at the phase interfaces in Fig. 4.11 b) - c) impose a feedback-loop to the local hydrogen concentrations in the vicinity of the phase interface, where the local hydrogen concentrations differ from the equilibrium concentrations within the phases. Hence, coupled stress and concentration gradients result at the phase interfaces, leading to the minimization of the total strain energy of the system. According to Fig. 4.11 a), the concentration gradients extend up to $5\,\mathrm{nm}$ in both directions in the vicinity of the phase interface, with increased concentration in the α-phase and depleted hydrogen concentration in the hydride-phase. We note, that this value of $5\,\mathrm{nm}$ is also a result of the choice of $\lambda_{\mathrm{c}} = 1 \times 10^{-5}\,\mathrm{mm}$.

The evolution of these heterogeneous stress and concentration fields can be easily followed by comparing the numerical results of t_2, t_3 and t_4, which all show qualitatively similar behavior but at different positions in the film height, due to the moving interface, see Fig. 4.11 a) - d). At $t = t_5$ the entire film has transformed into the hydride-phase and the phase interface has vanished. As mentioned above, the resulting concentrations and stresses are still not fully homogeneous, due to the heterogeneity in the equivalent plastic strains $\varepsilon_{\mathrm{eq}}$ in previous simulation steps, c.f. Fig. 4.11 d). This heterogeneity arises due to the heterogeneous hydrogen concentration and the interface between the α- and the hydride-phase. It explains, why the results averaged for the entire film do not match the analytic predictions discussed in Fig. 4.10 a). Ultimately this heterogeneous distribution is a result of the fluctuating chemical potential applied on top of the simulation domain. A final remark for these results concerns the tensile stress σ_{33} at $z = 0\,\mathrm{nm}$ for $t = t_5$, c.f. Fig. 4.11 c). This results from the heterogeneous distribution of plastic strains within the thin film, c.f. Fig. 4.11 d), and does not occur in the simulations presented in Fig. 4.9, where all fields are homogeneous. This tensile out-of-plane stress is only one-third of the in-plane stresses, but clearly affects the equilibrium concentration in the hydride-phase, which is larger at the bottom, c.f. Fig. 4.11 a).

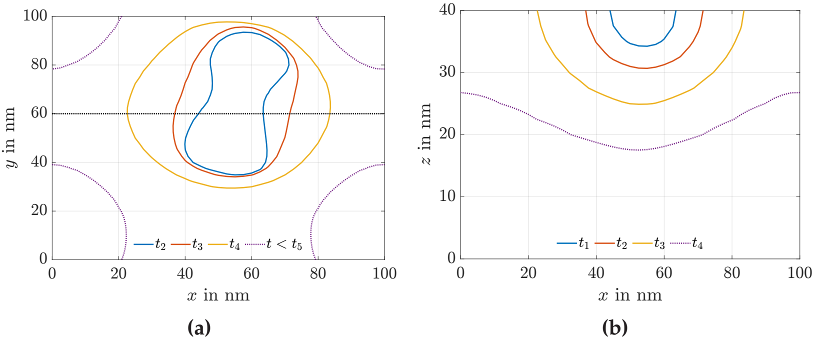

(a) **(b)**

Figure 4.12: Concentration isolines $c_{\mathrm{H}} = 0.5\,\mathrm{H/Nb}$ in equilibrium states $t \in [t_2, t_3, t_4]$. In addition, a non-equilibrium state $t_4 < t < t_5$ is shown dotted. a) View from top. A dotted black line is included to show the position of a vertical cut at $y = 60\,\mathrm{nm}$ through the film, shown in b). Figure based on Figure 6 from Dyck et al. (2025).

We now proceed by studying the geometries of hydride precipitates surrounded by α-phase and their growth due to increasing p_{H2}. Results in the form of concentration isolines $c_{\mathrm{H}} = 0.5\,\mathrm{H/Nb}$ are depicted in

Fig. 4.12 when viewed from above (a) and for a vertical cut (b). The resulting surface displacement of the film in $\boldsymbol{e}_z$-direction is shown in Fig. 4.13 b). In Fig. 4.12 the y-position for the vertical cut is indicated in a) by a dotted black line. Again, the equilibrium states t_2, t_3 and t_4 are shown. In addition, the dotted violet line shows a non-equilibrium state $t_4 < t < t_5$. This allows us to discuss the evolution of the precipitate geometry before the entire film has transformed into the hydride-phase. Initially, at $t = t_2$, a non-circular hydride precipitate has formed close to the film surface, emerging from two adjacent circular hydride nuclei. With increasing p_{H2} this irregular shape grows and becomes circular at t_3 and t_4. In our interpretation this is due to the in-plane stress state, that favors circular precipitate shapes. The hydride geometry shown in Fig. 4.12 a) for $t \in [t_2, t_3, t_4]$ closely resemble the experimentally determined geometries with radii up to $40\,\mathrm{nm}$. Both small regions with irregular shapes, as well as larger regions with circular shapes have been reported to form in the same film (Burlaka et al., 2016). As the simulation domain is limited in space for computational reasons, we do not see these shapes at the same equilibrium steps, but throughout several equilibrium steps. The experimentally determined range of radii of the precipitates resembles the radius of the precipitate shown in Fig. 4.12 a) and its evolution with p_{H2}. However, in contrast to results presented in Nörthemann and Pundt (2008), the precipitates do not grow straight to the bottom of the film-substrate interface in a cylindrical shape. Instead, before the hydride-phase grows all the way to the substrate in our simulations, the entire surface of the film has transformed to the hydride-phase. This is indicated by the non-equilibrium state shown as dotted line in both Fig. 4.12 a) and b). In our interpretation, this deviation of the simulation results and the experimental observations results from the coherent film-substrate interface in our simulations. Even though, as mentioned above, the plasticity parameters are determined by means of a semicoherent film-substrate interface, the coherency in our simulations introduces additional compressive in-plane stresses at the film-substrate interface, which prevent the growth of the precipitates towards the substrate, before the entire top of the simulated film has formed the hydride-phase.

Finally, in Fig. 4.13, we compare the simulated changes in height to experimentally determined values. Both the maximum displacement $u_3^{\max}$ in $\boldsymbol{e}_z$-direction of the top (dotted line, right axis), as well as the difference $\Delta u_3 = u_3^{\max} - u_3^{\min}$ between the maximum and minimum displacement (solid line, left axis) are shown in Fig. 4.13 a). To make this difference Δu_3 more clear, the u_3 displacement in $\boldsymbol{e}_z$-direction is depicted in Fig. 4.13 b) for $t \in [t_2, t_3, t_4, t_5]$. With time, the maximum displacement increases, especially when the entire film forms hydride in the range $t_4 < t < t_5$, in close analogy to the uptake of hydrogen shown in Fig. 4.10 b). The maximum displacement $u_3^{\max}$ observed in our simulation is slightly below the maximum observed in the experiments, which is at $4.6\,\mathrm{nm}$, c.f. Nörthemann and Pundt (2008). As dislocation steps and semicoherent interfaces were both not explicitly considered in our model but observed in Nörthemann and Pundt (2008), this model prediction is in pretty good agreement to the experimental results. Concerning Δu_3, i.e. the difference in u_3 displacement between α- and hydride-phase, the simulated results are in a similar range as the observed ones. The growth of the precipitates discussed above proceeds first in-plane and only later down to the substrate interface, thus the difference in height between α- and hydride-phase is not as pronounced as in the experiments, where, on average, a difference of $2.2\,\mathrm{nm}$ was observed. This is in agreement with the considerations presented in Nörthemann and Pundt (2008), where it was shown, that only cylindrical precipitates can reproduce the experimentally observed height differences. However, as we do not incorporate stress relaxation at the interface between substrate and Nb film, these can not be reproduced by our phase-field model.

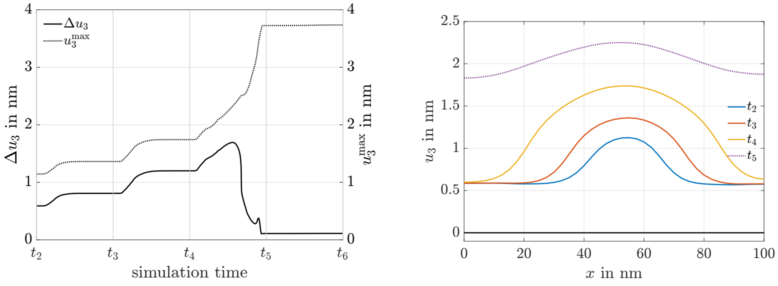

(a) **(b)**

Figure 4.13: a) Maximum displacement (dotted line, right axis) $u_3^{\max}$ in $\boldsymbol{e}_z$-direction and difference between maximum and minimum displacement (solid line, left axis) Δu_3 on the top of the model at $z = z_{\max}$ as a function of time. b) Displacement u_3 in $\boldsymbol{e}_z$-direction along a path on top of the thin film for four time steps. The simulation time increases from t_2 to t_5. In black the displacement without hydrogen loading is shown. Figure based on Figure 7 from Dyck et al. (2025).

4.6 Conclusion[8]

In the present chapter, a chemo-mechanically coupled phase-field model is presented, in order to study phase transformation in hydride forming thin-film open metal hydrogen systems. The open Pd-H and Nb-H systems are utilized as a model, due to the abundance of experimental data available. The model combines a Cahn-Hilliard-type diffusion equation and the balance of linear momentum in a small strain setting and includes both chemical and plastic deformations. The free energy density is chosen as the thermodynamic potential and additively decomposed into a chemical part, introducing the tendency of the metal hydrogen system to form α- and hydride-phases, an elastic part, introducing deformations of Nb, and an interfacial contribution introducing the system's tendency to minimize interfaces between both

---

[8] This section is based on section 6 of the publication "Hydride formation in open thin film metal hydrogen systems: Cahn-Hilliard-type phase-field simulations coupled to elasto-plastic deformations" (Dyck et al., 2025).

phases. The chemical and the elastic part are informed by experiments. The implementation of the model using a splitting method and the commercial Finite Element solver ABAQUS is presented. Within the model framework, the α-phase transforms locally into the hydride-phase as soon as the coherency strain energy barrier, computed analytically, c.f. Fig. 4.9, is surpassed due to increasing hydrogen concentration. As open systems are considered, the hydrogen gas pressure is directly prescribed as a boundary condition on the simulation domain. Both analytical investigations as well as numerical simulations are conducted, the latter using both a homogeneous as well as a fluctuating boundary condition for the chemical potential. The former allows us to verify the simulation results against analytic predictions, while the latter gives insight into the coexistence of hydride- and α-phase.
The main results are summarized as follows:

- In the thin film Pd-H system hydride formation is possible for elastically deforming Pd. On the contrary, this is not possible in the thin film Nb-H system, which only allows phase separation when plastic deformations occur. This is linked to the lower stresses due to plastic deformations.
- The numerical simulations confirm the absence of hydride formation for purely elastic Nb-H thin films.
- The numerical simulations reproduce the analytical considerations regarding the coherency strain energy barrier of elasto-plastic Nb-H films and the resulting critical concentration of the α–phase during hydrogen loading with a homogeneous boundary condition, c.f. Fig. 4.9. In accordance with the theory of open coherent systems, in the model with homogeneous surface chemical potential the film entirely transforms into the hydride phase, once the elastic energy barrier is surpassed.
- The model with locally fluctuating surface chemical potential can be used to investigate coexistence states of α- and hydride-phase in

open systems at a thermodynamic equilibrium, i.e. at a homogeneous chemical potential below the global elastic barrier at which the entire film transforms into the hydride-phase. Coupled stress and concentration gradients result at phase interfaces. Hence, the local concentrations at phase interfaces differ significantly from the analytical predictions of Sec. 4.4, where no interface between α- and hydride-phase was considered, with increased concentration in the α-phase and reduced hydrogen concentration in the hydride-phase. The gradients extend $5\,\mathrm{nm}$ into the single phase fields for the chosen simulation domain and parameters.

- The geometries of hydride precipitates at the surface of the film match experimental results of STM measurements on open systems, c.f. Fig. 4.12. However, the cylindrical growth mode of the precipitates from the film surface towards the substrate concluded in Nörthemann and Pundt (2008) is not reproduced by the model predictions. Supposedly, this is due to the assumed coherency of the film-substrate interface in our simulations, which differs from the experimentally observed relaxed interface of hydride-phase and substrate in the investigated Nb-H thin films.
- The height changes during hydrogen loading measured on open systems using STM are reproduced fairly well, even though the hydride growth modes in the simulation and in the experiments differ due to the different coherency states of the film-substrate interface. However, again, due to the assumed coherency of the interface, numerical values are about $0.4\,\mathrm{nm}$ smaller compared to the experimental values, as the simulated precipitates do not grow all the way to the substrate.
- The results gained for the model system of adhered Nb-H thin films in the present work can be transferred to the thermodynamics of other intercalating systems with constraint conditions.

Chapter 5

Water diffusion in Polyamide 6[1]

5.1 Introduction

In Kehrer et al. (2023), PA 6 specimens with a length $l = 83\,\mathrm{mm}$, a width $w = 10\,\mathrm{mm}$ and a thickness $t = 2\,\mathrm{mm}$ were water jet cut from injection molded plates. Directly after molding, the specimens are typically in a dry-as-molded (DAM) state and only take up water due to environmental conditions. As the DAM state was not known, the specimens were stored first in a vacuum oven and afterwards in a desiccator to ensure a DAM state. Before relaxation testing, two PA 6 specimens were preconditioned to ATM-23/50, i.e. at a temperature $\theta = 23°\mathrm{C}$ and a relative humidity of $\phi = 50\,\mathrm{RH\%}$, which leads to a mass uptake of $2.5 - 3$ wt.% (Vlasveld et al., 2005). This was achieved by placing them in a climatic chamber with an accelerated preconditioning program for seven days. Multiple weighing confirmed an equilibrium moisture content that did not change in the following days.

The two specimens were tested in a static relaxation experiment. To this end, the specimens were placed in the testing chamber of a GABO Explexor® $500\,\mathrm{N}$ and allowed to settle for one hour. Subsequently, a constant strain $\varepsilon_0 = 0.1\,\%$ was applied and held constant for six hours.

---

[1] Chapter 5 is based on sections 1 - 4 of the publication "Modeling and FE simulation of coupled water diffusion and viscoelasticity in relaxation tests of polyamide 6" (Dyck et al. (2024c)).

The testing conditions differed, as one specimen was placed in an environmental chamber with humidity control (HC) at $\phi = 50\,\mathrm{RH\%}$, while the other was tested in a chamber without HC at $\phi \approx 35\,\mathrm{RH\%}$. The unusual relaxation behavior is observed when the relaxation modulus $R(t)$, which connects the applied constant strain ε_0 to the stress via $\sigma(t) = R(t)\varepsilon_0$, is depicted over time for a duration of six hours, c.f. Fig. 5.1. The relaxation modulus for the specimen tested with HC decreases with increasing time as expected, c.f. Sharma et al. (2020). The specimen tested without HC, however, shows an increasing relaxation modulus over time which is linked to drying of the specimen due to the deviation in ambient humidity level compared to the specimen's humidity content (Kehrer et al., 2023). The drying process leads to a contraction of the specimen, which is prohibited by the constant applied strain ε_0. Thus the relaxation modulus $R(t)$ increases. Multiple weighing of the two samples confirmed the suspected drying as the specimen tested with HC did not change it's mass considerably, whereas the specimen tested without HC lost $1.115\,\%$ of it's mass relative to it's initial mass, c.f. Tab. 5 in Kehrer et al. (2023).

Clearly, there is a need to consider these observations in chemo-mechanically coupled models in order to predict the diffusion-deformation behavior of PA 6 in varying operating conditions. Numerous studies have been conducted to this end. An excellent review is given in Venoor et al. (2021). In the context of coupled chemo-mechanical modeling approaches, we want to briefly mention models considering non-constant diffusion coefficients, such as the models proposed in Sharma et al. (2020), Sambale et al. (2021b) and Wetzel et al. (2023), changing elastic or viscoelastic properties, c.f. Sharma et al. (2020), Sharma and Diebels (2021) and Sambale et al. (2021a) and a varying glass transition temperature (Broudin et al., 2015a). However, to the best knowledge of the authors, so far no model has been proposed to predict the experimentally observed increase in $R(t)$ during a relaxation experiment due to drying of PA 6. In order to bridge this gap, the goal of this work is the derivation and application of a chemo-mechanical continuum model that couples water diffusion in PA 6 to viscoelastic deformations. The derivation includes a detailed discussion of the balance equations and the constitutive theory which considers both chemical and mechanical contributions to the free energy. The chemical part relies on the Flory-Huggins model (Flory, 1942; Huggins, 1942) for enthalpy and entropy of mixing, while the mechanical part introduces viscoelastic strains (Sharma et al., 2020). As the previously published approaches mentioned above require cumbersome experimental identification of each dependency on water concentration and result in large numbers of material parameters, our model relies on constant parameters which significantly simplifies the presentation, implementation and application of the model equations. However, we clearly outline limitations of our model. We apply the model to study drying of PA 6 specimens in an uncoupled diffusion simulation and

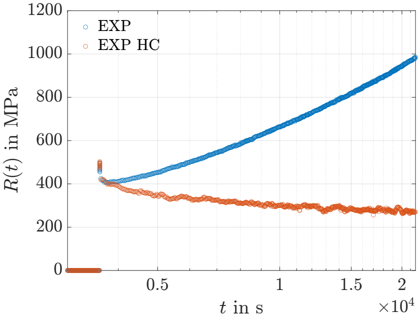

Figure 5.1: Relaxation modulus over time for two relaxation experiments conducted on PA 6 at 80° C. Both specimens were conditioned at a humidity level of $\phi = 50\,\%\mathrm{RH}$ at 80°C. One specimen was tested with humidity control (HC) at $\phi = 50\,\%\mathrm{RH}$, while the other specimen was tested without HC and the ambient humidity level was $\phi \approx 35\,\%\mathrm{RH}$. In the first hour of the experiment, both specimens are allowed to settle at $\varepsilon_0 = 0\,\%$, such that the temperature reaches an equilibrium. Subsequently, the strain is applied and held constant for 6 h. Figure based on Figure 1 from Dyck et al. (2024c).

subsequently in a chemo-mechanically coupled simulation of relaxation experiments.

This chapter is structured as follows: In Section 5.2 the theoretical framework of the model is presented, introducing balance laws and the constitutive theory. In Section 5.3, a Finite-Element implementation of the derived governing equations is presented and applied to predict both the drying of PA 6 specimens without mechanical deformation as well as an increasing relaxation modulus due to drying. Concluding remarks and an outlook are given in Section 5.4.

5.2 Theory

5.2.1 Basic assumptions

In this section, we present the governing balance equations and the constitutive theory, which we subsequently solve using Finite-Elements in order to model the diffusion of water in polyamide. Two components have to be considered, polyamide and water. As outlined in Chapter 2, we rely on a reduced set of governing equations, namely the concentration balance of the diffusing water and the balance of linear momentum in PA 6. For the constitutive theory we rely on a balance of internal energy of the mixture as well as an entropy balance of the mixture. As the maximum uptake of water in PA 6 is below 10 wt.%, we assume that contributions of water concentration to the mixture behavior are limited to a flux of internal energy as discussed in Chapter 2. The mixture balance of entropy relies on the Clausius-Duhem assumption for entropy production and flux (Coleman and Gurtin, 1967) and no further contributions from the diffusing water are introduced. The constitutive theory follows from a single free energy for the mixture, instead of two separate ones for each component.

As outlined in the introduction, the goal of this chapter is a comprehensive presentation of the model. To this end, all further assumptions underlying the constitutive theory are summarized below. These assumptions allow us to present a relatively simple model, that relies on few material parameters and no extra experimental work. A discussion and comparison to previous works of these assumptions is given at the end ob this section. The assumptions are:

- Isotropic material behavior.
- Constant material parameters with respect to water concentration.
- Absence of chemical reactions between water molecules and the PA 6 chains. As reactions are excluded, the model could also be called diffuso-mechanical.
- Constant mass density of PA 6 denoted by ρ.
- Negligence of inertia effects due to the time scale of water diffusion processes.
- Absence of volume forces.
- Purely volumetric, reversible swelling strain, being linear in the difference between current water concentration and a reference concentration (Sharma et al., 2020; Sambale et al., 2021a).
- A deviatoric linear viscoelastic model and an elastic behavior in volumetric deformations to describe the mechanical material behavior of PA 6 (Sharma et al., 2020).
- Isothermal conditions, such that parameter dependencies on temperature are discarded. In addition, heat-storage contributions to the free energy density are discarded.
- Applicability of the Flory-Huggins model (Flory, 1942; Huggins, 1942) for entropy and enthalpy of mixing to describe the chemical part of the free energy density.
- Negligence of the semi-crystalline structure of PA 6.

5.2.2 Description of the water content

As no separate continuum is introduced for the diffusing water, a definition of water content at any material point within PA 6 is necessary. This allows us to discuss the influence of water, e.g. due to swelling, on PA 6. Various works found different ways to approach this topic which will be briefly summarized here. The goal is to allow the reader to compare differing approaches to each other. A straightforward way to express water content is by using the partial density ρ_{w} of water (c.f. Eq. (2.15)), relating the infinitesimal mass of water $\mathrm{d}m_{\mathrm{w}}$ at a material point to the infinitesimal volume element $\mathrm{d}V = \mathrm{d}V_{\mathrm{w}} + \mathrm{d}V_{\mathrm{p,dry}}$. The dimensionless concentration, or mass fraction, is (c.f. Eq. (2.17))

$$c = \frac{\rho_{\mathrm{w}}}{\rho_{\mathrm{p,dry}}}, \tag{5.1}$$

where $\rho_{\mathrm{p,dry}}$ is the mass density of dry PA 6. This holds, as we assume the total mass of the mixture to be dominated by PA 6. In a homogeneous system this results in the integral mass fraction $c = m_{\mathrm{w}}/m_{\mathrm{p,dry}}$ (Venoor et al., 2021). For increasing water content, c increases up to a maximum concentration c_{max}, which denotes the maximum amount of water, that can be taken up by PA 6. Experiments indicate, that this maximum is at roughly $c_{\mathrm{max}} = 9\%$, almost independent of temperature (Sharma et al., 2020; Sambale et al., 2021a). Based on this observation, a normalized concentration or occupancy $\tilde{c}$ is frequently introduced by

$$\tilde{c} = \frac{c}{c_{\mathrm{max}}} \in [0, 1]\,. \tag{5.2}$$

Another approach to quantify water content in PA 6 is the polymer volume fraction φ, expressed as the ratio of an infinitesimal dry polymer volume element $\mathrm{d}V_{\mathrm{p,dry}}$ with respect to the infinitesimal total volume element $\mathrm{d}V$, given by (Chester and Anand, 2011)

$$\varphi = \frac{\mathrm{d}V_{\mathrm{p,dry}}}{\mathrm{d}V_{\mathrm{w}} + \mathrm{d}V_{\mathrm{p,dry}}}. \tag{5.3}$$

A fourth way of quantifying water content is the concentration of water in number of molecules of water per volume of dry PA 6 (Chester and Anand, 2011). We slightly change the notation introduced in Chapter 2 here and express the concentration in moles per volume as ϑ. To this end, we introduce ϑ_{max} as the maximum number of water particles per volume of PA 6 via

$$\vartheta_{\mathrm{max}} = \frac{\rho_{\mathrm{p,dry}} c_{\mathrm{max}}}{M_{\mathrm{w}}}, \tag{5.4}$$

where M_{w} in $\mathrm{kg/mol}$ is the molar mass of water. We want to point out, that both c_{max} and ϑ_{max} are material parameters, that describe the maximum amount of water, that PA 6 can take up, where the former specifies the maximum infinitesimal mass fraction, while the latter describes the maximum number of moles per volume. Based on ϑ_{max}, a relation between ϑ, c and $\tilde{c}$ can be computed according to

$$\vartheta = \frac{\vartheta_{\mathrm{max}}}{c_{\mathrm{max}}} c = \vartheta_{\mathrm{max}} \tilde{c}. \tag{5.5}$$

We conclude this short summary by relating φ with ϑ. We need to consider the volumetric expansion of polyamide due to the presence of water molecules. To this end, the volumetric expansion coefficient of water in polyamide, Ω, needs to be introduced, further outlined below. This implies that the infinitesimal volume of water at a material point can be expressed as $\mathrm{d}V_{\mathrm{w}} = \Omega\vartheta \mathrm{d}V_{\mathrm{p,dry}}$. Building upon this coefficient, the relation is (Chester and Anand, 2011)

$$\varphi = \frac{1}{1 + \frac{\mathrm{d}V_{\mathrm{w}}}{\mathrm{d}V_{\mathrm{p,dry}}}} = \frac{1}{1 + \Omega\vartheta}. \tag{5.6}$$

In the following, we will make use of the definition for the concentration c and occupancy $\tilde{c}$. However, using the relations summarized above, readers can express quantities as functions of ϑ or φ.

5.2.3 Balance equations

We start by formulating a balance equation for the diffusion of water, expressed for the normalized water concentration $\tilde{c}$, see Eq. (5.2). The concentration can change due to a flux of water $\boldsymbol{j}$, into or out of PA 6. In its local form, the mass balance reads (c.f. Eq. (2.21) (1))

$$\dot{\vartheta} = \vartheta_{\max}\dot{\tilde{c}} = -\mathrm{div}\left(\boldsymbol{j}\right). \tag{5.7}$$

The local balance of linear momentum for the mixture is

$$\mathrm{div}\left(\boldsymbol{\sigma}\right) = \boldsymbol{0}, \tag{5.8}$$

where $\boldsymbol{\sigma}$ is the Cauchy stress tensor in PA 6. As noted in Sec. 2.4, the balance of internal energy for the mixture considers, additionally to the heat flux, the change due to water flux across the system boundary by $\mu\boldsymbol{j}\cdot\boldsymbol{n}$, where μ is the chemical potential of water and $\boldsymbol{n}$ the outer normal of PA 6. The local balance of internal energy is then (Gurtin and Vargas, 1971; Gurtin et al., 2010)

$$\dot{e} = \boldsymbol{\sigma}\cdot\dot{\boldsymbol{\varepsilon}} - \mu\mathrm{div}\left(\boldsymbol{j}\right) - \mathrm{grad}\left(\mu\right)\cdot\boldsymbol{j} - \mathrm{div}\left(\boldsymbol{q}_\theta\right) + \omega, \tag{5.9}$$

where $-\mathrm{div}\left(\boldsymbol{q}_\theta\right) + \omega$ denotes changes in internal energy due to heat flux $\boldsymbol{q}_\theta$ and heat source densities ω. The non-standard contribution to the flux in internal energy due to water flux is given by $-\mathrm{div}\left(\mu\boldsymbol{j}\right) = -\mu\mathrm{div}\left(\boldsymbol{j}\right) - \mathrm{grad}\left(\mu\right)\cdot\boldsymbol{j}$, c.f. Eq. (2.25) and Eq. (3.4). Inserting the mass balance of the diffusing water from Eq. (5.7) yields

$$\dot{e} = \boldsymbol{\sigma}\cdot\dot{\boldsymbol{\varepsilon}} + \mu\vartheta_{\max}\dot{\tilde{c}} - \mathrm{grad}\left(\mu\right)\cdot\boldsymbol{j} - \mathrm{div}\left(\boldsymbol{q}_\theta\right) + \omega. \tag{5.10}$$

Finally, to complete the necessary balance equations, we introduce the entropy balance and the assumption of a non-negative entropy production in it's local form for constant temperature θ as

$$\dot{\eta} \geq -\mathrm{div}\left(\frac{\boldsymbol{q}_\theta}{\theta}\right) + \frac{\omega}{\theta}, \tag{5.11}$$

where, as introduced in Chapter 2, η is the entropy density, $\boldsymbol{q}_\theta/\theta$ the entropy flux and ω/θ entropy supply density due to heat sources. We want to point out, that the specific form of the entropy flux $\boldsymbol{q}_\theta/\theta$, which neglects a contribution of the diffusing water, is a simplifying assumption. This assumption was introduced in Gurtin and Vargas (1971) and is commonly used in chemo-mechanically coupled theories, see, e.g., Chester and Anand (2011) and Di Leo and Anand (2013).

5.2.4 Thermodynamically consistent constitutive equations

To arrive at a closed set of governing equations, we rely on the Coleman-Noll procedure (Coleman and Gurtin, 1967) to derive a thermodynamically consistent material theory. Therefore, we introduce the free energy density via a Legendre transformation

$$\psi = e - \theta\eta. \tag{5.12}$$

By inserting Eq. (5.12) into Eq. (5.11) and eliminating the heat source density ω by means of Eq. (5.10), we arrive at

$$\left(\dot{\psi} + \eta\dot{\theta}\right) - \boldsymbol{\sigma} \cdot \dot{\boldsymbol{\varepsilon}} + \frac{\boldsymbol{q}_\theta \cdot \mathrm{grad}\,(\theta)}{\theta} - \mu\vartheta_{\mathrm{max}}\dot{\tilde{c}} + \mathrm{grad}\,(\mu) \cdot \boldsymbol{j} \leq 0. \tag{5.13}$$

In our theory, the independent variables are the set $\Lambda = (\boldsymbol{\varepsilon}, \theta, \tilde{c}, \underline{\alpha})$, where $\underline{\alpha}$ is a tuple of internal variables, that later on will be used to model the viscoelastic deformation of PA 6. Based on the equipresence argument, we insert $\psi = \psi\left(\Lambda\right)$ into Eq. (5.13) to arrive at

$$\begin{gathered}\left(\frac{\partial\psi}{\partial\boldsymbol{\varepsilon}} - \boldsymbol{\sigma}\right)\cdot\dot{\boldsymbol{\varepsilon}} + \left(\frac{\partial\psi}{\partial\theta} + \eta\right)\dot{\theta} + \left(\frac{\partial\psi}{\partial\tilde{c}} - \mu\vartheta_{\max}\right)\dot{\tilde{c}} + \\ \frac{\partial\psi}{\partial\underline{\alpha}}\cdot\underline{\dot{\alpha}} + \operatorname{grad}\left(\mu\right)\cdot\boldsymbol{j} + \frac{1}{\theta}\boldsymbol{q}_{\theta}\cdot\operatorname{grad}\left(\theta\right) \leq 0.\end{gathered} \tag{5.14}$$

This inequality has to hold for all thermodynamic processes Λ. We start by considering reversible processes and thus conclude, that the the potential relations

$$\boldsymbol{\sigma} = \frac{\partial\psi}{\partial\boldsymbol{\varepsilon}}, \quad \eta = -\frac{\partial\psi}{\partial\theta}, \quad \mu = \frac{1}{\vartheta_{\max}}\frac{\partial\psi}{\partial\tilde{c}} \tag{5.15}$$

hold, for both reversible and irreversible processes. The remaining dissipation inequality is

$$\frac{\partial\psi}{\partial\underline{\alpha}}\cdot\underline{\dot{\alpha}} + \operatorname{grad}\left(\mu\right)\cdot\boldsymbol{j} + \frac{1}{\theta}\boldsymbol{q}_{\theta}\cdot\operatorname{grad}\left(\theta\right) \leq 0. \tag{5.16}$$

The dissipation inequality implies restrictions for the choice of heat flux $\boldsymbol{q}_{\theta}$, water flux $\boldsymbol{j}$ and the evolution of internal variables $\underline{\dot{\alpha}}$. In addition, we conclude from Eq. (5.15) that we need to specify a free energy density that relates the constitutive quantities $\boldsymbol{\sigma}, \mu$ and η to the process parameters $\boldsymbol{\varepsilon}, \theta, \tilde{c}$ and $\underline{\alpha}$. Here we formulate a single free energy density for the continuum of polyamide and water, which is additively split in an elastic and a chemical part via

$$\psi(\Lambda) = \psi_{\mathrm{e}}\left(\boldsymbol{\varepsilon}_{\mathrm{e}}\right) + \psi_{\mathrm{c}}(\theta, \tilde{c}), \tag{5.17}$$

where the elastic part ψ_{e} depends on the elastic strains $\boldsymbol{\varepsilon}_{\mathrm{e}}$, which are a function of $\boldsymbol{\varepsilon}, \tilde{c}$ and $\underline{\alpha}$, while the chemical part ψ_{c} solely depends on θ and $\tilde{c}$.

The chemical part of the free energy density ψ_{c} follows from considering changes in the free enthalpy and the entropy due to mixing of water and

PA 6. At this stage we want to mention, that typically this relation is used to describe a change in Gibb's energy density due to mixing, i.e., g_c. However, as pointed out in Doi (1996), the chemical part ψ_c of the free energy and the Gibb's energy g_c coincide in our approach, i.e. $\psi_\mathrm{c} = g_\mathrm{c}$, as the mechanical part is considered separately in ψ_e.

Commonly in chemo-mechanics, a highly idealized model is used that allows to express the entropy of mixing for ideal gases and assumes a vanishing enthalpy of mixing. This approach has been successfully used to model hydrogen diffusion in metal lattices or Lithium diffusion in silicon anodes, c.f. Di Leo and Anand (2013) and Di Leo et al. (2015). However, this highly idealized model is not valid for the mixture of PA 6 and water, considered in this work, as neither water molecules nor PA 6 behave like ideal gases (Chester and Anand, 2011; Wilmers and Bargmann, 2015).

Instead, to describe the chemical contribution to the free energy, the model of Flory and Huggins (Flory, 1942; Huggins, 1942) is used in this work, which is based on a lattice model as depicted in Fig. 5.2 a). The polymer consists of polymer molecules, which occupy connected lattice points, whereas the rest of the lattice is occupied by water molecules. Flory and Huggins introduced a parameter χ (later called Flory-Huggins parameter) that models interactions of the long polymer molecules and the small water molecules and introduces a non vanishing enthalpy of mixing. The larger the Flory-Huggins parameter, the stronger the interaction between both molecules, the larger the enthalpy of mixing. The Flory-Huggins entropy of mixing is in close analogy to the entropy of mixing of ideal gases, but is a function of the partial volume instead of the concentration. The change in free energy is, based on the Flory Huggins model (Doi, 1996; Chester and Anand, 2011),

$$\psi_\mathrm{c} = \mu_0 \vartheta_\mathrm{max} \tilde{c} + R\theta\vartheta_\mathrm{max}\tilde{c} \left(\ln \left(\frac{\Omega \vartheta_\mathrm{max} \tilde{c}}{1 + \Omega \vartheta_\mathrm{max} \tilde{c}} \right) + \frac{\chi}{1 + \Omega \vartheta_\mathrm{max} \tilde{c}} \right) . \tag{5.18}$$

To specify ψ_e, chemical and viscoelastic strains are introduced. Chemical strains $\boldsymbol{\varepsilon}_\mathrm{c}$ are volumetric (Chester and Anand, 2011)

$$\boldsymbol{\varepsilon}_\mathrm{c} = \alpha_\mathrm{c} \Delta \tilde{c} \boldsymbol{I}, \tag{5.19}$$

where $3\alpha_\mathrm{c} = \Omega \vartheta_\mathrm{max}$ is a dimensionless swelling coefficient (Sharma et al., 2020; Sambale et al., 2021b) and $\Delta\tilde{c}$ is the difference of the current concentration to a normalized reference concentration $\tilde{c}_0$, for which no swelling occurs. Viscoelastic strains $\boldsymbol{\varepsilon}_{\mathrm{v},\alpha}$ are introduced as internal variables $\underline{\alpha}$. A standard linear viscoelastic Maxwell element model is used with N_MW Maxwell elements in parallel to an equilibrium stiffness $\mathbb{C}_0$, c.f. Fig. 5.2 b). To this end, the viscosity tensor $\mathbb{V}_\alpha$ for Maxwell element α as well as it's inverse, the fluidity tensor $\mathbb{F}_\alpha$, are introduced by

$$\mathbb{V}_\alpha = \tau_\alpha \mathbb{C}_\alpha, \quad \mathbb{F}_\alpha = \frac{1}{\tau_\alpha} \mathbb{C}_\alpha^{-1}, \tag{5.20}$$

where $\mathbb{C}_\alpha = 2G_\alpha \mathbb{P}_2$ is the stiffness of each element, G_α the respective shear modulus and $\mathbb{P}_2$ the projector on symmetric deviatoric tensors of rank 2. This implies, that all viscous strains are volume preserving. For each Maxwell element, the relaxation time and the inverse of the stiffness are denoted by τ_α and $\mathbb{C}_\alpha^{-1}$ respectively (Wicht et al., 2021). The evolution of the viscous strains follows from

$$\dot{\boldsymbol{\varepsilon}}_{\mathrm{v},\alpha} = \mathbb{F}_\alpha \left[\boldsymbol{\sigma}_{\mathrm{v},\alpha}\right]. \tag{5.21}$$

Building upon the chemical strain and the viscous strains in each Maxwell element, an elastic strain is retrieved for both the equilibrium stiffness and each Maxwell element by

$$\boldsymbol{\varepsilon}_{\mathrm{e},0} = \boldsymbol{\varepsilon} - \boldsymbol{\varepsilon}_\mathrm{c}, \quad \boldsymbol{\varepsilon}_{\mathrm{e},\alpha} = \boldsymbol{\varepsilon} - \boldsymbol{\varepsilon}_{\mathrm{v},\alpha}. \tag{5.22}$$

The stress in each Maxwell element can now be given by

$$\boldsymbol{\sigma}_{\mathrm{v},\alpha} = \mathbb{C}_\alpha \left[\boldsymbol{\varepsilon} - \boldsymbol{\varepsilon}_{\mathrm{v},\alpha}\right]. \tag{5.23}$$

Based on these quantities, the elastic part of the free energy density is considered to be a quadratic function of the elastic strain and expressed as (Wicht et al., 2021)

$$\psi_{\mathrm{e}} = \frac{1}{2}(\boldsymbol{\varepsilon} - \boldsymbol{\varepsilon}_{\mathrm{c}}) \cdot \mathbb{C}_0 \left[\boldsymbol{\varepsilon} - \boldsymbol{\varepsilon}_{\mathrm{c}}\right] + \frac{1}{2} \sum_{\alpha=1}^{N_{\mathrm{MW}}} (\boldsymbol{\varepsilon} - \boldsymbol{\varepsilon}_{\mathrm{v},\alpha}) \cdot \mathbb{C}_\alpha \left[\boldsymbol{\varepsilon} - \boldsymbol{\varepsilon}_{\mathrm{v},\alpha}\right]. \tag{5.24}$$

Here, $\mathbb{C}_0 = 3K_0\mathbb{P}_1 + 2G_0\mathbb{P}_2$ is the isotropic equilibrium stiffness with compression modulus K_0 and shear modulus G_0. $\mathbb{P}_1$ is the projector onto spherical tensors of rank 2. Based on the potential relations in Eq. (5.15), the free energy density given by Eqs. (5.18) and (5.24) results

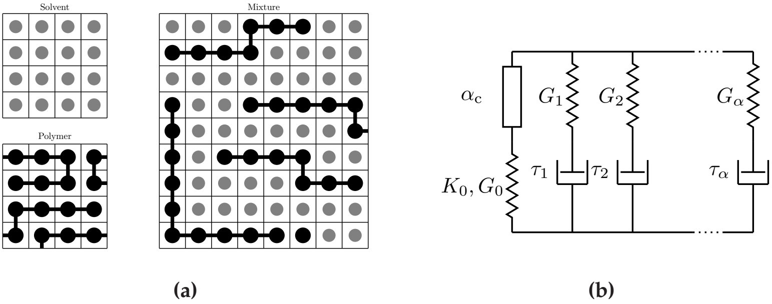

(a) **(b)**

Figure 5.2: a) Schematic of the Flory-Huggins mean-field model to predict both enthalpy and entropy of mixing of a polymer with a solvent. b) Schematic of the Maxwell element model used to describe the viscoelastic behavior of PA 6. Next to N_{ME} elements a reference stiffness in series with an α_{c}-element, representing the isochoric swelling of PA 6, is attached in parallel. Figure based on Figure 2 from Dyck et al. (2024c).

in

$$\boldsymbol{\sigma} = \mathbb{C}_0 \left[\boldsymbol{\varepsilon} - \alpha_{\mathrm{c}} \Delta\tilde{c}\boldsymbol{I}\right] + \sum_{\alpha}^{\mathrm{N_{MW}}} \mathbb{C}_\alpha \left[\boldsymbol{\varepsilon} - \boldsymbol{\varepsilon}_{\mathrm{v},\alpha}\right]$$

$$\mu = \mu_0 + R\theta \left(\ln\left(\frac{3\alpha_{\mathrm{c}}\tilde{c}}{1+3\alpha_{\mathrm{c}}\tilde{c}}\right) + \frac{1}{1+3\alpha_{\mathrm{c}}\tilde{c}} + \frac{\chi}{(1+3\alpha_{\mathrm{c}}\tilde{c})^2}\right) - \frac{\alpha_{\mathrm{c}}}{\vartheta_{\max}} \mathrm{tr}(\boldsymbol{\sigma}). \tag{5.25}$$

To conclude the constitutive theory, we introduce the water flux which is proportional to the gradient in the chemical potential, with a proportionality factor $m(\tilde{c}, \theta)$, that is interpreted as the mobility of water in the polymer network. This is summarized as

$$\boldsymbol{j} = -m(\tilde{c}, \theta)\mathrm{grad}\,(\mu)\,, \tag{5.26}$$

with a scalar mobility $m(\tilde{c}, \theta)$ being linear in $\tilde{c}$. For increasing $\tilde{c}$, experiments have shown that diffusion occurs at a faster rate (Sharma et al., 2020; Sambale et al., 2021b). In Chester and Anand (2011), a proposal was made to capture this behavior by considering a change in mobility due to an increase of water molecules with a dimensionless function $\gamma\,(\tilde{c})$. We follow this approach such that the mobility is given by

$$m = \frac{D\vartheta_{\max}}{R\theta}\gamma\,(\tilde{c})\,, \quad \text{where} \quad \gamma\,(\tilde{c}) = 1 + \gamma_{\mathrm{S}}\tilde{c} \tag{5.27}$$

and the diffusion coefficient is D. This ansatz fulfills the dissipation inequality (5.16) and leads to an increasing mobility for increasing $\tilde{c}$. For maximum water content, the mobility is $1 + \gamma_{\mathrm{S}}$ times its dry value.

5.2.5 Closed set of governing equations

As noted in Chapter 3, for the implementation of the coupled set of governing equations it is advantageous to change the independent chemical variable from concentration to chemical potential. This has several reasons:

- Solving the diffusion equation for $\tilde{c}$ requires the solution of a PDE with a bounded solution variable as $c \geq 0$. Enforcing this inequality constraint is either numerically costly (Lu et al., 2013) or impossible in commercial FEM packages.
- The flux term in the diffusion equations is linear in the gradient of the chemical potential, itself being a function of the displacement gradient. This necessitates to approximate gradients of mechanical stresses on FEM meshes, which makes solutions susceptible to mesh sensitivity and less generally applicable. In addition, this results in the requirement of $C2$-continuous functions to interpolate the displacement field $\boldsymbol{u}$ as second order gradients have to be computed.
- An open system, i.e. a system that is exposed to an atmosphere with a given ambient humidity ϕ, can not readily be simulated in a concentration based setting. This is due to the fact, that chemical potential and concentration are linked through the hydrostatic stress.

These reasons motivate a change in independent variables from concentration to chemical potential. To achieve this, we differentiate Eq. (5.25) (2) in time and use the result to express the rate of change in occupancy as a function of the rate of change in chemical potential. Introducing some abbreviations

$$\begin{aligned}
k_0 &= \ln\left(\frac{3\alpha_{\mathrm{c}}\tilde{c}}{1+3\alpha_{\mathrm{c}}\tilde{c}}\right) + \frac{1}{1+3\alpha_{\mathrm{c}}\tilde{c}} + \frac{\chi}{(1+3\alpha_{\mathrm{c}}\tilde{c})^2}, \\
k_1 &= \frac{\partial k_0}{\partial \tilde{c}} = \frac{1-6\alpha_{\mathrm{c}}(\chi-1/2)\tilde{c}}{(3\alpha_{\mathrm{c}}\tilde{c}+1)^3\tilde{c}}, \\
k_2 &= R\theta k_1 + \frac{\alpha_{\mathrm{c}}^2 \mathrm{tr}\left(\mathbb{C}_0\left[\boldsymbol{I}\right]\right)}{\vartheta_{\max}},
\end{aligned} \tag{5.28}$$

allows us to find

$$\dot{\tilde{c}} = \frac{\dot{\mu} + \alpha_{\mathrm{c}} \mathrm{tr}\left(\mathbb{C}_0\left[\dot{\boldsymbol{\varepsilon}}\right]\right)/\vartheta_{\max}}{k_2}. \tag{5.29}$$

Combining the constitutive laws outlined in the previous subsection, the balance of linear momentum, Eq. (5.8), and inserting Eq. (5.29) in Eq. (5.7) allows us to arrive at the closed set of governing equations

$$\begin{aligned} \mathbf{0} &= \operatorname{div}\left(\boldsymbol{\sigma}(\boldsymbol{\varepsilon}, \tilde{c}, \boldsymbol{\varepsilon}_{\mathrm{v},\alpha})\right), \\ \frac{\vartheta_{\max}}{k_2}\dot{\mu} &= \operatorname{div}\left(m \operatorname{grad}\left(\mu\right)\right) - \frac{\alpha_{\mathrm{c}} \mathrm{tr}\left(\mathbb{C}_0\left[\dot{\boldsymbol{\varepsilon}}\right]\right)}{k_2}, \end{aligned} \tag{5.30}$$

where the constitutive equations for $\boldsymbol{\sigma}$ and m are defined in Eq. (5.25) (1) and Eq. (5.27) and k_2 is given in Eq. (5.28).

To complete the model, both initial and boundary values have to be specified. We denote initial conditions by a hat and boundary conditions by a bar, i.e. the initial chemical potential is $\hat{\mu}$ and boundary displacements are given by $\bar{\boldsymbol{u}}$. Both initial and boundary chemical potentials $\hat{\mu}$ and $\bar{\mu}$, when PA 6 is exposed to an atmosphere with a given relative humidity ϕ, are computed by (Wilmers and Bargmann, 2015)

$$\mu_{0,\mathrm{vapor}} + R\theta \ln \phi = \begin{cases} \hat{\mu}, & t = 0 \\ \bar{\mu}, & t > 0, \end{cases} \tag{5.31}$$

where $\mu_{0,\mathrm{vapor}}$ is the reference chemical potential of water in air. A short summary of the nomenclature for initial and boundary conditions used in all simulations of the subsequent Section 5.3 is given in Tab. 5.1. As the concentration is no longer a degree of freedom, no boundary or initial concentration is specified when the model is used. However, an initial concentration $\hat{c}$ in wt.% follows from evaluating the initial displacements $\hat{\boldsymbol{u}}$ and the initial chemical potential $\hat{\mu}$ by means of Eq. (5.25) (2). The same holds for concentrations $\bar{c}$ at the boundary, which follow for known

boundary displacements $\bar{\boldsymbol{u}}$ and boundary chemical potential $\bar{\mu}$.
In order to study the coupled diffusion deformation behavior of PA 6, using the coupled governing equations outlined in this subsection, we rely on the commercial Finite-Element solver ABAQUS. To implement the derived model equations in ABAQUS, the heat-transfer analogy outlined in Chapter 3 is used.

	Symbol	Computed based on
Initial displacement	$\hat{\boldsymbol{u}}$	
Initial chemical potential	$\hat{\mu}$	Eq. (5.31)
Boundary displacement	$\bar{\boldsymbol{u}}$	
Boundary chemical potential	$\bar{\mu}$	Eq. (5.31)

Table 5.1: Nomenclature for initial and boundary conditions. Table based on Table 1 from Dyck et al. (2024c).

5.2.6 Discussion of the model equations

Before identifying the model and implementing it in a commercial Finite-Element solver to study chemo-mechanically coupled deformation and drying processes in PA 6, we want to comment in the following on several of the assumptions that lead to the closed set of governing equations presented in Eq. (5.30). By this, the newly derived model can be compared with existing models to identify possible extensions and limitations of the model can be more clearly identified.

Balance equations. By the specific form of the balance of entropy given in Eq. (5.11), we assume that mass transport does not contribute to entropy flux and supply, which is often done in chemo-mechanically coupled theories, c.f. Gurtin and Vargas (1971), Chester and Anand (2011) and Di Leo and Anand (2013). However, instead of introducing the contribution of water to the mixture behavior in the balance of internal energy in Eq. (5.9), we could also have introduced a non-standard entropy flux due to water flux, as, e.g., done in Johlitz and Lion (2013) and Sharma and Diebels (2021). However, both approaches lead to identical constitutive relations when thermodynamics are introduced, as noted in Gurtin and Vargas (1971), Johlitz and Lion (2013) and Johlitz (2015). Introducing the diffusing phases contribution in the balance of internal energy allows a clear interpretation of the chemical potential, as noted in Gurtin et al. (2010). Therefore, we prefer the version proposed in Gurtin and Vargas (1971).

Dependence on water concentration and temperature. As stated, many material parameters (such as glass transition temperature (Miri et al., 2009; Broudin et al., 2015a;b), stiffness (Sharma et al., 2020), Poisson's ratio (Sharma et al., 2020), diffusion constant (Vlasveld et al., 2005)) in PA 6 have been experimentally shown to be dependent on the moisture content, as well as temperature. However, we have neglected this in our model entirely, in order to arrive at a comparably simple model, still capturing the essence of the observed relaxation behavior, c.f. Fig. 5.1. As a side note we want to point out, that introducing non constant material parameters in the potential relations derived in Eq. (5.15) leads to an increasing complexity of the material laws. This can be studied by imagining the stiffness tensors of the equilibrium spring being a function of water concentration. When this dependency is introduced in the mechanical part of the free energy in Eq. (5.24) and the chemical potential is derived from it, a non-standard term being quadratic in the elastic strain is added to the chemical potential of water.

Isotropy of the constitutive laws All material laws are assumed to be isotropic within our work. However, this does not represent all experimental observations, as in injection molded PA 6 specimens, an anisotropy of both stiffness constants as well as extension parameters has been shown in Sambale et al. (2021a) and Wetzel et al. (2023).

Reaction term. In the mass balance introduced in Eq. (5.7), no production term is introduced. This limits the derived model to studying water uptake or loss from the medium surrounding PA 6, but does not allow for simulating chemical reactions between PA 6 and water. Introducing a production term between water molecules and PA 6 in Eq. (5.7) allows to study, e.g., ageing effects due to chemical reactions between both phases, such as in Johlitz and Lion (2013).

Extensions to the model. In the view of the authors, the presented model can be extended to consider anisotropic material, as, e.g., observed in Sambale et al. (2021b) and Wetzel et al. (2023), to large deformations (Chester and Anand, 2011) or nonlinear viscoelastic models (Zink et al., 2022), without reasonable effort.

Heat contribution. Neglecting heat-storage contributions to the total free energy density is inspired by numerous publications in the context of chemo-mechanical processes at constant temperature, see, e.g., Chester and Anand (2011), Di Leo and Anand (2013) and Wilmers and Bargmann (2015). However, considering non isothermal cases, e.g. along the lines of Di Leo and Anand (2013) and Chester and Anand (2011), can be considered a valuable extension of the theory.

5.3 Applications

5.3.1 Parameter identification

All mechanical and chemical material parameters of the model outlined above have to be identified in order to study water uptake or drying of PA 6 coupled to it’s deformation. All parameters used in subsequent simulations are summarized in Tab. 5.2 and Tab. 5.3. Due to the modeling

Symbol	Value	Unit	Source
D	5×10^{-6}	$\mathrm{mm^2/s}$	Vlasveld et al. (2005)
M_{w}	18.015	$\mathrm{g/mol}$	Greenwood and Earnshaw (1997)
$\rho_{\mathrm{p,dry}}$	1.13	$\mathrm{g/cm^3}$	Domininghaus (2012)
μ_0	0	$\mathrm{Nmm/mol}$	Chester and Anand (2011)
$\mu_{0,\mathrm{vapor}}$	0	$\mathrm{Nmm/mol}$	Chester and Anand (2011)
α_{c}	0.045		Sharma et al. (2020)
γ_{S}	3		Chester and Anand (2011)
$c_{\max}$	0.09		Vlasveld et al. (2005)
χ	1.64		this work

Table 5.2: Chemical material parameters used in all simulations of this work. Parameters taken from literature are indicated by the source, the rest are identified in this work. Table based on Table 2 from Dyck et al. (2024c).

Symbol	Value	Unit	Source
ν_0	0.4		Tschoegl et al. (2002)
E_0	256	MPa	this work
N_{MW}	5		this work
G_α	$[14.9, 11.4, 6.8, 24.5, 31.0]$	MPa	this work
τ_α	$\left[10^0, 10^1, 10^2, 10^3, 10^4\right]$	$1/\mathrm{s}$	this work

Table 5.3: Mechanical material parameters used in all simulations of this work. Parameters taken from literature are indicated by the source, the rest are identified in this work. Table based on Table 3 from Dyck et al. (2024c).

assumptions outlined above, most of the chemical parameters can be taken directly from literature. The only unknown chemical parameter is the Flory-Huggins parameter χ. To identify both χ and the mechanical parameters we rely on two sets of data. We use sorption curves of PA 6 exposed to an atmosphere with given relative humidity ϕ to determine χ. For the isotropic equilibrium stiffness $\mathbb{C}_0$ as well as Maxwell element parameters G_α and τ_α we use the experimental results of a relaxation test conducted under HC at 80° C, c.f. Fig. 5.1.

To identify the Flory-Huggins parameter χ, both the maximum concentration $c_{\max} = 0.09$ of water in PA 6 as well as the mass frac-

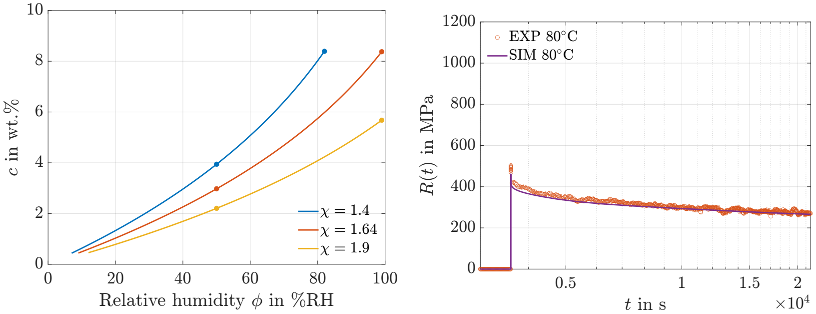

(a) **(b)**

Figure 5.3: a) Equilibrium water content c in $\mathrm{wt.\%}$ when PA 6 is exposed to an environment with humidity content ϕ for three Flory-Huggins parameters. At $\phi = 50\,\%\mathrm{RH}$ and ϕ_{max}, the model predictions are marked by a dot as these data points are used to identify the Flory-Huggins parameter χ as outlined in the text. b) Relaxation modulus over time for both an experimental and simulated result of a relaxation experiment conducted at 80° C under HC. Figure based on Figure 3 from Dyck et al. (2024c).

tion $c \in [2.5\,\mathrm{wt.\%}, 3\,\mathrm{wt.\%}]$ of water in PA 6 after conditioning in an atmosphere with $\phi = 50\,\%\mathrm{RH}$ are considered to be given (Vlasveld et al., 2005). We then determine χ in such a way, that our model reproduces the maximum concentration c_{max}. In addition, the mass fraction should result in a value from the interval $c \in [2.5\,\mathrm{wt.\%}, 3\,\mathrm{wt.\%}]$ obtained experimentally. To this end, we equate the boundary condition of the chemical potential, Eq. (5.31), with the chemical potential of water in PA 6, Eq. (5.25) (2), and neglect mechanical contributions. We vary χ and study both the water uptake at $\phi = 50\,\%\mathrm{RH}$, as well as $\phi \approx 100\,\%\mathrm{RH}$. The results are shown in Fig. 5.3 a), where the water uptake as a function of the relative humidity is depicted. Both the model prediction for $\phi = 50\,\%\mathrm{RH}$ and $\phi = 100\,\%\mathrm{RH}$ are depicted as dots. For $\chi = 1.64$, both $c(\phi = 50\,\%\mathrm{RH}) \approx 3\,\mathrm{wt.\%}$ as well as $c_{\mathrm{max}} \approx 9\,\mathrm{wt.\%}$ are predicted with satisfying accuracy. The shape of the sorption curve, i.e., the equilibrium water content plotted against the relative humidity as predicted by our model was investigated experimentally in, e.g., Vlasveld et al. (2005) and Broudin et al. (2015b). The curves determined published in these works qualitatively match the shape of our model curve.

The mechanical material parameters are the equilibrium compression and shear moduli K_0 and G_0 as well as the shear and relaxation moduli of the Maxwell elements G_α, τ_α. As no experimental evidence is at hand, Poisson's ratio ν_0 of PA 6 is chosen to be $\nu_0 = 0.4$ (Tschoegl et al., 2002). All other parameters are determined by fitting to the experimentally obtained relaxation curve under HC at $80°\mathrm{C}$ depicted in Fig. 5.3 b). This is achieved by means of a least square fit of a one-dimensional linear viscoelastic model to the experimental data. The number of Maxwell elements $N_{\mathrm{MW}} = 5$ and the relaxation times $\tau_\alpha \in \left[10^0, 10^1, 10^2, 10^3, 10^4\right]$ 1/s are previously fixed (Bradshaw and Brinson, 1997; Jalocha et al., 2015; Kehrer et al., 2023). The optimization allows us to identify the equilibrium elastic modulus E_0 as well as elastic moduli E_α for the Maxwell elements. Using $G_\alpha = E_\alpha/(2(1-\nu_0))$ all shear moduli of the Maxwell elements are determined. The result of the determined relaxation curve is depicted in Fig. 5.3 b), where the model prediction is compared to experimental results. As can be seen, the identified set of mechanical parameters allows us to capture the typical decrease in relaxation modulus $R(t)$.

Before we proceed to conduct Finite-Element simulations of diffusion and coupled diffusion-deformation processes, we comment on two material parameters summarized in Tab. 5.2 and Tab. 5.3.

Diffusion coefficient: An experimental investigation showed that the dependency of the diffusion coefficient of water in PA 6 strongly depends on temperature (Vlasveld et al., 2005). An explicit Arrhenius-type equation for this was proposed as

$$D = D_0 \exp\left(-\frac{E_{\mathrm{s}}}{k_{\mathrm{B}}\theta}\right), \tag{5.32}$$

where $E_\mathrm{s} = 0.49\,\mathrm{eV}$ is an activation energy and k_B the Boltzmann constant. The diffusion coefficient $D_{70^\circ\mathrm{C}} = 3 \times 10^{-6}\,\mathrm{mm}^2/\mathrm{s}$ was determined experimentally in Vlasveld et al. (2005). Using these measurements and Eq. (5.32), we determine a diffusion coefficient for water in PA 6 at $80^\circ\mathrm{C}$ as $D_{80^\circ\mathrm{C}} = 5 \times 10^{-6}\,\mathrm{mm}^2/\mathrm{s}$.

Expansion coefficient: In Sharma et al. (2020), Jia and Kagan (2001), Wetzel et al. (2023) and Sambale et al. (2021b) measurements were conducted to identify the swelling coefficient α_c leading to a volume change of PA 6 for increasing water content. To obtain the parameter, specimen are allowed to absorb the maximum amount of water and the change in length is measured. In the mentioned works, the swelling coefficient lies in the range $\alpha_\mathrm{c} \in [0.018, 0.05]$. This range is explained by differing processing conditions of specimens Wetzel et al. (2023), by differing volume to surface ratios (Sambale et al., 2021a) and by differing boundary conditions (Sharma et al., 2020). As no experiments were conducted in this study, we use a swelling factor of $\alpha_\mathrm{c} = 0.045$. We note that this choice is coupled to the choice of the Flory-Huggins parameter χ due to the fact that α_c also enters Eq. (5.25) (2). Thus, the choice of α_c and χ are, in our model, coupled in such a way that the water uptake experimentally observed in Vlasveld et al. (2005) is influenced by them.

5.3.2 Drying of preconditioned specimens

We first use the derived and identified model to study the drying of PA 6 specimens preconditioned to $c_0 = 3\,\mathrm{wt.\%}$ at an ambient relative humidity of $\phi = 50\,\%\mathrm{RH}$ and $\theta = 80^\circ\mathrm{C}$. We therefore expose specimens to a varying ambient humidity $\phi = [35, 25, 15]\,\%\mathrm{RH}$ for $7\,\mathrm{h}$, which corresponds to the total exposure time during the relaxation experiment depicted in Fig. 5.1. The specimen dimensions presented in Sec. 5.1 are used in the simulation. However, we want to point out, that Tab. 10 in Kehrer et al. (2023) documents a slight variation in specimen thickness for each specimen, which results from the injection molding process. We

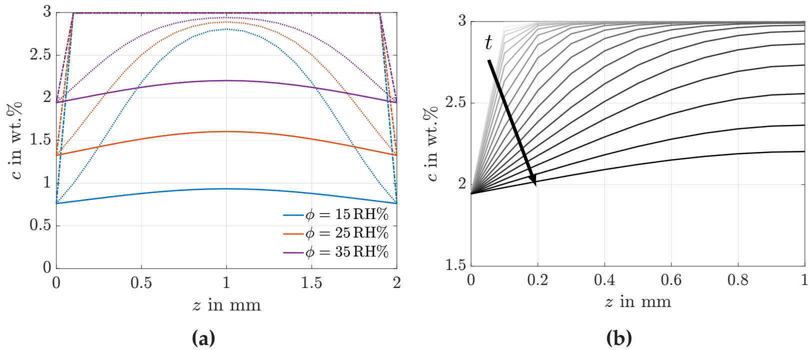

Figure 5.4: a) Water concentration c in wt.% along the thickness of three specimens for varying relative humidity ϕ at 80°C. All specimens are preconditioned to $c = 3\,\mathrm{wt.\%}$ at an ambient humidity of $\phi = 50\,\%\mathrm{RH}$. Dashed lines depict the water concentration after the specimen is exposed to an environment with lower ambient humidity. Dotted lines show the concentration after $1\,\mathrm{h}$ of drying while solid lines show the concentration after $7\,\mathrm{h}$. b) Water concentration c in wt.% along a single specimen's thickness for $\phi = 35\,\%\mathrm{RH}$. The black arrow indicates increasing drying time. Figure based on Figure 4 from Dyck et al. (2024c).

focus solely on the drying process and, at this stage, do not solve the balance of linear momentum. Instead, we solve Eq. (5.30) (2) for given boundary and initial conditions using a *heat-transfer step* in ABAQUS. Initially, the chemical potential is homogeneous, $\hat{\mu} = -2.04 \times 10^3\,\mathrm{J/mol}$ based on Eq. (5.31) for $\theta = 80°\mathrm{C}$ and $\phi = 50\,\%\mathrm{RH}$. This leads to an initial concentration of $\hat{c} = 3\,\mathrm{wt.\%}$. For the drying process, the boundary chemical potential on all surfaces of the specimen is adjusted to $\bar{\mu} = [-3.08, -4.07, -5.57] \times 10^3\,\mathrm{J/mol}$ according to Eq. (5.31) for $\phi = [35, 25, 15]\,\%\mathrm{RH}$. Before that, in an initial simulation step, the preconditioned specimen is initialized in a homogeneous state. The boundary conditions are subsequently applied within $0.3\,\mathrm{s}$, i.e. instantaneously in comparison with the duration of the experiment. However, we note that this choice is of $0.3\,\mathrm{s}$ is arbitrary. This mimics the removal of the specimen from a controlled environment and its placement in a testing chamber with a lower ambient humidity. Subsequently, the water diffusion or drying is allowed to take place for $7\,\mathrm{h}$. The specimen geometry is discretized using linear, hexahedral heat-conduction elements (DC3D8) with an edge length of $0.5\,\mathrm{mm}$ in length and width direction and $0.1\,\mathrm{mm}$ in thickness direction, which leads to 20 elements over the specimen thickness.

Results of the three simulations are depicted in Fig. 5.4 a) as concentration profiles along the thickness (z-direction) in the specimen center. Both the initial concentration profile after applying the corresponding chemical potential boundary condition (dashed lines), after $1\,\mathrm{h}$ of drying (dotted lines), as well as the final profile (solid lines) after $7\,\mathrm{h}$ of drying are depicted. As observed in previous publications, see, e.g., Sharma et al. (2020) and Sambale et al. (2021b), after $1\,\mathrm{h}$ a significant concentration gradient occurs within the specimen. In fact, the lower the ambient humidity, the stronger the heterogeneity of the concentration along the specimen thickness. As is to be expected, a lower ambient humidity leads to a lower concentration of water close to the surface. After $7\,\mathrm{h}$ of drying at $80^\circ\mathrm{C}$, the specimen is almost in equilibrium with it's environment, regardless of the ambient humidity content. To study the water distribution as a function of time, the concentration profile at $\phi = 35\,\%\mathrm{RH}$ is depicted for increasing simulation time in Fig. 5.4 b). The sharp initial concentration gradient along z flattens out with increasing exposure time, as the system moves towards an equilibrium between the boundary and initial chemical potentials.

In addition to the concentration heterogeneity along the specimen thickness, the drying simulation allows to study the weight loss due to drying during the experiment. In Kehrer et al. (2023), weight loss of a preconditioned specimen tested in a relaxation test at $80^\circ\mathrm{C}$ at a relative humidity of $\phi \approx 35\,\%\mathrm{RH}$ is reported to be $-1.115\,\%$. In Tab. 5.4 results from the three drying simulations are compared to the experimentally obtained mass. To this end, the mean water concentration c_{mean} in $\mathrm{wt.\%}$

is computed for the entire specimen, i.e.

$$c_{\text{mean}} = \frac{1}{V} \sum_{\alpha} c_\alpha v_\alpha, \tag{5.33}$$

where c_α is the concentration at integration point α, v_α its volume and V denotes the volume of the entire specimen. The mass of water then follows as $m_{\text{w}} = c_{\text{mean}} m_{\text{P}}$, c.f. Eq. (5.1), where m_{P} is the mass of the PA 6 specimen. The result from the simulation with a relative humidity $\phi = 35\,\%\text{RH}$ is close to the experimentally obtained values, which allows us to conclude, that the relative humidity during the relaxation experiment without HC is indeed $\phi = 35\,\%\text{RH}$. We consider the slight deviation between experiment and simulation to be due to the fact that the exact shape of the specimen used in the experiments scatters, c.f. Tab. 10 in Kehrer et al. (2023) due to the injection molding process, which is not reproduced in the simulations.

To summarize, the drying simulation does lead to a mass loss in close agreement with the one observed in experiments. In addition, the heterogeneous water profile along the specimen thickness is in qualitative agreement with previously published simulative and experimental studies. We now proceed to study the model response in a relaxation experiment.

5.3.3 Comparison of experiments and simulations

Finally we use the fully chemo-mechanically coupled model to study relaxation experiments and compare numerically obtained results with the experimentally obtained data depicted in Fig. 5.1. We therefore reproduce the simulation setup outlined in Kehrer et al. (2023). The geometry of the specimen is the same as described above. However, as we consider four nodal degrees of freedom, a *coupled temperature-displacement step* is used to model the coupling of the drying process to the viscoelastic behavior of PA 6 in ABAQUS. We use linear, hexahedral

	EXP no HC ($\phi \approx 35\,\%$RH)	EXP HC ($\phi = 50\,\%$RH)	SIM ($\phi = 35\,\%$RH)
m_{initial} in g	1.9467	1.9534	1.9321
m_{end} in g	1.94250	1.9532	1.92440
Δm	$-1.115\,\%$	$-0.0102\,\%$	$-0.8972\,\%$

	SIM ($\phi = 25\,\%$RH)	SIM ($\phi = 15\,\%$RH)
m_{initial} in g	1.9321	1.9321
m_{end} in g	1.91980	1.91540
Δm	$-1.4911\,\%$	$-2.0935\,\%$

Table 5.4: The initial total mass before testing and final total mass after testing of the specimens (i.e. PA 6 and water) is summarized for both experiments (no HC and HC) and the simulations for varying ambient humidity levels at $\theta = 80°$C. The relative deviation $\Delta m = (m_{\text{end}} - m_{\text{initial}})/m_{\text{initial}}$ is also displayed.

coupled temperature-displacement elements (C3D8T) with an identical size to the one used in the drying simulation. In the experimental setup, the preconditioned specimen is placed in the testing chamber of the DMA. The test protocol starts with a rest period of $1\,\text{h}$ during which the length of the specimen is recorded continuously and the strain amplitude is kept at $\varepsilon_0 = 0\,\%$. After the rest period, a strain $\varepsilon_0 = 0.1\,\%$ is applied with a rate of $\dot{\varepsilon}_0 = 1/\text{s}$. This strain is subsequently held constant for $6\,\text{h}$. To mimic this setup in the simulation, we apply an initial chemical potential of $\hat{\mu} = -2.04 \times 10^3$ J/mol which leads to an initially homogeneous water concentration of $\hat{c} = 3\,\text{wt.}\%$ analogously to the drying simulation. We use this initial concentration as the swelling free normalized concentration $\tilde{c}_0 = \hat{c}/c_{\max}$. The specimen surface is then exposed to a boundary chemical potential $\bar{\mu} = -3.08 \times 10^3$ J/mol. This boundary condition is ramped up in $0.3\,\text{s}$ and held constant for $1\,\text{h}$. As above, this mimics the placing of the specimen in the testing chamber and the rest period. During this time, one end of the specimen is restrained from moving, i.e. $\bar{\boldsymbol{u}} = \boldsymbol{0}$. Due to the onset of drying, the length of the specimen decreases, as the concentration falls below the

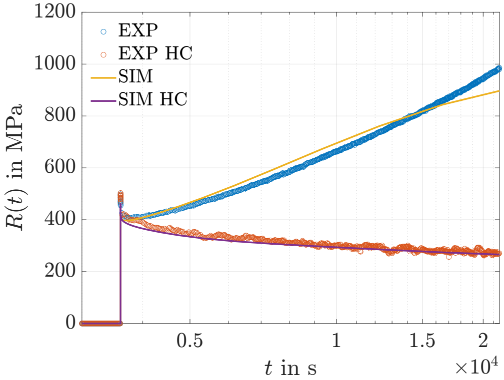

Figure 5.5: Relaxation modulus for two relaxation experiments conducted on PA 6 at 80° C. Both specimens were conditioned at a humidity level of $\phi = 50\,\%\mathrm{RH}$. In the HC experiment, a controlled humidity level of $\phi = 50\,\%\mathrm{RH}$ was enforced, while the other specimen was tested without humidity control. In addition, the results of Finite-Element simulations based on the model outlined in this publications are depicted. Figure based on Figure 5 from Dyck et al. (2024c).

swelling free concentration. After the rest period, a displacement $\bar{\boldsymbol{u}}$ leading to a strain of $\varepsilon = 0.1\,\%$ is applied with the same rate as in the experiment, which is held constant for $6\,\mathrm{h}$.

The result of the simulation is depicted in Fig. 5.5. The experiment conducted in a humidity controlled environment is, as shown during the parameter identification, reproduced accurately. In addition, the simulation of a relaxation experiment without HC closely matches the experimental results. Especially the initial decline and subsequent increase in relaxation modulus $R(t)$ during the first $4\,\mathrm{h}$ of simulation time matches the experimentally obtained curve. In fact, the slope of increasing $R(t)$ in simulation and experiment are almost identical. This is, in our simulation framework, entirely due to the drying of the specimen. As shown in Fig. 5.4 b), the mean water concentration decreases significantly due to the onset of drying. This leads to a compressive chemical strain as the concentration falls below the swelling free concentration $\tilde{c}_0$. Due to the applied mechanical boundary conditions, ε is constant in the specimen and Eq. (5.25) (1) therefore predicts an increasing stress and relaxation modulus $R(t)$. After about $5\,\mathrm{h}$ in the relaxation experiment (which is equivalent to $6\,\mathrm{h}$ of drying), the specimen is almost dry (c.f. Fig. 5.4 b)) and only negligible changes in chemical strains occur. This leads to a slight flattening of the relaxation modulus $R(t)$, and the simulation results deviate from the experimentally obtained curve which shows a further increase in $R(t)$.

5.3.4 Discussion of the results

Before concluding this chapter, several remarks regarding the results are given, in order to make the results and their limitations more clear:

Chemical parameters. The chosen chemical part of the free energy, based on the Flory-Huggins theory, introduces only a single unknown parameter. This interaction parameter was identified by studying the absorption of water exposed to a humid atmosphere as depicted in Fig. 5.3 a). All other chemical parameters in the model are taken from literature.

Mass loss. As shown during the drying simulation, c.f. Tab. 5.4, the mass loss of the PA 6 specimen observed in the experiment is reproduced based on the derived chemical model.

Relaxation modulus. When the fully chemo-mechanically coupled model is used to study the behavior in a relaxation experiment, only the drying of the PA 6 specimen leads to an increase in the relaxation modulus $R(t)$. The experimentally observed increase in $R(t)$ is reproduced by the chemo-mechanically coupled model derived in this work.

Glass transition. As outlined in Sec. 5.2, both experimental (Miri et al., 2009; Sambale et al., 2021a) and numerical studies (Broudin et al., 2015a;b) indicate that the glass transition temperature θ_g of PA 6 strongly varies with the water content. This is due to an increasing chain mobility caused by the presence of water molecules. This fact is not considered in our model. However, the model outlined in Broudin et al. (2015a) can be used as a starting point to include such a transition.

Temperature dependency. In this work, we consider the temperature to be constant at all times. In order to incorporate non isothermal cases, the derivation of a heat-equation in a thermo-chemo-mechanical setting would be required. This has been done in other works, see, e.g., Chester and Anand (2011) and Di Leo and Anand (2013). In addition, each node in the Finite-Element scheme would have 5 degrees of freedom, i.e. three displacement degrees of freedom, a chemical one and temperature. This would require a more involved implementation scheme, relying on the `UEL` of ABAQUS.

Statistical relevance. In experimental studies on PA 6, such as Sambale et al. (2021a), Sambale et al. (2021b), Sharma et al. (2020) and many other, scatterings have been observed in both parameters and material response to applied loads and boundary conditions. Due to the fact that our model predictions are compared with results of only a single specimen, no statement regarding the statistical relevance of our data can be given. To quantify this, further experimental investigations are necessary in future work.

5.4 Conclusion

In the present chapter, a chemo-mechanically coupled continuum model is derived with the goal of predicting changes in water concentration in

PA 6 during mechanical testing using Finite-Element simulations and its influence on mechanical behavior. The main results are:

- The coupling between chemical and mechanical fields is derived by means of a thermodynamically consistent constitutive theory. To this end, a free energy for the mixture of water and PA 6 is additively decomposed into mechanical and chemical parts. While the former part is based on standard linear-viscoelastic Maxwell elements, the chemical part relies on the Flory-Huggins theory of mixing of monomers with solvent molecules. Thereby, a parameter for the interaction during mixing is introduced. The coupling of chemical fields to mechanical fields arises due to chemical strains, while the mechanical stress leads to a water flux and thus couples mechanical to chemical fields.
- The derived model is implemented in the commercial Finite-Element program ABAQUS, relying on a newly proposed version of the heat-transfer analogy, exploiting the similarity of heat-equation and diffusion equation. Parameters for the chemical part of the model are mostly taken from literature, while the Flory-Huggins interaction parameter is identified to match experimentally obtained water uptake curves of polyamide exposed to humid environments. The Maxwell elements are identified by fitting to an experiment, where no water diffusion is involved.
- The identified model is capable of reproducing mass loss due to drying as well as an increasing relaxation modulus $R(t)$ during a prolonged relaxation test, where the specimen exhibits significant drying.

Chapter 6

Summary, Conclusions and Outlook

6.1 Summary and Conclusions

In this thesis, we developed chemo-mechanically coupled continuum models and a scheme for their application in a commercial FEM solver. First, we proposed a scheme to solve chemo-mechanically coupled problems by relying on the chemical potential as the degree of freedom for the chemical field. We validated the scheme against established solution schemes and analytical results. We then proposed a chemo-mechanically coupled theory capable of predicting experimentally observed phase-separation behavior in thin film metal hydrogen systems, using Pd-H and Nb-H as model systems. The final contribution deals with the drying process of PA 6 coupled to its viscoelastic behavior. In the following, we summarize each chapter.

Summary of Chapter 3:

- Choosing chemical potential as the degree of freedom in Finite-Element simulations has numerous advantages compared to choosing concentration. This includes the possibility of simulating open systems and better numerical properties due to the unbounded nature of the chemical potential.

- The well-established heat-transfer analogy (Oh et al., 2010), allowing users of commercial FEM solvers to study chemo-mechanically coupled processes by relying on concentration as the degree of freedom, can be readily extended to chemical potential as the degree of freedom.

Summary of Chapter 4:

- The proposed chemo-mechanically coupled phase-field model accurately captures the phase-separation behavior of thin film metal hydrogen systems. This was confirmed by comparing analytical and numerical model predictions to experimental results.
- Considering homogeneous systems allows the efficient prediction of critical concentrations for the formation of hydrides, without the need for time-consuming numerical simulations.

Summary of Chapter 5:

- For PA 6, experimentally observed increases in the relaxation modulus at elevated temperatures can be explained by the drying of specimens and the resulting, chemically induced, contraction of the specimens.
- The chemo-mechanically coupled behavior of PA 6 observed in experiments is accurately predicted by the combination of the Flory-Huggins theory (Flory, 1942; Huggins, 1942) and a generalized Maxwell model.

6.2 Outlook

In[1] future work on phase-separating metal hydrogen systems, we plan to include several of the aspects outlined in Chapter 4 in the model. This requires a relaxation of several of the assumptions introduced in this thesis. These include:

---

[1] This paragraph is based on the outlook of section 6 of the publication "Hydride formation in open thin film metal hydrogen systems: Cahn-Hilliard-type phase-field simulations coupled to elasto-plastic deformations" (Dyck et al., 2024c).

- Adding a structural order parameter to the phase-field whose evolution is governed by an Allen-Cahn equation, in order to introduce interfacial anisotropies, see, e.g., Han et al. (2019), Heo et al. (2019) and others.
- As the thin films observed in experiments are either epitaxial or nanocrystalline (Wagner et al., 2019), both the isotropic elasticity as well as the isotropic, phenomenological plasticity model could be replaced by a mechanism-based model, such as crystal plasticity (Prahs et al., 2024). An extension to gradient crystal plasticity, see, e.g., Forest et al. (2000) could possibly also allow for the inclusion of the size effect observed in experiments.
- To more closely reproduce the suspected cylindrical shapes of hydride precipitates, the inclusion of an effect accounting for the loss of coherence between film and substrate would be suitable.
- Finally, the proposed model can be used to study hydride dissolution during hydrogen release, in addition to the well known hysteresis effect Schwarz and Khachaturyan (1995), which has not been done in this work.

In addition the authors plan to investigate hydride precipitate shapes and sizes quantitatively using the model, in order to identify the key influencing factors for hydride formation during hydrogen absorption. In[2] future work on the water diffusion in PA 6, we plan to extend the outlined model by incorporating parameter changes depending on the local water concentration, inspired by Broudin et al. (2015a). In this setting, all parameters depend on the difference between current temperature θ and glass transition temperature $\theta_{\mathrm{g}}(c)$, which is itself a function of local water content c. Such an approach would, in our opinion, not only increase the accuracy of the model predictions, but

---

[2] This paragraph is based on the outlook of section 4 of the publication "Modeling and FE simulation of coupled water diffusion and viscoelasticity in relaxation tests of polyamide 6" (Dyck et al., 2024c).

also allow the usage of the model at other temperature levels or in settings with non-constant temperatures. Furthermore, an extension to account for nonlinear viscoelastic behavior can be incorporated, see, e.g., Zink et al. (2022).

Bibliography

Abromeit, A., Siebrecht, R., Song, G., Zabel, H., Klose, F., Nagengast, D., Weidinger, A., 1997. Thickness dependence of the hydrogen solubility in epitaxial Nb(110) films grown on Al_2O_3(11.0) substrates. Journal of Alloys and Compounds 253, 58–61.

Adams, B. D., Chen, A., 2011. The role of palladium in a hydrogen economy. Materials Today 14 (6), 282–289.

Alefeld, G., 1972. Phase transitions of hydrogen in metals due to elastic interaction. Berichte der Bunsengesellschaft für physikalische Chemie 76 (8), 746–755.

Ammar, K., Appolaire, B., Cailletaud, G., Forest, S., 2009. Combining phase field approach and homogenization methods for modelling phase transformation in elastoplastic media. European Journal of Computational Mechanics 18 (5–6), 485–523.

Anand, L., 2012. A Cahn-Hilliard-type theory for species diffusion coupled with large elastic-plastic deformations. Journal of the Mechanics and Physics of Solids 60 (12), 1983–2002.

Armand, M., Tarascon, J. M., 2008. Building better batteries. Nature 451 (7179), 652–657.

Arndt, D., Bangerth, W., Bergbauer, M., Feder, M., Fehling, M., Heinz, J., Heister, T., Heltai, L., Kronbichler, M., Maier, M., et al., 2023. The deal. II library, version 9.5. Journal of Numerical Mathematics 31 (3), 231–246.

Bai, Y., Mianroodi, J. R., Ma, Y., da Silva, A. K., Svendsen, B., Raabe, D., 2022. Chemo-mechanical phase-field modeling of iron oxide reduction with hydrogen. Acta Materialia 231, Article 117899.

Bair, J., Asle Zaeem, M., Schwen, D., 2017. Formation path of δ-hydrides in zirconium by multiphase field modeling. Acta Materialia 123, 235–244.

Baldi, A., Narayan, T. C., Koh, A. L., Dionne, J. A., 2014. In situ detection of hydrogen-induced phase transitions in individual palladium nanocrystals. Nature Materials 13 (12), 1143–1148.

Barrera, O., Tarleton, E., Tang, H. W., Cocks, A. C., 2016. Modelling the coupling between hydrogen diffusion and the mechanical behaviour of metals. Computational Materials Science 122, 219–228.

Barrett, J., Blowey, J., 1999. Finite element approximation of the Cahn-Hilliard equation with concentration dependent mobility. Mathematics of Computation 68 (226), 487–517.

Bertram, A., 2012. Elasticity and Plasticity of Large Deformations, 3rd Edition. Springer, Berlin.

Bistri, D., Di Leo, C. V., 2023. A continuum electro-chemo-mechanical gradient theory coupled with damage: application to Li-metal filament growth in all-solid-state batteries. Journal of the Mechanics and Physics of Solids 174, Article 105252.

Böhlke, T., Henning, F., Hrymak, A. N., Kärger, L., Weidenmann, K., Wood, J. T., 2019. Continuous-Discontinuous Fiber-Reinforced Polymers. An Integrated Engineering Approach. Hanser, Munich.

Bradshaw, R., Brinson, L., 1997. A sign control method for fitting and interconverting material functions for linearly viscoelastic solids. Mechanics of Time-Dependent Materials 1 (1), 85–108.

Broudin, M., Le Gac, P.-Y., Le Saux, V., Champy, C., Robert, G., Charrier, P., Marco, Y., 2015a. Water diffusivity in PA66: experimental characterization and modeling based on free volume theory. European Polymer Journal 67, 326–334.

Broudin, M., Le Saux, V., Le Gac, P.-Y., Champy, C., Robert, G., Charrier, P., Marco, Y., 2015b. Moisture sorption in polyamide 6.6: experimental investigation and comparison to four physical-based models. Polymer Testing 43, 10–20.

Burlaka, V., Roddatis, V., Bongers, M. D., Pundt, A., 2017. Defect generation in Pd layers by ’smart’ films with high H-affinity. Scientific Reports 7 (1), Article 9564.

Burlaka, V., Wagner, S., Hamm, M., Pundt, A., 2016. Suppression of phase transformation in Nb-H thin films below switchover thickness. Nano Letters 16 (10), 6207–6212.

Burlaka, V., Wagner, S., Pundt, A., 2015. In-situ STM and XRD studies on Nb-H films: coherent and incoherent phase transitions. Journal of Alloys and Compounds 645, S388–S391.

Cahn, J. W., Hilliard, J. E., 1958. Free energy of a nonuniform system. I. Interfacial free energy. The Journal of Chemical Physics 28 (2), 258–267.

Castelli, G. F., von Kolzenberg, L., Horstmann, B., Latz, A., Dörfler, W., 2021. Efficient simulation of chemical-mechanical coupling in battery active particles. Energy Technology 9 (6), Article 2000835.

Chen, L., Fan, F., Hong, L., Chen, J., Ji, Y. Z., Zhang, S., Zhu, T., Chen, L., 2014. A phase-field model coupled with large elasto-plastic deformation: application to lithiated silicon electrodes. Journal of the Electrochemical Society 161 (11), Article F3164.

Chester, S. A., Anand, L., 2011. A thermo-mechanically coupled theory for fluid permeation in elastomeric materials: application to thermally responsive gels. Journal of the Mechanics and Physics of Solids 59 (10), 1978–2006.

Chester, S. A., Di Leo, C. V., Anand, L., 2015. A finite element implementation of a coupled diffusion-deformation theory for elastomeric gels. International Journal of Solids and Structures 52, 1–18.

Cichy, K., Świerczek, K., 2021. Influence of Doping on the Transport Properties of $\mathrm{Y}_{1-x}\mathrm{Ln}_x\mathrm{MnO}_{3+\delta}$ (Ln: Pr, Nd). Crystals 11 (5), Article 510.

Čížek, J., Procházka, I., Bečvář, F., Kužel, R., Cieslar, M., Brauer, G., Anwand, W., Kirchheim, R., Pundt, A., 2004. Hydrogen-induced defects in bulk niobium. Physical Review B 69 (22), Article 224106.

Coleman, B. D., Gurtin, M. E., 1967. Thermodynamics with internal state variables. The Journal of Chemical Physics 47 (2), 597–613.

Coleman, B. D., Noll, W., 1963. The thermodynamics of elastic materials with heat conduction and viscosity. Archive for Rational Mechanics and Analysis 13, 167–178.

Copetti, M. I. M., Elliott, C. M., 1992. Numerical analysis of the Cahn-Hilliard equation with a logarithmic free energy. Numerische Mathematik 63, 39–65.

Crank, J., 1979. The Mathematics of Diffusion, 3rd Edition. Oxford University Press, Oxford.

DeHoff, R., 2006. Thermodynamics in Materials Science, 2nd Edition. CRC Press, Boca Raton.

Di Leo, C. V., Anand, L., 2013. Hydrogen in metals: a coupled theory for species diffusion and large elastic-plastic deformations. International Journal of Plasticity 43, 42–69.

Di Leo, C. V., Rejovitzky, E., Anand, L., 2014. A Cahn-Hilliard-type phase-field theory for species diffusion coupled with large elastic deformations: Application to phase-separating Li-ion electrode materials. Journal of the Mechanics and Physics of Solids 70 (1), 1–29.

Di Leo, C. V., Rejovitzky, E., Anand, L., 2015. Diffusion-deformation theory for amorphous silicon anodes: the role of plastic deformation on electrochemical performance. International Journal of Solids and Structures 67, 283–296.

Díaz, A., Alegre, J. M., Cuesta, I. I., 2016. Coupled hydrogen diffusion simulation using a heat transfer analogy. International Journal of Mechanical Sciences 115–116, 360–369.

Doi, M., 1996. Introduction to Polymer Pysics. Clarendon Press, Oxford.

Domininghaus, H., 2012. Kunststoffe: Eigenschaften und Anwendungen, 8th Edition. Springer, Berlin.

Durbin, D. J., Malardier-Jugroot, C., 2013. Review of hydrogen storage techniques for on board vehicle applications. International Journal of Hydrogen Energy 38 (34), 14595–14617.

Dyck, A., Böhlke, T., Pundt, A., Wagner, S., 2024a. Phase transformation in the niobium hydrogen system: effects of elasto-plastic deformations on phase stability predicted by a thermodynamic model. Scripta Materialia 251, Article 116209.

Dyck, A., Böhlke, T., Pundt, A., Wagner, S., 2024b. Phase transformation in the palladium hydrogen system: effects of boundary conditions on phase stabilities. Scripta Materialia 247, Article 116117.

Dyck, A., Gisy, J., Hille, F., Wagner, S., Pundt, A., Böhlke, T., 2025. Hydride formation in open thin film metal hydrogen systems: Cahn-Hilliard-type phase-field simulations coupled to elasto-plastic deformations. Mechanics of Materials (accepted).

Dyck, A., Groß, L., Keursten, J., Kehrer, L., Böhlke, T., 2024c. Modeling and FE simulation of coupled water diffusion and viscoelasticity in relaxation tests of polyamide 6. Continuum Mechanics and Thermodynamics 36, 935–953.

Elliott, C. M., French, D. A., Milner, F., 1989. A second order splitting method for the Cahn-Hilliard equation. Numerische Mathematik 54, 575–590.

Fernandez, A., Caretta, L., Das, S., Klewe, C., Lou, D., Parsonnet, E., Gao, R., Luo, A., Shafer, P., Martin, L. W., 2021. Strain-induced orbital contributions to oxygen electrocatalysis in transition-metal perovskites. Advanced Energy Materials 11 (46), Article 2102175.

Fernández-Sousa, R., Betegón, C., Martínez-Pañeda, E., 2020. Analysis of the influence of microstructural traps on hydrogen assisted fatigue. Acta Materialia 199, 253–263.

Flory, P. J., 1942. Thermodynamics of high polymer solutions. The Journal of Chemical Physics 10 (1), 51–61.

Forest, S., Ammar, K., Appolaire, B., 2011. Micromorphic vs. Phase-Field Approaches for Gradient Viscoplasticity and Phase Transformations. In: Markert, B. (Ed.), Advances in Extended and Multifield Theories for Continua. Springer, Berlin, pp. 69–88.

Forest, S., Barbe, F., Cailletaud, G., 2000. Cosserat modelling of size effects in the mechanical behaviour of polycrystals and multi-phase materials. International Journal of Solids and Structures 37 (46–47), 7105–7126.

Fruchter, L., Brouet, V., Colson, D., Moussy, J.-B., Forget, A., Li, Z., 2018. Electrochemical oxygen intercalation into $\mathrm{Sr_2IrO_4}$. Journal of Physics and Chemistry of Solids 112, 1–7.

Fukai, Y., 2005. The Metal-Hydrogen System: Basic Bulk Properties, 2nd Edition. Springer, Berlin.

Gajek, S., Schneider, M., Böhlke, T., 2022. An FE-DMN method for the multiscale analysis of thermomechanical composites. Computational Mechanics 69 (5), 1087–1113.

Gear, C. W., 1967. The numerical integration of ordinary differential equations. Mathematics of Computation 21 (98), 146–156.

Gobbi, G., Colombo, C., Miccoli, S., Vergani, L., 2019. A fully coupled implementation of hydrogen embrittlement in FE analysis. Advances in Engineering Software 135 (November 2018), Article 102673.

Greenwood, N. N., Earnshaw, A., 1997. Chemistry of the Elements, 2nd Edition. Butterworth-Heinemann, Oxford.

Gremaud, R., Gonzalez-Silveira, M., Pivak, Y., De Man, S., Slaman, M., Schreuders, H., Dam, B., Griessen, R., 2009. Hydrogenography of PdH_x thin films: influence of H-induced stress relaxation processes. Acta Materialia 57 (4), 1209–1219.

Greve, R., 2003. Kontinuumsmechanik: Ein Grundkurs für Ingenieure und Physiker. Springer, Berlin.

Griessen, R., Strohfeldt, N., Giessen, H., 2016. Thermodynamics of the hybrid interaction of hydrogen with palladium nanoparticles. Nature Materials 15 (3), 311–317.

Guo, X., Shi, S.-Q., Zhang, Q., Ma, X., 2008. An elastoplastic phase-field model for the evolution of hydride precipitation in zirconium. Part I: smooth specimen. Journal of Nuclear Materials 378 (1), 110–119.

Gurtin, M. E., Fried, E., Anand, L., 2010. The Mechanics and Thermodynamics of Continua. Cambridge University Press, Cambdrige.

Gurtin, M. E., Vargas, A. S., 1971. On the classical theory of reacting fluid mixtures. Archive for Rational Mechanics and Analysis 43, 179–197.

Hageman, T., Martínez-Pañeda, E., 2023. A phase field-based framework for electro-chemo-mechanical fracture: crack-contained electrolytes, chemical reactions and stabilisation. Computer Methods in Applied Mechanics and Engineering 415, Atricle 116235.

Hamm, M., Burlaka, V., Wagner, S., Pundt, A., 2015. Achieving reversibility of ultra-high mechanical stress by hydrogen loading of thin films. Applied Physics Letters 106 (24), Article 243108.

Han, G., Zhao, Y., Zhou, C., Lin, D.-Y., Zhu, X., Zhang, J., Hu, S., Song, H., 2019. Phase-field modeling of stacking structure formation and transition of δ-hydride precipitates in zirconium. Acta Materialia 165, 528–546.

Haupt, P., 2002. Continuum Mechanics and Theory of Materials, 2nd Edition. Springer, Berlin.

Heo, T. W., Colas, K. B., Motta, A. T., Chen, L. Q., 2019. A phase-field model for hydride formation in polycrystalline metals: application to δ-hydride in zirconium alloys. Acta Materialia 181, 262–277.

Huggins, M. L., 1942. Theory of solutions of high polymers. Journal of the American Chemical Society 64 (7), 1712–1719.

Jalocha, D., Constantinescu, A., Neviere, R., 2015. Revisiting the identification of generalized Maxwell models from experimental results. International Journal of Solids and Structures 67–68, 169–181.

Jia, N., Fraenkel, H. A., Kagan, V. A., 2004. Effects of moisture conditioning methods on mechanical properties of injection molded nylon 6. Journal of Reinforced Plastics and Composites 23 (7), 729–737.

Jia, N., Kagan, V. A., 2001. Mechanical Performance of Polyamides with Influence of Moisture and Temperature - Accurate Evaluation and Better Understanding. In: Moalli, J. (Ed.), Plastics Failure Analysis and Prevention. William Andrew Inc, Norwich NY, pp. 95–104.

Jia, Y. J., Han, W. Z., 2023. Mechanisms of hydride nucleation, growth, reorientation, and embrittlement in zirconium: a review. Materials 16 (6), Article 2419.

Johlitz, M., 2015. Zum Alterungsverhalten von Polymeren: Experimentell gestützte, thermochemische Modellbildung und numerische Simulation. Habilitationsschrift, Universität der Bundeswehr München.

Johlitz, M., Lion, A., 2013. Chemo-thermomechanical ageing of elastomers based on multiphase continuum mechanics. Continuum Mechanics and Thermodynamics 25 (5), 605–624.

Kehrer, L., Keursten, J., Hirschberg, V., Böhlke, T., 2023. Dynamic mechanical analysis of PA 6 under hydrothermal influences and viscoelastic material modeling. Journal of Thermoplastic Composite Materials 36 (11), 1–35.

Kehrer, L., Pinter, P., Böhlke, T., 2017. Mean and full field homogenization of artificial long fiber reinforced thermoset polymers. Proceedings in Applied Mathematics and Mechanics 17 (1), 603–604.

Kirsch, C., 1898. Die Theorie der Elastizitaet und die Bedurfnisse der Festigkeitslehre. Zeitschrift des Vereines Deutscher Ingenieure 42, 797–807.

Krom, A. H., Koers, R. W., Bakker, A., 1999. Hydrogen transport near a blunting crack tip. Journal of the Mechanics and Physics of Solids 47 (4), 971–992.

Kumnick, A. J., Johnson, H. H., 1980. Deep trapping for hydrogen iron. Acta Metallurgica 28 (1), 33–39.

Larché, F., Cahn, J. W., 1973. A linear theory of thermochemical equilibrium of solids under stress. Acta Metallurgica 21 (8), 1051–1063.

Larché, F., Cahn, J. W., 1978. A nonlinear theory of thermochemical equilibrium of solids under stress. Acta Metallurgica 26 (1), 53–60.

Laudahn, U., Fähler, S., Krebs, H., Pundt, A., Bicker, M., v. Hülsen, U., Geyer, U., Kirchheim, R., 1999. Determination of elastic constants in thin films using hydrogen loading. Applied Physics Letters 74 (5), 647–649.

Liu, I.-S., 1972. Method of lagrange multipliers for exploitation of the entropy principle. Archive for Rational Mechanics and Analysis 46, 131–148.

Liu, L.-B., Yi, C., Mi, H.-C., Zhang, S. L., Fu, X.-Z., Luo, J.-L., Liu, S., 2024. Perovskite oxides toward oxygen evolution reaction: intellectual design strategies, properties and perspectives. Electrochemical Energy Reviews 7 (1), 1–37.

Lu, C., Huang, W., Van Vleck, E. S., 2013. The cutoff method for the numerical computation of nonnegative solutions of parabolic PDEs with application to anisotropic diffusion and lubrication-type equations. Journal of Computational Physics 242, 24–36.

Makuch, M., Kovacevic, S., Wenman, M. R., Martínez-Pañeda, E., 2024. A microstructure-sensitive electro-chemo-mechanical phase-field model of pitting and stress corrosion cracking. Corrosion Science 232, Article 112031.

Matsumoto, K., Kawasoko, H., Kasai, H., Nishibori, E., Fukumura, T., 2020. Increased electrical conduction with high hole mobility in anti-$\mathrm{ThCr_2Si_2}$-type $\mathrm{La_2O_2Bi}$ via oxygen intercalation adjacent to Bi square net. Applied Physics Letters 116 (19), Article 191901.

McCay, M. H., Shafiee, S., 2020. Hydrogen: An Energy Carrier. In: Lecther, T. M. (Ed.), Future energy - Improved, Sustainable and Clean Options for our planet, 3rd Edition. Elsevier, Amsterdam, pp. 475–493.

Miehe, C., Hildebrand, F. E., Böger, L., 2014. Mixed variational potentials and inherent symmetries of the Cahn-Hilliard theory of diffusive phase separation. Proceedings of the Royal Society A: Mathematical, Physical and Engineering Sciences 470 (2164), Article 20130641.

Miehe, C., Hofacker, M., Welschinger, F., 2010. A phase field model for rate-independent crack propagation: robust algorithmic implementation based on operator splits. Computer Methods in Applied Mechanics and Engineering 199 (45–48), 2765–2778.

Miri, V., Persyn, O., Lefebvre, J.-M., Seguela, R., 2009. Effect of water absorption on the plastic deformation behavior of nylon 6. European Polymer Journal 45 (3), 757–762.

Mises, R. v., 1928. Mechanik der plastischen Formänderung von Kristallen. Zeitschrift für Angewandte Mathematik und Mechanik 8 (3), 161–185.

Müller, I., 1968. A thermodynamic theory of mixtures of fluids. Archive for Rational Mechanics and Analysis 28 (1), 1–39.

Mï¿½ller, I., 1985. Thermodynamics. Pitman, London.

Nesterov, Y., 2004. Introductory Lectures on Convex Optimization: A Basic Course. Vol. 87. Springer, New York.

Nichols, J., Terzic, J., Bittle, E. G., Korneta, O. B., De Long, L. E., Brill, J., Cao, G., Seo, S. S. A., 2013. Tuning electronic structure via epitaxial strain in $\mathrm{Sr_2IrO_4}$ thin films. Applied Physics Letters 102 (14), Article 141908.

Nörthemann, K., Pundt, A., 2008. Coherent-to-semi-coherent transition of precipitates in niobium-hydrogen thin films. Physical Review B 78 (1), Article 014105.

Nörthemann, K., Pundt, A., 2011. Double-locked nucleation and growth kinetics in Nb-H thin films. Physical Review B - Condensed Matter and Materials Physics 83 (15), 1–10.

Oh, C.-S., Kim, Y.-J., Yoon, K.-B., 2010. Coupled Analysis of Hydrogen Transport using ABAQUS. Journal of Solid Mechanics and Materials Engineering 4 (7), 908–917.

Oriani, R., 1978. Hydrogen embrittlement of steels. Annual Review of Materials Science 8 (1), 327–357.

Oriani, R. A., 1970. The diffusion and trapping of hydrogen in steel. Acta Metallurgica 18 (1), 147–157.

Papenfuß, C., 2020. Continuum Thermodynamics and Constitutive Theory. Springer, Cham.

Peisl, H., 1978. Lattice strains due to hydrogen in metals. In: Alefeld, G., Vï¿½lkl, J. (Eds.), Hydrogen in metals I: Basic Properties. Springer, Berlin, pp. 53–74.

Phan, A. T., Gheribi, A. E., Chartrand, P., 2019. Modeling of coherent phase transformation and particle size effect in $\mathrm{LiFePO_4}$ cathode material and application to the charging/discharging process. Electrochimica Acta 295, 632–644.

Pivak, Y., Schreuders, H., Slaman, M., Griessen, R., Dam, B., 2011. Thermodynamics, stress release and hysteresis behavior in highly adhesive Pd-H films. International Journal of Hydrogen Energy 36 (6), 4056–4067.

Prahs, A., Schöller, L., Schwab, F. K., Schneider, D., Böhlke, T., Nestler, B., 2024. A multiphase-field approach to small strain crystal plasticity accounting for balance equations on singular surfaces. Computational Mechanics 73 (4), 773–794.

Puffr, R., Šebenda, J., 1967. On the structure and properties of polyamides. XXVII. The mechanism of water sorption in polyamides. Journal of Polymer Science Part C: Polymer Symposia 16 (1), 79–93.

Rahm, J. M., Löfgren, J., Erhart, P., 2022. Quantitative predictions of thermodynamic hysteresis: temperature-dependent character of the phase transition in Pd-H. Acta Materialia 227, Article 117697.

Rosakis, P., Rosakis, A. J., Ravichandran, G., Hodowany, J., 2000. A thermodynamic internal variable model for the partition of plastic work into heat and stored energy in metals. Journal of the Mechanics and Physics of Solids 48, 581–607.

Sambale, A. K., Maisl, M., Herrmann, H. G., Stommel, M., 2021a. Characterisation and modelling of moisture gradients in polyamide 6. Polymers 13 (18), 1–17.

Sambale, A. K., Stanko, M., Emde, J., Stommel, M., 2021b. Characterisation and FE modelling of the sorption and swelling behaviour of polyamide 6 in water. Polymers 13 (9), 20–22.

Schneemann, A., White, J. L., Kang, S., Jeong, S., Wan, L. F., Cho, E. S., Heo, T. W., Prendergast, D., Urban, J. J., Wood, B. C., et al., 2018. Nanostructured metal hydrides for hydrogen storage. Chemical Reviews 118 (22), 10775–10839.

Schober, T., Wenzl, H., 1978. The systems NbH(D), TaH(D), VH(D): structures, phase diagrams, morphologies, methods of preparation. In: Alefeld, G., Vï¿½lkl, J. (Eds.), Hydrogen in metals II: Application-Oriented Properties. Springer, Berlin, pp. 11–71.

Schoof, R., Niermann, J., Dyck, A., Böhlke, T., Dörfler, W., 2024. Efficient modeling and simulation of chemo-elasto-plastically coupled battery active particles. Computational Mechanics online first.

Schwarz, R., Khachaturyan, A., 1995. Thermodynamics of open two-phase systems with coherent interfaces. Physical Review Letters 74 (13), Article 2523.

Schwarz, R., Khachaturyan, A., 2006. Thermodynamics of open two-phase systems with coherent interfaces: application to metal–hydrogen systems. Acta Materialia 54 (2), 313–323.

Schwarz, R., Khachaturyan, A., Caro, A., Baskes, M., Martinez, E., 2020. Coherent phase decomposition in the Pd-H system. Journal of Materials Science 55 (11), 4864–4882.

Schwarze, C., Gupta, A., Hickel, T., Darvishi Kamachali, R., 2017. Phase-field study of ripening and rearrangement of precipitates under chemomechanical coupling. Physical Review B 95 (17), Article 174101.

Sharma, P., Diebels, S., 2021. A mixture theory for the moisture transport in polyamide. Continuum Mechanics and Thermodynamics 33 (4), 1891–1905.

Sharma, P., Sambale, A., Stommel, M., Maisl, M., Herrmann, H. G., Diebels, S., 2020. Moisture transport in PA6 and its influence on the mechanical properties. Continuum Mechanics and Thermodynamics 32 (2), 307–325.

Shi, S., Markmann, J., Weissmüller, J., 2018. Verifying Larché-Cahn elasticity, a milestone of 20th-century thermodynamics. Proceedings of the National Academy of Sciences 115 (43), 10914–10919.

Simo, J. C., Hughes, T. J., 1998. Computational Inelasticity. Springer, New York.

Simo, J. C., Miehe, C., 1992. Associative coupled thermoplasticity at finite strains: Formulation, numerical analysis and implementation. Computer Methods in Applied Mechanics and Engineering 98 (1), 41–104.

Simon, P. C., Aagesen, L. K., Jokisaari, A. M., Chen, L. Q., Daymond, M. R., Motta, A. T., Tonks, M. R., 2021. Investigation of δ-zirconium hydride morphology in a single crystal using quantitative phase field simulations supported by experiments. Journal of Nuclear Materials 557, Article 153303.

Smith, M., 2009. ABAQUS/Standard User's Manual, Version 6.9. Dassault Systèmes Simulia Corp, United States.

Sofronis, P., McMeeking, R. M., 1989. Numerical analysis of hydrogen transport near a blunting crack tip. Journal of the Mechanics and Physics of Solids 37 (3), 317–350.

Song, G., Remhof, A., Labergerie, D., Zabel, H., 2002. Kinetics of hydrogen absorption and desorption in epitaxial thin niobium films. Physical Review B 66 (4), Article 045407.

Spatschek, R., Gobbi, G., Hüter, C., Chakrabarty, A., Aydin, U., Brinckmann, S., Neugebauer, J., 2016. Scale bridging description of coherent phase equilibria in the presence of surfaces and interfaces. Physical Review B 94 (13), Article 134106.

Steinbach, I., 2009. Phase-field models in materials science. Modelling and Simulation in Materials Science and Engineering 17 (7), Article 073001.

Steinbach, I., Shchyglo, O., 2011. Phase-field modelling of microstructure evolution in solids: perspectives and challenges. Current Opinion in Solid State and Materials Science 15 (3), 87–92.

Stoney, G. G., 1909. The tension of metallic films deposited by electrolysis. Proceedings of the Royal Society of London. Series A, Containing Papers of a Mathematical and Physical Character 82 (553), 172–175.

Switendick, A. C., 1979. Band structure calculations for metal hydrogen systems. Zeitschrift für Physikalische Chemie 117, 89–112.

Tschoegl, N. W., Knauss, W. G., Emri, I., 2002. Poisson's ratio in linear viscoelasticity-a critical review. Mechanics of Time-Dependent Materials 6, 3–51.

Ubachs, R. L. J. M., Schreurs, P. J. G., Geers, M. G. D., 2004. A nonlocal diffuse interface model for microstructure evolution of tin-lead solder. Journal of the Mechanics and Physics of Solids 52 (8), 1763–1792.

Venoor, V., Park, J. H., Kazmer, D. O., Sobkowicz, M. J., 2021. Understanding the effect of water in polyamides: a review. Polymer Reviews 61 (3), 598–645.

Vlasveld, D. P., Groenewold, J., Bersee, H. E., Picken, S. J., 2005. Moisture absorption in polyamide-6 silicate nanocomposites and its influence on the mechanical properties. Polymer 46 (26), 12567–12576.

Voskuilen, T. G., Pourpoint, T. L., 2013. Phase field modeling of hydrogen transport and reaction in metal hydrides. International Journal of Hydrogen Energy 38 (18), 7363–7375.

Šilhavï¿½, M., 1997. The Mechanics and Thermodynamics of Continuous Media. Springer, Berlin.

Wagner, S., Klose, P., Burlaka, V., Nörthemann, K., Hamm, M., Pundt, A., 2019. Structural phase transitions in niobium hydrogen thin films: mechanical stress, phase equilibria and critical temperatures. ChemPhysChem 20 (14), 1890–1904.

Wagner, S., Pundt, A., 2016. Quasi-thermodynamic model on hydride formation in palladium-hydrogen thin films: impact of elastic and microstructural constraints. International Journal of Hydrogen Energy 41 (4), 2727–2738.

Wagner, S., Uchida, H., Burlaka, V., Vlach, M., Vlcek, M., Lukac, F., Cizek, J., Baehtz, C., Bell, A., Pundt, A., 2011. Achieving coherent phase transition in palladium-hydrogen thin films. Scripta Materialia 64 (10), 978–981.

Weissmüller, J., 2024. Coherent phase change in interstitial solutions: a hierarchy of instabilities. Advanced Science 11 (21), Article 2308554.

Wetzel, P., Sambale, A. K., Uhlig, K., Stommel, M., Schneider, B., Kaiser, J. M., 2023. Hygromechanical behavior of polyamide 6.6: experiments and modeling. Polymers 15 (16), 1–17.

Wicht, D., Schneider, M., Böhlke, T., 2021. Computing the effective response of heterogeneous materials with thermomechanically coupled constituents by an implicit fast Fourier transform-based approach. International Journal for Numerical Methods in Engineering 122 (5), 1307–1332.

Wicke, E., Brodowsky, H., Züchner, H., 1978. Hydrogen in Palladium and Palladium Alloys. In: Alefeld, G., Vï¿½lkl, J. (Eds.), Hydrogen in Metals II: Application-Oriented Properties. Springer, Berlin, pp. 73–155.

Wilmers, J., Bargmann, S., 2015. A continuum mechanical model for the description of solvent induced swelling in polymeric glasses: thermomechanics coupled with diffusion. European Journal of Mechanics, A/Solids 53, 10–18.

Wodo, O., Ganapathysubramanian, B., 2011. Computationally efficient solution to the Cahn-Hilliard equation: adaptive implicit time schemes, mesh sensitivity analysis and the 3D isoperimetric problem. Journal of Computational Physics 230 (15), 6037–6060.

Xia, J., Zhang, N., Yang, Y., Chen, X., Wang, X., Pan, F., Yao, J., 2023. Lanthanide contraction builds better high-voltage $\mathrm{LiCoO_2}$ batteries. Advanced Functional Materials 33 (8), Article 2212869.

Zabel, H., Peisl, H., 1979. Sample-shape-dependent phase transition of hydrogen in niobium. Physical Review Letters 42 (8), Article 511.

Zhang, L., Tonks, M. R., Gaston, D., Peterson, J. W., Andrs, D., Millett, P. C., Biner, B. S., 2013. A quantitative comparison between C0 and C1 elements for solving the Cahn-Hilliard equation. Journal of Computational Physics 236, 74–80.

Zhu, Y., Wook Heo, T., Rodriguez, J. N., Weber, P. K., Shi, R., Baer, B. J., Morgado, F. F., Antonov, S., Kweon, K. E., Watkins, E. B., Savage, D. J., Chapman, J. E., Keilbart, N. D., Song, Y., Zhen, Q., Gault, B., Vogel, S. C., Sen-Britain, S. T., Shalloo, M. G., Orme, C., Bagge-Hansen, M., Hahn, C., Pham, T. A., Macdonald, D. D., Roger Qiu, S., Wood, B. C., 2022. Hydriding of titanium: recent trends and perspectives in advanced characterization and multiscale modeling. Current Opinion in Solid State and Materials Science 26 (6), Article 101020.

Zink, T., Kehrer, L., Hirschberg, V., Wilhelm, M., Böhlke, T., 2022. Nonlinear Schapery viscoelastic material model for thermoplastic polymers. Journal of Applied Polymer Science 139 (17), Article 52028.

Zï¿½ttel, A., Borgschulte, A., Schlapbach, L., 2008. Hydrogen as a Future Energy Carrier. Wiley, Weinheim.

Schriftenreihe Kontinuumsmechanik im Maschinenbau
Karlsruher Institut für Technologie (KIT)
(ISSN 2192-693X)

Band 1 Felix Fritzen
Microstructural modeling and computational homogenization of the physically linear and nonlinear constitutive behavior of micro-heterogeneous materials.
ISBN 978-3-86644-699-1

Band 2 Rumena Tsotsova
Texturbasierte Modellierung anisotroper Fließpotentiale.
ISBN 978-3-86644-764-6

Band 3 Johannes Wippler
Micromechanical finite element simulations of crack propagation in silicon nitride.
ISBN 978-3-86644-818-6

Band 4 Katja Jöchen
Homogenization of the linear and non-linear mechanical behavior of polycrystals.
ISBN 978-3-86644-971-8

Band 5 Stephan Wulfinghoff
Numerically Efficient Gradient Crystal Plasticity
with a Grain Boundary Yield Criterion and
Dislocation-based Work-Hardening.
ISBN 978-3-7315-0245-6

Band 6 Viktor Müller
Micromechanical modeling of short-fiber
reinforced composites.
ISBN 978-3-7315-0454-2

Band 7 Florian Rieger
Work-hardening of dual-phase steel.
ISBN 978-3-7315-0513-6

Band 8 Vedran Glavas
Micromechanical Modeling and Simulation of Forming Processes.
ISBN 978-3-7315-0602-7

Band 9 Eric Bayerschen
Single-crystal gradient plasticity with an accumulated plastic slip: Theory and applications.
ISBN 978-3-7315-0606-5

Band 10 Bartholomäus Brylka
Charakterisierung und Modellierung der Steifigkeit von langfaserverstärktem Polypropylen.
ISBN 978-3-7315-0680-5

Band 11 Rudolf Neumann
Two-Scale Thermomechanical Simulation of Hot Stamping.
ISBN 978-3-7315-0714-7

Band 12 Mauricio Lobos Fernández
Homogenization and materials design of mechanical properties of textured materials based on zeroth-, first- and second-order bounds of linear behavior.
ISBN 978-3-7315-0770-3

Band 13 Malte Schemmann
Biaxial Characterization and Mean-field Based Damage Modeling of Sheet Molding Compound Composites.
ISBN 978-3-7315-0818-2

Band 14 Jürgen Albiez
Finite element simulation of dislocation based plasticity and diffusion in multiphase materials at high temperature.
ISBN 978-3-7315-0918-9

Die Bände sind unter www.ksp.kit.edu als PDF frei verfügbar oder als Druckausgabe bestellbar.

Band 15 Maria Loredana Kehrer
Thermomechanical Mean-Field Modeling and Experimental Characterization of Long Fiber-Reinforced Sheet Molding Compound Composites.
ISBN 978-3-7315-0924-0

Band 16 Peter Hölz
A dynamic and statistical analysis of the temperature- and fatigue behavior of a race power unit – The effect of different thermodynamic states.
ISBN 978-3-7315-0988-2

Band 17 Andreas Prahs
A Gradient Crystal Plasticity Theory
Based on an Extended Energy Balance.
ISBN 978-3-7315-1025-3

Band 18 Johannes Ruck
Modeling martensitic phase transformation in
dual phase steels based on a sharp interface theory.
ISBN 978-3-7315-1072-7

Band 19 Hannes Erdle
Modeling of Dislocation - Grain Boundary Interactions in Gradient Crystal Plasticity Theories.
ISBN 978-3-7315-1196-0

Band 20 Johannes Görthofer
Microstructure generation and micromechanical modeling of sheet molding compound composites.
ISBN 978-3-7315-1205-9

Band 21 Daniel Wicht
Efficient fast Fourier transform-based solvers for computing the thermomechanical behavior of applied materials.
ISBN 978-3-7315-1220-2

Band 22 Juliane Lang
Thermomechanical Modeling and Experimental
Characterization of Sheet Molding Compound Composites.
ISBN 978-3-7315-1232-5

Die Bände sind unter www.ksp.kit.edu als PDF frei verfügbar oder als Druckausgabe bestellbar.

Band 23 Julian Karl Bauer
Fiber Orientation Tensors and Mean Field Homogenization: Application to Sheet Molding Compound.
ISBN 978-3-7315-1262-2

Band 24 Sebastian Gajek
Deep material networks for efficient scale-bridging in thermomechanical simulations of solids.
ISBN 978-3-7315-1278-3

Band 25 Jannick Kuhn
Microstructure modeling and crystal plasticity parameter identification for predicting the cyclic mechanical behavior of polycrystalline metals.
ISBN 978-3-7315-1272-1

Band 26 Felix Ernesti
A computational multi-scale approach for brittle materials.
ISBN 978-3-7315-1285-1

Band 27 Patrick Arthur Hessman
On multi-scale modeling of fatigue in short glass fiber reinforced thermoplastics.
ISBN 978-3-7315-1398-8

Band 28 Benedikt Sterr
Machine learning aided multiscale mechanics of fiber suspensions.
ISBN 978-3-7315-11421-3

Band 29 Maximilian Krause
Local Stresses and Strains in Polycrystals.
ISBN 978-3-7315-1411-4

Band 30 Johannes Keursten
Thermoviscoelastic Modeling of Thermoplastic Polymers.
ISBN 978-3-7315-1422-0

Die Bände sind unter www.ksp.kit.edu als PDF frei verfügbar oder als Druckausgabe bestellbar.

Band 31 Alexander Dyck

Chemo-Mechanically Coupled Models in Continuum Thermodynamics.

ISBN 978-3-7315-1425-1

Die Bände sind unter www.ksp.kit.edu als PDF frei verfügbar oder als Druckausgabe bestellbar.

The investigation of multi-physics problems using continuum models is becoming increasingly important, e.g., the analysis of chemical and mechanical fields in the design of energy storage systems. To address the complexity of real processes, validated models and efficient implementation schemes in commercial Finite-Element solvers are essential.

In this work, we derive chemo-mechanically coupled continuum models in a thermodynamically consistent manner. We adress hydrogen embrittlement, phase-separation in thin-film metal-hydrogen systems and water diffusion in Polyamide 6.

In the context of hydrogen embrittlement we present a scheme to solve chemo-mechanically coupled models, using the chemical potential of hydrogen as degree of freedom and validate it.

In the context of phase-separation in thin-film metal-hydrogen systems, we present a model to describe phase-separation in Niobium and Palladium thin-films under hydrogen loading. The model is investigated both analytically and using Finite-Element simulations.

Finally, we present a chemo-mechanically coupled model for the diffusion of water in Polyamide 6. The model is capable of predicting the drying of Polyamide 6 in dependence on humidity levels and environmental temperature, while also capturing an increase in the relaxation modulus during prolongued tests at elevated temperatures due to drying.

ISSN 2192-693X
ISBN 978-3-7315-1425-1

Gedruckt auf FSC-zertifiziertem Papier

ISBN 978-3-7315-1425-1
9 783731 514251